Title	COMPOSITE MODELING OF CREEP VOIDS IN TEXTURED COPPER BASED ON ULTRASONIC VELOCITIES
Author(s)	森下, 智博
Citation	大阪大学, 1998, 博士論文
Version Type	VoR
URL	https://doi.org/10.11501/3144153
rights	
Note	

COMPOSITE MODELING OF CREEP VOIDS IN TEXTURED COPPER BASED ON ULTRASONIC VELOCITIES

Tomohiro MORISHITA
November 1997

ABSTRACT

This thesis presents a composite modeling of creep voids in textured pure copper. A simple procedure is used to separate the elastic anisotropy due to texture. The effective stiffness of the voids/copper composite is related to the ultrasonic velocities.

The creep experiment is made by the best possible procedures for being compatible with the theoretical treatment. No precipitation of the second phase particles and no texture modification occur during creep. The density and the ultrasonic velocities are measured for the composite. Ultrasonic velocities decrease and their anisotropy develops with decreasing density due to creep voids. The elastic anisotropy due to texture is canceled by using normalized velocities.

Five models for creep voids are considered based on the elasticity theory of particle dispersed composite. There are four void modeling factors; the volume fraction, the shape, the positional distribution, and the orientation distribution. The effective elastic stiffness is obtained as a function of the modeling parameters, and it is related to the velocities. The volume fraction is obtained by the measured density so that we characterize the remaining three factors for the modeling study. It is concluded that the double composite model is best for the explanation of experimental features including the evolution of velocity changes and their anisotropy. In this model, the shape of voids is assumed to be spherical. Their positions are restricted to within the oblate areas dispersed randomly in the copper matrix. The minor axes of oblate areas are statistically tilted in an orthorhombic way. The model represents well the creep damaging process. The ellipsoidal elements are sparsely scattered in the matrix, but they continue to grow in volume as the creep progresses, containing more and more voids in them. The elastic anisotropy develops by the preferential void formation within the grain boundaries perpendicular to the stress axis.

The double composite model provides a basis for understanding complicated and important phenomena of creep fracture. The concept of this work, the effective stiffness of the creep damaged material, is applicable to the heat resistant materials involving metallurgical complexity. Modeling for them remains for the further study.

CONTENTS

Chapter 1

INTRODUCTION

1.1 Effective moduli of particle dispersed composite

Micromechanics of composite materials and defects in solids has been developed in the field of the elastic theory [1] -[5]. This thesis applies the results on macroscopic elastic moduli of particle dispersed composites to the crept metal containing voids.

In a particle reinforced composite, a large number of particles are dispersed in the matrix. Each of them has a distinct boundary and is separated from the other particles. A typical example of them is short-fiber reinforced composites which are increasingly being used in a wide range of applications. Short fibers are regarded as slender prolate ellipsoidal inclusions. The macroscopic (overall) elastic properties of such materials can be derived by applying the micromechanics theories. The macroscopic elastic moduli of composites, called the effective elastic moduli, depend on the elastic constants of its constituents and the inclusion aspects; the inclusion volume fraction, the geometric parameters, and the positional and orientational distribution of the inclusions.

The composites have been designed using inefficient trial-and-error approaches. These costly approaches were mandated because there existed a fundamental gap in the understanding of the relations between microstructure and overall properties. The rule of mixtures, arithmetic average of elastic constants of its constituents weighting by the volume fraction, has been used to estimate the effective elastic moduli. However, it had no coincidence with experimental results. Up to now, the proper theories have been studied to estimate the effective elastic moduli.

The effective elastic constants for spherical inclusions with dilute suspension were first derived by Dewey [6]. In this derivation, no interaction or long distance among inclusions was supposed, so that the result was limited to very small inclusion volume fraction. The theoretical studies have been developed to generalize the inclusion aspects.

For ellipsoidal inclusions, Eshelby's work [7] has played an important role. He considered the case of one ellipsoidal inclusion in the matrix and proved that the state of stress and

1

strain remains uniform inside the inclusion when the external uniform stress is applied at a far distance from it. The effective elastic moduli for prolate ellipsoidal inclusions of dilute suspension with restriction of all aligned orientation was derived by Russel and Acrivos [8] based on the result obtained by Eshelby.

The problem for non-dilute suspension becomes complicated because it involves the interaction among the inclusions. A three-phase model for spherical inclusions with non-dilute suspension was introduced by Kerner [9] and van der Pol [10] and was modified later by Christensen and Lo [11]. In their model, a spherical inclusion surrounded by spherical matrix phase is embedded in infinite equivalent homogeneous media with unknown properties. An approximate method of the self-consistent scheme was first devised by Hershey [12] and Kröner [13] as means to model the behavior of single phase polycrystalline materials. The extension of the scheme to composite materials with non-dilute suspension was given by Hill [14] and Budiansky [15]. The method has a very simple geometric interpretation. It assumes a single inclusion in an infinite matrix of the unknown effective properties of the problem. Mori-Tanaka theory [16] was then applied to obtain the effective elastic moduli. For a full range of volume fraction, the theory gives average stress in matrix. By Weng and his colleagues, the effective moduli for several cases were derived based on the Mori-Tanaka theory: multiphase composite containing spherical inclusions [17], unidirectionally aligned spheroidal inclusions [18], ellipsoidal inclusions with random orientation [19], spheroidal voids with some orientation distributions [20], and dual-phase metals with randomly oriented spheroidal inclusions [21].

The effective moduli have been studied for the particle reinforced composite. However, they are applicable to the porous materials, by assuming zero elastic constants of the inclusion.

1.2 Purpose of this work and theoretical assumptions

This thesis presents an application of the theory for effective moduli to the creep damaged material. The damaged material in the intergranular creep process is regarded as a porous material. Voids (or cavities) nucleate on grain boundaries at the initial stage of creep. The nucleation occurs even within 10 percent time to rupture [22]. Voids grow in volume and/or number especially on the grain boundaries perpendicular to the stress direction. The nucleation and growth of voids continue over the entire range of creep curve [23, 24]. Subsequent coalescence leads to microcracking and eventually macroscopic cracks occur.

To make the theoretical treatment simple, we use the following assumptions:

(1) No precipitation of the second phase particles,

(2) No texture modification,

(3) No dislocation restructuring,

(4) No interaction between the effects of voids and texture.

In the general creep process for the heat resistant materials, the macroscopic stiffness is altered from the uncrept state by not only the nucleation and the growth of voids but also the metallurgical attributes. The first three assumptions are introduced to ignore these attributes. The first two assumptions are realized by the intergranular creep experiments on a pure metal. The third is easily acceptable, because the effect would be sufficiently smaller than the void effect. Also, this effect is minimized by annealing the samples prior to the experiments.

The problem is still complicated even with the first three assumptions. The macroscopic stiffness of polycrystallite metals has an anisotropy in an uncrept state. It is caused by the texture developed during the manufacturing process. The rigorous expression of the effective stiffness in creep damaged material should then be obtained for the composite comprising the anisotropic matrix and voids. The last assumption is introduced to give a further simple procedure in calculating the approximated effective stiffness supposing the isotropic matrix composite. For this simple procedure, we use the theory of polycrystalline aggregate [25, 26]. According to the theory, the anisotropic deviation stiffness due to texture ΔC_{ijkl}^T is separated from the macroscopic stiffness as

$$C_{ijkl}^R = C_{ijkl}^M + \Delta C_{ijkl}^T, \tag{1.1}$$

where C_{ijkl}^R is the macroscopic stiffness in uncrept sample (we refer to it as a reference sample) and C_{ijkl}^M is the isotropic stiffness. Using above four assumptions, the effective stiffness in damaged sample C_{ijkl}^* is simply written as

$$\begin{aligned} C_{ijkl}^* &= C_{ijkl}^M + \Delta C_{ijkl}^T + \Delta C_{ijkl}^V, \\ &= C_{ijkl}^R + \Delta C_{ijkl}^V, \\ &= C_{ijkl}^C + \Delta C_{ijkl}^T, \end{aligned} \tag{1.2}$$

where ΔC_{ijkl}^V is the deviation stiffness due to void formation and growth. Because ΔC_{ijkl}^T is also separated in the damaged sample by using the assumption (4), the effective stiffness $C_{ijkl}^C = C_{jkl}^M + \Delta C_{ijkl}^V$ can be calculated for a composite comprising of the isotropic matrix and the voids.

The velocities of ultrasonic bulk waves in this porous material reflect the voids state because they are simply given by the square root of the effective stiffness divided by the overall density. We will present an interpretation of the velocity change due to voids through the creep void

3

modeling and the calculation of the effective stiffness. The ultrasonic velocities in the reference sample have the anisotropy due to texture. Those in the damaged samples includes further the void effect.

1.3 Outline of the thesis

Figure 1.1 shows the outline of the thesis. Experimental procedure is described in the beginning. The results are studied in two subjects, texture effect and void effect, respectively. The study on void effect is organized by the theoretical case studies and the numerical calculations in the modeling.

In chapter 2, the experiment will be described. We will make the best possible procedures to carry out a simple experiment for being compatible with the first two assumptions. Polycrystalline pure copper samples machined from a rolled plate are used. The specimens are subjected to the stabilization annealing, and creep condition is chosen for the brittle failure. Ultrasonic velocities in reference (uncrept) samples show an intrinsic orthorhombic anisotropy due to the rolling texture. The density and the ultrasonic velocities in creep damaged samples

Chapter 2 (Experiment)
- Velocities in reference sample
- Relation between normalized velocities and density

Chapter 3 (Texture effect)
- Theory
  - Orientation distribution function
  - $C_{ijkl}^{R} = C_{ijkl}^{M} + \Delta C_{ijkl}^{T}$
- $|\Delta C_{ijkl}^{T}/C_{ijkl}^{M}| \ll 1$
- Texture effect

Void effect
- Chapter 4 (Theoretical case studies)
  - $C_{ijkl}^{C} = C_{ijkl}^{M} + \Delta C_{ijkl}^{V}$
  - (A) Spherical inclusions
  - (B) Unidirectionally aligned spheroidal inclusions
  - (C) Partially oriented spheroidal inclusions
- Chapter 5 (Modeling studies)
  - (1) Spherical voids model (A)
  - (2) Unidirectionally aligned oblate voids model (B)
  - (3) Randomly oriented oblate voids model (C')
  - (4) Partially oriented oblate voids model (C)
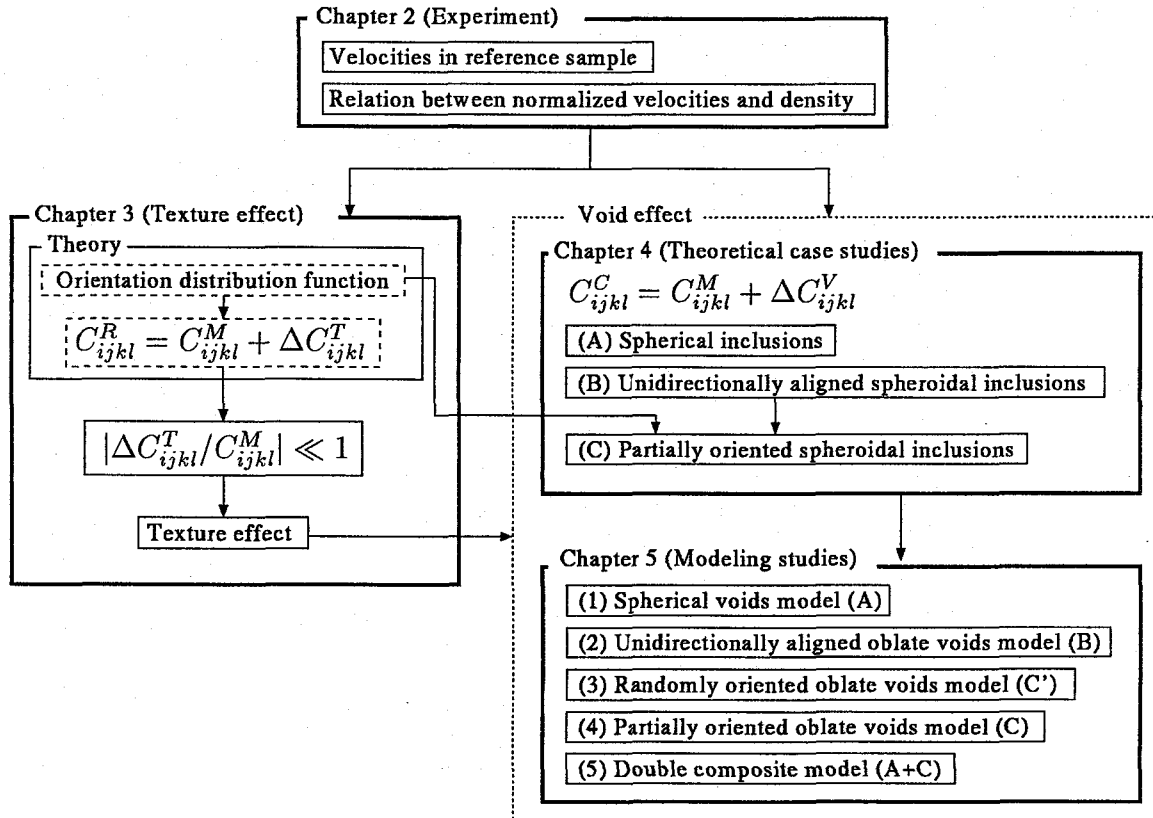 - (5) Double composite model (A+C)

Fig. 1.1. Outline of the thesis.

are measured. The density decreases due to the generation of voids. The relation between the velocities normalized by those in the reference samples and the density change are presented. The normalized velocities decrease with the decreasing density. Their anisotropy is observed and develops with the decreasing density. Discussion in the following chapters are based on these measurement results.

The study on texture effect will be described in chapter 3. We will separate the anisotropic deviation stiffness from the macroscopic stiffness using the theory for polycrystallite metals. In the beginning of the chapter, the theory will be described with the attention to the single-phase polycrystallite cubic metal having statistically the orthorhombic symmetry (rolling texture). This is pertinent for the material used in the experiment, that is, pure copper samples machined from a rolled plate. The crystallite orientation distribution function (crystallite-ODF), a probability density function to represent the orientation of single crystallite, is introduced. The explicit form of $C_{ijkl}^{R} = C_{ijkl}^{M} + \Delta C_{ijkl}^{T}$ is obtained through the ODF. The values for C_{ijkl}^{M} and ΔC_{ijkl}^{T} are calculated from the measured velocities. These values will be used as the material properties in the following modeling studies for the void effect. The inequality $|\Delta C_{ijkl}^{T}/C_{ijkl}^{M}| \ll 1$ (without the summation convention) holds. It supports the assumption (4). If the assumption is not possible, the calculation of the effective stiffness for the composite comprising of the anisotropic matrix and voids is required. However, the inequality permits a simple procedure, the isotropic matrix is used in the calculation of C_{ijkl}^{C} and the texture effect ΔC_{ijkl}^{T} is added later to C_{ijkl}^{C}. Therefore, the effective stiffness in damaged samples is expressed as $C_{ijkl}^{*} = C_{ijkl}^{M} + \Delta C_{ijkl}^{T} + \Delta C_{ijkl}^{V}$. The texture effect on the normalized velocities is then discussed, leading to a conclusion that they exclude the texture effect ΔC_{ijkl}^{T} within the first order approximation. The study on the void effect will be carried out based on the conclusion.

Theoretical case studies on void effect are described in chapter 4. The isotropic matrix is supposed, and the effective stiffness of the composite $C_{ijkl}^{C} = C_{ijkl}^{M} + \Delta C_{ijkl}^{V}$ will be obtained by the theory for particle dispersed composites. The inclusions, or voids in our interest, are also assumed to be isotropic and their shape is spheroidal. The void effect ΔC_{ijkl}^{V} depends on the void factors; the volume fraction, the shape (the aspect ratio), the positional distribution, and the orientation distribution of non-spherical voids. In this chapter, the positional distribution of voids is assumed to be random. (Non-random distribution will be discussed in the later chapter.) The effective stiffness C_{ijkl}^{C} is given for three cases. In the case A, the inclusions are assumed to be spherical. The composite is then macroscopically isotropic. The void effect ΔC_{ijkl}^{V} is given only by the volume fraction. In the case B, the spheroidal inclusions are

5

Table 1.1. Void factors and use for the expression in chapter 4.

	shape of voids	positional distribution	orientational distribution	case
model 1	sphere	random	–	A
model 2	oblate ellipsoid	random	unidirectional	B
model 3	oblate ellipsoid	random	random	modified C
model 4	oblate ellipsoid	random	partially oriented	C
model 5	sphere	restricted to oblate areas	areas partially oriented	A within C

assumed to be all aligned. The composite is transversely isotropic, and has five independent elastic constants. ΔC^V_{ijkl} is given by the volume fraction and the aspect ratio. The case C is a modified version of the case B by including the orientation distribution. The inclusion-ODF is introduced with an analogy of the crystallite-ODF in chapter 3. The distribution is assumed to be statistically orthorhombic. ΔC^V_{ijkl} depends on the volume fraction, the aspect ratio, and the orientation distribution.

In chapter 5, the void effect will be discussed by the modeling studies. The effective elastic stiffness C^C_{ijkl} is obtained as a function of the modeling parameters, and it is related to the normalized velocities. Since the volume fraction is obtained from the measured density, we characterize the remaining three factors for the modeling study. Five models are considered. The void factors are summarized in Table 1.1. The expressions of C^C_{ijkl} in them are obtained using the theoretical case studies in chapter 4. It will be concluded that the model 5 is best for the creep damage. The model 5 explains the quantitative relation between the normalized velocities and the change in density, perfectly. Moreover, it represents well the damaging process. The oblate areas are sparsely scattered in the matrix, but they continue to grow in volume as the creep progresses, containing more and more voids in them. The elastic anisotropy develops by the preferential void formation within the grain boundaries (oblate areas) perpendicular to the stress axis.

Chapter 2

# ULTRASONIC VELOCITY CHANGE WITH CREEP VOIDS IN COPPER

2.1 Introduction

In this chapter, the experimental results are described. We make the best possible procedures to carry out a simple experiment for being compatible with the theoretical treatments. To avoid the precipitation, pure copper is used. To suppress the texture modification by the recrystallization, a stabilization annealing is provided prior to the creep tests. The test conditions are chosen for intergranular creep fracture to take place. There should be no plastic deformation, because the rupture occurred in a brittle manner, leaving little elongation of specimens. The ultrasonic velocities shows an anisotropy due to texture even in the initial state. We measure the change of ultrasonic velocities and density in creep damaged samples. The features in velocities and photomicrographic observations of voids will give suggestions for the modeling study.

2.2 Creep test

Test material is a commercial tough pitch copper of 99.95 mass pct purity. Copper has been used for the fundamental study of creep fracture because of its relatively short time to rupture and large density [23, 24, 27, 28]. The creep specimens were machined from a rolled plate of 20 mm thick. To suppress the texture modification by the recrystallization, the plate was annealed at 800 °C, which was higher than the creep temperature, for 3 hours before machining. They were further annealed at 550 °C for 20 hours before the creep tests. Specimen geometry and the sample coordinate system $O - x_1 x_2 x_3$ are shown in Fig. 2.1. The x_1 direction lies along the thickness direction of the original plate and the x_2 axis along the rolling direction. Tensile load is applied in the x_3 direction.

Creep tests were done under the constant load in air. Eight specimens were crept to failure, four at 500°C and the other four at 550°C to know the time to rupture. The nominal stress was 6.0 MPa at the minimum cross section. The creep conditions were chosen for intergranular

Fig. 2.1. Specimen geometry and sample coordinate system.

Table 2.1. Creep test conditions and rupture times.
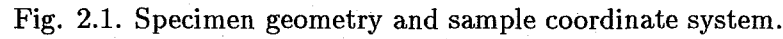
Stress (MPa)		6.0	
Temperature (°C)		500	550
Rupture time (hr)		618.9	279.2
		573.1	264.2
		580.5	267.3
		618.6	272.6
	t_r	597.8	270.8
Time of interrupt test t/t_r		0.1 0.2 0.3 0.4 0.5 0.6 0.7 0.75 0.8 0.85 0.9	

fracture, referring to a fracture-mechanism map for copper [29]. The temperature was held within the fluctuation of 2°C; its spatial variation along the specimen gauge length was less than 2°C. The test conditions and the rupture times are listed in Table 2.1. The scatter of rupture time is relatively small because all specimens were machined from a plate. The average rupture time, t_r, was 597.8 hours at 500°C and 270.8 hours at 550°C. The elongation of the ruptured specimens was negligible despite the fairly high ductility at the room temperature as shown in Fig. 2.2. Brittle fracture occurred without any visible precursors. The location was within 10 mm from the minimum cross section. We can suppose that the effect of texture modification by plastic deformation is sufficiently smaller than the void effect.

We made interrupt tests in the same creep conditions as the rupture tests to obtain coupons for the density and ultrasonic measurements. Eleven interrupting times were chosen relative to t_r as shown in the bottom row of Table 2.1. Shallow notches were introduced to obtain two cube
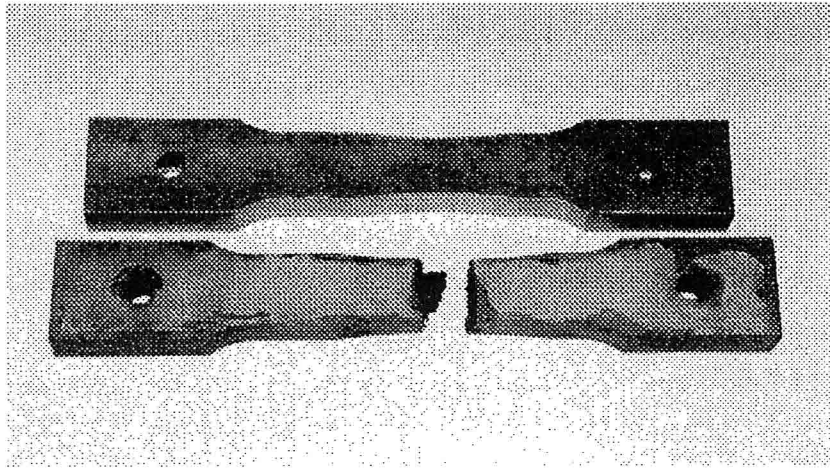
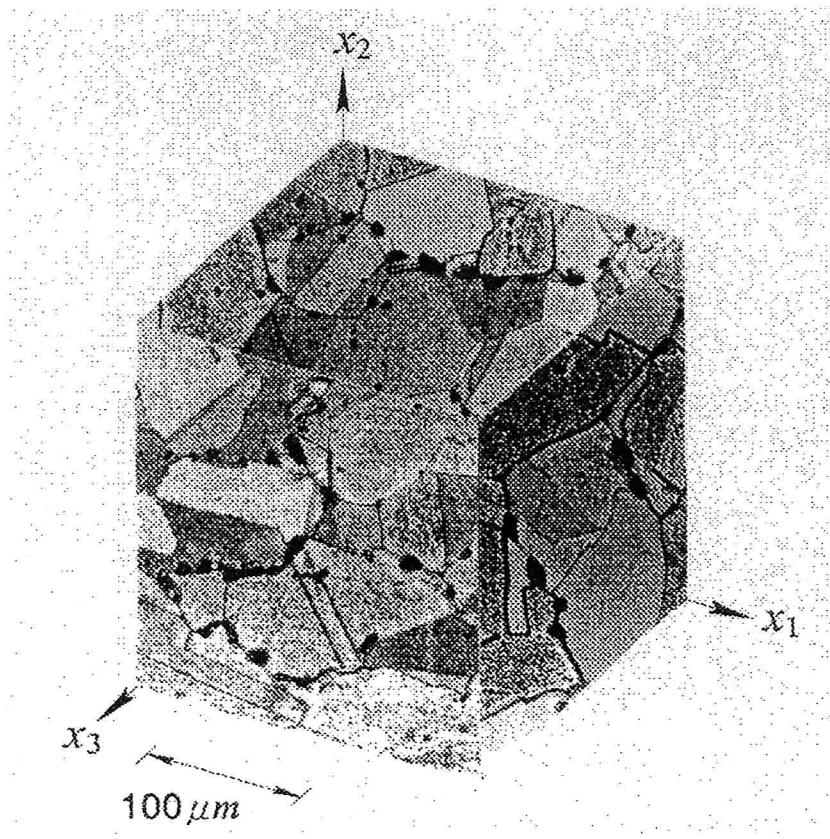Fig. 2.2. Comparison of uncrept and ruptured specimens.

Fig. 2.3. Photomicrograph of creep damaged copper; notched position, $t/t_r = 0.7$, 550°C, 6.0 MPa.

samples, 20 mm on each side, of different damage states (Fig. 2.1). They underwent slightly different stresses with the equal thermal history. Because the stress concentration factor at the notch bottom was estimated as 1.04 from a finite element computation, we ignored the damage inhomogeneity around the notches. Here we refer to them as the damaged samples. For a comparison purpose, we prepared six reference samples of the same dimensions from a specimen after the heat treatment.

Figure 2.3 is a typical photomicrograph of the damaged samples. The grain shape is nearly equiaxial and the grain size is approximately 0.1 mm. Voids are not randomly positioned. They tend to gather preferentially on the grain boundaries perpendicular to the x_3 (stress) direction. The void diameter is approximately 10 μm at this stage of creep.

2.3 Porosity

Because no precipitation of the second phase particles occurs during creep, the porosity c, that is the void volume fraction, is equivalent to the decreasing rate of density:

$$c = 1 - \frac{\rho_*}{\rho_R}, \tag{2.1}$$

where ρ_R and ρ_* are the densities of the reference (uncrept) and damaged samples, respectively. We determined c from the weight measurements as Ratcliffe [30] did:

$$c = 1 - \frac{W_*^a \left(W_R^a - W_R^w\right)}{W_R^a \left(W_*^a - W_*^w\right)}, \tag{2.2}$$

where "a" and "w" indicate the weights in air and in water. The method doesn't give the densities, but it gives directly the density ratio, or the porosity. This measurement of c is independent of the sample volume and the fluid density. The weight measurements were done using a digital electric balance with 0.1 mg accuracy. The experimental equipment for measuring weight in water is illustrated in Fig. 2.4. A beaker is held on a support straddling the balance table. The weight of cubic sample is applied to the balance table through the swing hanging from the top. The top plate has a circle hole to insert a sample. The weight of equipment was canceled before the measurement. To suppress the error caused by the rise of the water level, a fishing line with 0.090 mm diameter was used to hang the swing. The measuring error of the porosity was estimated to be less than $\pm 10^{-4}$. The tolerance is tested through many trial measurements by choosing two out of reference samples.

Figure 2.5 shows the change of porosity c with creep time. The solid lines are the least-square fitting curves of $c = 1 - (1 - t/a)^b$. The constants a and b are listed in the figure. For the samples from the notches, c increased at the accelerating rates. The samples from the
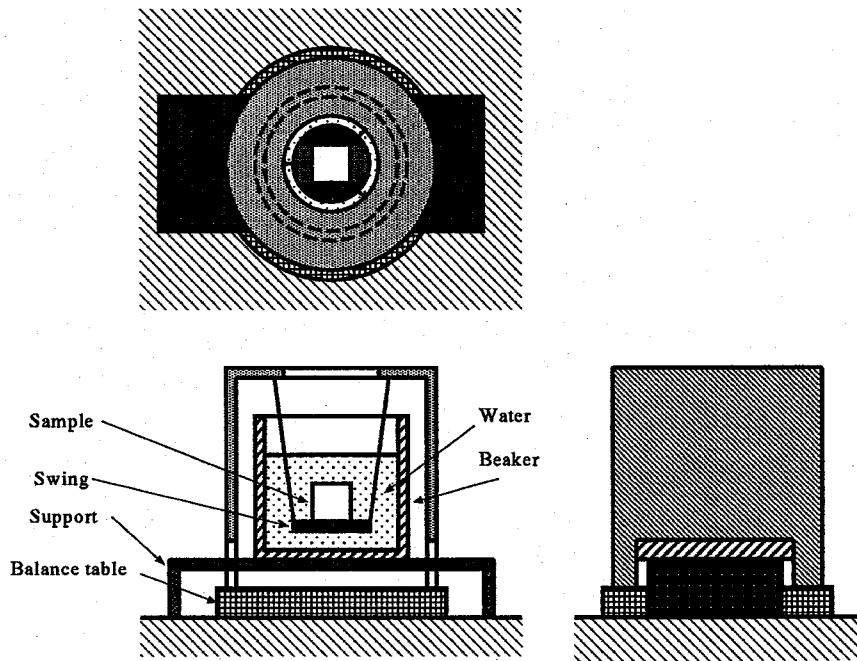
Fig. 2.4. Experimental equipment for weight measurements in water.

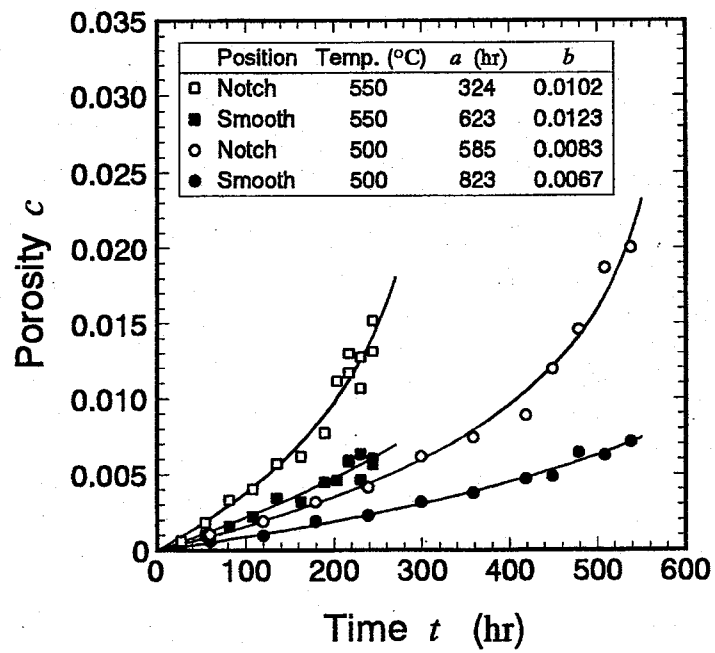| Position	Temp. (°C)	a (hr)	b
□ Notch	550	324	0.0102
■ Smooth	550	623	0.0123
○ Notch	500	585	0.0083
● Smooth	500	823	0.0067

Fig. 2.5. Evolution of porosity c with creep time. Least-square fitting curves are $c = 1 - (1 - t/a)^b$.

smooth positions displayed a slower increase because of the slightly lower stress. The creep tests were duplicated at 550 °C for $t/t_r = 0.8$, 0.85, and 0.9. The difference for nominally the same creep condition arises probably from the metallurgical inhomogeneity, which causes a variation in the rupture time or the damage accumulation rate in the individual specimens. The slopes of porosity increase at $t = 0$ are not equal to zero. This indicates that the voids nucleate from the beginning of the creep test. Similar results have been obtained for Cr-Mo-V steel [22], OFHC copper [23], SUS347 [31], and SUS304 [32].

Boettner and Robertson [23] measured the density change and the creep strain during creep at 500 °C for OFHC copper. They showed that the increasing rate of porosity was not coincident with that of the creep strain. According to their results, the creep curve, that was the creep strain versus time, was divided into primary, secondary, and tertiary creep periods. On the other hand, the increase of porosity c was a continuous process.

2.4   Ultrasonic velocities

Ultrasonic velocities are measured by the pulse reflection method. An ultrasonic pulse, introduced by a transducer from a surface, is reflected at the opposite side and returns to the transducer. Ultrasonic velocities are calculated by dividing a traveling distance, which is two times distance between the parallel surfaces, with the measured transit time.

We used the sing-around technique to measure the transit time. Experimental setup is shown in Fig. 2.6. It contains a sing-around unit, an oscilloscope to observe the waveform, a transducer to excite and receive the ultrasonic pulse, and a personal computer. The personal computer is connected by RS232C to the sing-around unit, and controls it and processes the measured data. The transducer is attached on the specimen with the couplant. We measured the velocities of nine plane waves propagating and polarized in the principal directions using 7.5 mm square piezoelectric transducers. The center frequency was 10 MHz for longitudinal waves and 5 MHz for shear waves. The accuracy was $\pm 1.3 \times 10^{-3}$ in terms of V^*/V^R, where V^R denotes the average velocity over six reference samples and V^* denotes the velocity in creep damaged sample.

It is often the case that the texture varies in the thickness direction of the rolled plate. However, the reference samples showed an ideal orthorhombic anisotropy due to the rolling texture. In Table 2.2, exchanging the propagation and polarization directions leaves the shear wave velocity virtually unchanged. Maximum velocity difference is $V_{31}^R/V_{13}^R = 0.9976$, where V_{ij} refers to the velocity of elastic wave propagating in the x_i direction and polarized in the x_j direction. The creep loading creates a damage-induced anisotropy, which has the axes coincident with the original principal axes and is regarded to be superimposed upon the
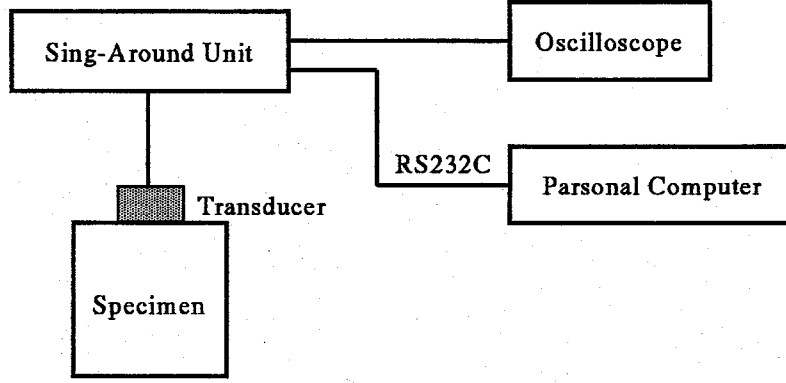
Fig. 2.6. Experimental setup for ultrasonic velocities.

Table 2.2. Ultrasonic velocities in the reference sample. (unit: m/s)

		Polarization direction		
		x_1	x_2	x_3
Propagation	x_1	4726	2303	2287
direction	x_2	2308	4723	2284
	x_3	2281	2285	4734

texture-induced anisotropy as Eq.(1.2). Specimens had shallow notches (Fig.2.1) causing a degree of inhomogeneity. However, the velocities in creep damaged samples demonstrated a macroscopic elastic homogeneity with the equivalent shear wave velocities in exchanging the propagation and polarization directions. This is beneficial for the modeling study.

The relations between the porosity c and the normalized velocities are plotted in Fig. 2.7. The solid lines represent the least-square fitting with polynomials. Polynomial fitting curves are $V^*/V^R = 1 - ac - bc^2$; the constants are shown in the figure. The longitudinal wave suffered from a severe damping in the final stage of creeping. The velocity V_{33}^* was not obtainable for $c > 0.018$. All normalized velocities decrease acceleratingly and their anisotropy develops with increasing c. The velocity of longitudinal wave propagating in the stress direction V_{33}^* is most sensitive to the creep damage, and V_{12}^* is most insensitive. V_{11}^*/V_{11}^R and V_{23}^*/V_{23}^R are approximately equal to V_{22}^*/V_{22}^R and V_{31}^*/V_{31}^R, respectively.

Ledbetter et al. [33] measured the ultrasonic velocities for longitudinal wave in creep damaged copper. Their results also show $V_{33}^*/V_{33}^R < V_{11}^*/V_{11}^R$. Although they gave the linear relation between the porosity and the ultrasonic velocities, their discussion was restricted to within $c < 0.006$.
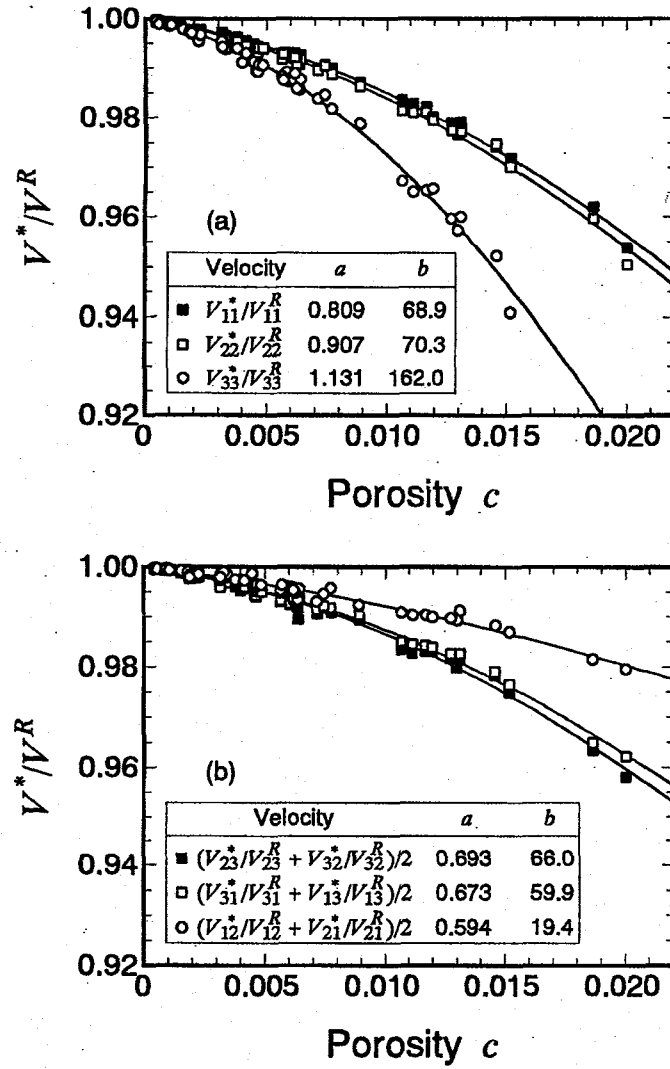
13

(a)

Velocity	a	b
■ V_{11}^*/V_{11}^R	0.809	68.9
□ V_{22}^*/V_{22}^R	0.907	70.3
○ V_{33}^*/V_{33}^R	1.131	162.0

(b)

Velocity	a	b
■ $(V_{23}^*/V_{23}^R + V_{32}^*/V_{32}^R)/2$	0.693	66.0
□ $(V_{31}^*/V_{31}^R + V_{13}^*/V_{13}^R)/2$	0.673	59.9
○ $(V_{12}^*/V_{12}^R + V_{21}^*/V_{21}^R)/2$	0.594	19.4

Fig. 2.7. Relation between porosity c and normalized ultrasonic velocities for longitudinal waves (a) and shear waves (b). Polynomial fitting curves are $V^*/V^R = 1 - ac - bc^2$.

2.5 Summary

Annealed copper specimens were used in the creep test. The elongation of the ruptured specimens was negligible, and a brittle fracture occurred without any visible precursors. The theoretical assumptions (1) and (2) described in chapter 1 were satisfied. The porosity and the ultrasonic velocities were measured. Porosity c increased at the accelerating rates with creep time. It was represented by a function of $c = 1 - (1 - t/a)^b$. The relations between porosity c and normalized velocities were given by polynomials $V^*/V^R = 1 - ac - bc^2$. Equivalent shear wave velocities in exchanging the propagation and polarization directions indicated the

homogeneity of the texture and the damage.

The experimental results give the following suggestions for the creep void modeling. They will be further discussed in the following chapters.

(1) The reference (uncrept) samples show an intrinsic orthorhombic anisotropy due to the rolling texture.

(2) All normalized velocities decrease acceleratingly with increasing c.

(3) The anisotropy of them develops with increasing c.

(4) The equalities $V_{11}^*/V_{11}^R = V_{22}^*/V_{22}^R$ and $V_{23}^*/V_{23}^R = V_{31}^*/V_{31}^R$ approximately hold.

(5) The inequalities $V_{33}^*/V_{33}^R < V_{11}^*/V_{11}^R < V_{23}^*/V_{23}^R < V_{12}^*/V_{12}^R$ hold.

(6) Voids are not randomly positioned, but they tend to gather preferentially on the grain boundaries perpendicular to the stress direction.

Chapter 3

TEXTURE EFFECT

3.1 Introduction

If the orientation distribution of polycrystalline aggregate is perfectly random, the material is macroscopically isotropic because the intrinsic strong anisotropy of single crystals is neutralized. However, the orientation distribution is not random in many cases because of solidification, heat treatment, or plastic deformation in the manufacturing process. The preferred orientation is called texture. Because of texture, polycrystalline metals have elastic, plastic and magnetic anisotropy.

The explicit form of macroscopic elastic stiffness in reference sample $C_{ijkl}^{R} = C_{ijkl}^{M} + \Delta C_{ijkl}^{T}$ is presented by the theory on polycrystalline aggregate. The values for C_{ijkl}^{M} and ΔC_{ijkl}^{T} are calculated from the measured velocities. The inequality $|\Delta C_{ijkl}^{T}/C_{ijkl}^{M}| \ll 1$ is obtained. It supports the theoretical assumption (4) in this thesis, and allows us to express the effective stiffness in damaged sample as $C_{ijkl}^{*} = C_{ijkl}^{M} + \Delta C_{ijkl}^{T} + \Delta C_{ijkl}^{V}$. The effect of texture on normalized velocities is discussed. We will reach a conclusion that the normalized velocities exclude the effect within the first order approximation.

3.2 Macroscopic elastic moduli of polycrystallite metal

The texture has been represented by pole figure diagrams obtained by x-ray diffraction method [34]. The pole figure diagrams are two dimensional or stereographic expression for the distribution of selected crystallographic plane normals. They don't have the information about the rotation around the normals. A harmonic method for quantitative texture analysis was developed by Bunge [35] and Roe [25, 26] in the 1960s. Their mathematical formulations are equivalent, but we will adopt Roe's notation throughout this work. The method requires the intensity of diffracted x-ray measured as a function of the orientation of the sample to decide the coefficients of the orientation distribution function (ODF). In the last fifteen years, intensive studies have been directed toward obtaining the coefficients of the ODF by measuring

ultrasonic velocities and relating them to the texture [36] -[40]. The ultrasonic method gives the texture using only lower order coefficients of the ODF.

A harmonic method for quantitative texture analysis is described in this section. The ODF is related to the macroscopic elastic moduli of textured polycrystalline metal. We will here describe it with the attention on a single-phase polycrystalline cubic metal having statistically the orthorhombic symmetry (rolling texture).

3.2.1 Crystallite orientation distribution function

We begin by taking up a crystallite (grain) in a polycrystalline sample. The crystallographic axes [100], [010], and [001] are chosen for the crystallite-fixed axes, X_i. We simply take the sample-fixed axes, x_1, x_2, and x_3 aligned in the normal, rolling, and transverse directions of the plate sample, respectively. The relation between the crystallite axes $O - X_1X_2X_3$ and the sample axes $O - x_1x_2x_3$ can be specified using three Euler angles, ψ, θ, and ϕ. That is, these Cartesian coordinate systems come to coincide with each other through the rotations of $-\phi$ around the X_3 axis, $-\theta$ around the X_2 axis, and $-\psi$ around the X_3 axis in this order as shown in Fig. 3.1. The coordinate transformation from X_j to x_i can be written with the
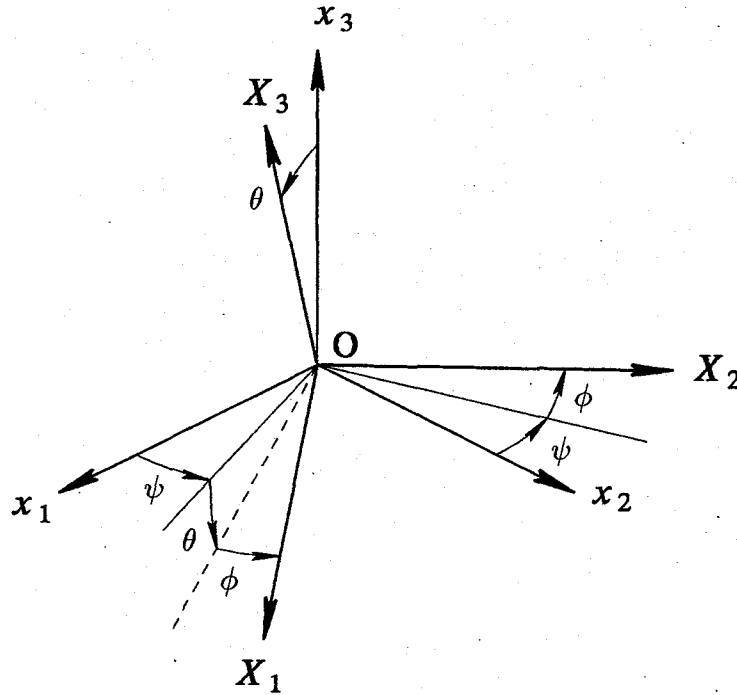

Fig. 3.1. Sample-fixed coordinate $O - x_1x_2x_3$ and crystallite-fixed coordinate $O - X_1X_2X_3$.

summation convention as

$$x_i = \beta_{ji} X_j, \qquad i,j = 1,2,3 \qquad (3.1)$$

where the transformation tensor β_{ji} is written as

$$\beta_{ji} = \begin{pmatrix} \cos\psi\cos\theta\cos\phi - \sin\psi\sin\phi & \sin\psi\cos\theta\cos\phi + \cos\psi\sin\phi & -\sin\theta\cos\phi \\ -\cos\psi\cos\theta\sin\phi - \sin\psi\cos\phi & -\sin\psi\cos\theta\sin\phi + \cos\psi\cos\phi & \sin\theta\sin\phi \\ \cos\psi\sin\theta & \sin\psi\sin\theta & \cos\theta \end{pmatrix}. \qquad (3.2)$$

The crystallites making up the polycrystalline sample have a wide range of the crystallographic orientation relative to the sample coordinate. An orientation distribution function (ODF) w, that is, a probability density function, is introduced for the purpose of uniquely representing the crystallite orientation distribution. The integration of this probability density over all possible orientations is naturally unity:

$$\int_0^{2\pi} \int_0^{2\pi} \int_{-1}^1 w(\xi, \psi, \phi) d\xi d\psi d\phi = 1, \qquad (3.3)$$

where $\xi = \cos\theta$.

In the harmonic method, the ODF w is expanded in a series of generalized spherical harmonics as

$$w(\xi, \psi, \phi) = \sum_{l=0}^{\infty} \sum_{m=-l}^{l} \sum_{n=-l}^{l} W_{lmn}^T Z_{lmn}(\xi) \exp(-im\psi) \exp(-in\phi), \qquad (3.4)$$

where the $Z_{lmn}(\xi)$ is the generalization of associated Legendre function defined by Roe [25]. The expansion coefficients W_{lmn}^T are called crystallite orientation distribution coefficients (crystallite-ODCs) and are determined by

$$W_{lmn}^T = \frac{1}{4\pi^2} \int_0^{2\pi} \int_0^{2\pi} \int_{-1}^1 w(\xi, \psi, \phi) Z_{lmn}(\xi) \exp(im\psi) \exp(in\phi) d\xi d\psi d\phi. \qquad (3.5)$$

From the discussion of pole figure diagrams related to the ODF w, it is concluded that W_{lmn}^T is identically equal to zero when l is odd. The function $Z_{lmn}(\xi)$ in Eq.(3.4) is a solution of

$$\left(1 - \xi^2\right) \frac{d^2 Z}{d\xi^2} - 2\xi \frac{dZ}{d\xi} + \left\{ l(l+1) - \frac{m^2 - 2mn\xi + n^2}{1 - \xi^2} \right\} Z = 0, \qquad (3.6)$$

and have the following properties:

$$\int_{-1}^1 Z_{lmn}(\xi) Z_{l'mn}(\xi) d\xi = \delta_{ll'},$$

19

$$Z_{lmn}(\xi) = Z_{l\bar{n}\bar{m}}(\xi),$$

$$Z_{lmn}(\xi) = (-1)^{m+n} Z_{lnm}(\xi),$$

$$Z_{lm\bar{n}}(\xi) = Z_{lmn}(-\xi) = Z_{l\bar{m}n}(\xi),$$

where $\bar{m}$ stands for $-m$. The explicit forms of $Z_{lmn}(\xi)$ of lower orders are given as:

$$Z_{000}(\xi) = \frac{1}{\sqrt{2}},$$

$$Z_{200}(\xi) = \frac{\sqrt{5}}{2\sqrt{2}}\left(3\xi^2 - 1\right),$$

$$Z_{220}(\xi) = \frac{\sqrt{15}}{4}\left(-\xi^2 + 1\right),$$

$$Z_{400}(\xi) = \frac{3}{8\sqrt{2}}\left(35\xi^4 - 30\xi^2 + 3\right),$$

$$Z_{420}(\xi) = \frac{15}{8\sqrt{5}}\left(-7\xi^4 + 8\xi^2 - 1\right),$$

$$Z_{440}(\xi) = \frac{3\sqrt{35}}{16}\left(\xi^4 - 2\xi^2 + 1\right), \tag{3.7}$$

$$Z_{442}(\xi) = \frac{3\sqrt{14}}{16}\left(-\xi^4 - 2\xi^3 + 2\xi + 1\right),$$

$$Z_{44\bar{2}}(\xi) = \frac{3\sqrt{14}}{16}\left(-\xi^4 + 2\xi^3 - 2\xi + 1\right),$$

$$Z_{444}(\xi) = \frac{3}{16\sqrt{2}}\left(\xi^4 + 4\xi^3 + 6\xi^2 + 4\xi + 1\right),$$

$$Z_{44\bar{4}}(\xi) = \frac{3}{16\sqrt{2}}\left(\xi^4 - 4\xi^3 + 6\xi^2 - 4\xi + 1\right),$$

etc.

The value of $W_{000}^T = 1/(4\sqrt{2}\pi^2)$ is given by Eq.(3.7)$_1$ and the normalization condition Eq.(3.3).

Considering the symmetry properties of the cubic crystallites and that of the sample with the orthorhombic symmetry, many of the ODCs are found to be zero, and furthermore, the remaining coefficients are linearly dependent on each other. Because of this, the above procedure is highly simplified. Being restricted to the rolling texture of cubic metals, they have the following characteristics:

(a) W_{lmn}^T are real values,

(b) W_{lmn}^T are zero unless l and m are even and $n(\le l)$ is a multiple of 4,

(c) $W_{lmn}^T = W_{l\bar{m}n}^T = W_{lm\bar{n}}^T = W_{l\bar{m}\bar{n}}^T$,

20

(d) $W_{2m0}^T = 0$, $W_{4m4}^T = (5/\sqrt{70})W_{4m0}^T$, etc.

The characteristics (a)-(c) apply to orthorhombic, tetragonal, and cubic classes of crystal symmetry, but (d) applies to only cubic classes. It is then concluded that the independent texture parameters are only W_{400}^T, W_{420}^T, and W_{440}^T up to $l = 4$.

With the full benefit of symmetry consequences from (a) to (d), when the summation is truncated at $l = 4$, Eq.(3.4) reduces to

$$w(\xi, \psi, \phi) = \frac{1}{8\pi^2}$$
$$+ \frac{3}{8\sqrt{2}}W_{400}^T \left\{ \left(35\xi^4 - 30\xi^2 + 3\right) + 5\left(\xi^4 - 2\xi^2 + 1\right)\cos 4\phi \right\}$$
$$+ \frac{15}{4\sqrt{5}}W_{420}^T \left\{ \left(-7\xi^4 + 8\xi^2 - 1\right)\cos 2\psi \right. \tag{3.8}$$
$$\left. + \left(-\xi^4 + 1\right)\cos 2\psi \cos 4\phi + 2\left(\xi^3 - \xi\right)\sin 2\psi \sin 4\phi \right\}$$
$$+ \frac{3\sqrt{35}}{56}W_{440}^T \left\{ 7\left(\xi^4 - 2\xi^2 + 1\right)\cos 4\psi \right.$$
$$\left. + \left(\xi^4 + 6\xi^2 + 1\right)\cos 4\psi \cos 4\phi - 4\left(\xi^3 + \xi\right)\sin 4\psi \sin 4\phi \right\}.$$

3.2.2 Average weighted by ODF

We will now calculate the macroscopic elastic moduli incorporating the ODF $w(\xi, \psi, \phi)$. Sayers [36] has derived the elastic moduli as functions of the single-crystal elastic moduli and W_{4m0}^T ($m = 0, 2, 4$). He employed the Voigt type averaging procedure and averaged the single-crystal elastic moduli with w as a weighting function. As shown by Hill [41], the Voigt and Reuss averages provide the upper and lower bounds, respectively, for the true values. Hirao et al. [38] considered the Voigt and Reuss averages for elastic moduli and take the mean value of them (Hill average).

Supposing generalized Hooke's law for a single crystal, the following relations between the stress σ_{ij} and the strain ε_{kl} hold locally for each crystallite,

$$\sigma_{ij} = C_{ijkl}\varepsilon_{kl}, \tag{3.9}$$

$$\varepsilon_{ij} = S_{ijkl}\sigma_{kl}, \tag{3.10}$$

with respect to the crystallite-fixed coordinate $O - X_1 X_2 X_3$, where C_{ijkl} is the elastic stiffness and S_{ijkl} is the elastic compliance of the single crystal. They are related to each other by $C_{ijkl} = S_{ijkl}^{-1}$. On a hypothesis that the strain is uniform in the material, the average of

Eq.(3.9) over all crystallites is given by

$$\langle \sigma_{ij} \rangle = \langle C_{ijkl}\varepsilon_{kl} \rangle = \langle C_{ijkl} \rangle_V \langle \varepsilon_{kl} \rangle, \tag{3.11}$$

where the angle brackets denote an averaging process. Equation (3.11) is called the Voigt average and $\langle C_{ijkl} \rangle_V$ is the macroscopic elastic stiffness of polycrystalline aggregate. On the other hand, supposing that the stress is uniform in the material, the macroscopic elastic compliance $\langle S_{ijkl} \rangle_R$ of polycrystalline aggregate is then written as

$$\langle \varepsilon_{ij} \rangle = \langle S_{ijkl}\sigma_{kl} \rangle = \langle S_{ijkl} \rangle_R \langle \sigma_{kl} \rangle. \tag{3.12}$$

The macroscopic elastic stiffness is obtained by

$$\langle C_{ijkl} \rangle_R = \langle S_{ijkl} \rangle_R^{-1}. \tag{3.13}$$

This averaging procedure is called the Reuss average. The macroscopic elastic stiffness by the Hill average is then given by

$$\langle C_{ijkl} \rangle_H = \frac{\langle C_{ijkl} \rangle_V + \langle C_{ijkl} \rangle_R}{2}. \tag{3.14}$$

The averaging procedures for the Voigt and Reuss averages with the ODF $w(\xi, \psi, \phi)$ as a weighting function are performed by

$$\langle C_{ijkl} \rangle_V = \int_0^{2\pi} \int_0^{2\pi} \int_{-1}^1 \beta_{mi}\beta_{nj}\beta_{pk}\beta_{ql}C_{mnpq}w(\xi, \psi, \phi)d\xi d\psi d\phi, \tag{3.15}$$

$$\langle S_{ijkl} \rangle_R = \int_0^{2\pi} \int_0^{2\pi} \int_{-1}^1 \beta_{mi}\beta_{nj}\beta_{pk}\beta_{ql}S_{mnpq}w(\xi, \psi, \phi)d\xi d\psi d\phi, \tag{3.16}$$

where $\beta_{mi}\beta_{nj}\beta_{pk}\beta_{ql}$ represents the transformation tensor from the crystallite-fixed coordinate $O - X_1X_2X_3$ to the sample-fixed coordinate $O - x_1x_2x_3$. We find that $\langle C_{ijkl} \rangle_V$ and $\langle S_{ijkl} \rangle_R$ contain W_{lmn}^T up to $l = 4$ because of the orthogonality in harmonics and the tensor rank (4) of elastic stiffness and compliance for a single crystal. In other words, the ODCs W_{lmn}^T for $l > 4$ have no effect on $\langle C_{ijkl} \rangle_V$ and $\langle S_{ijkl} \rangle_R$. Although the inverse problem such as the ultrasonic pole figures requires the calculation of W_{lmn}^T from the macroscopic elastic constants obtained by the experiments, it is impossible to determine W_{lmn}^T for $l > 4$.

3.2.3 Macroscopic elastic moduli of cubic metal

We calculate the macroscopic elastic moduli for a single phase polycrystalline cubic metal. The elastic stiffness C_{ijkl} has three independent components. Since the crystallite-fixed axes

X_i coincide with the crystallographic axes [100], [010], and [001], C_{ijkl} is written in the Voigt (two index) notation as

$$
\begin{pmatrix}
C_{11} & C_{12} & C_{12} & 0 & 0 & 0 \\
 & C_{11} & C_{12} & 0 & 0 & 0 \\
 & & C_{11} & 0 & 0 & 0 \\
 & & & C_{44} & 0 & 0 \\
 & \text{sym.} & & & C_{44} & 0 \\
 & & & & & C_{44}
\end{pmatrix}.
\tag{3.17}
$$

Substituting Eqs.(3.8) and (3.17) into Eq.(3.15), the macroscopic elastic stiffness in the Voigt average $\langle C_{ijkl}\rangle_V$ is obtained. Similarly, from Eq.(3.16), the macroscopic elastic compliance in the Reuss average $\langle S_{ijkl}\rangle_R$ is obtained. Both of them are reduced to the sum of isotropic and anisotropic parts. The macroscopic elastic stiffness in the Reuss average $\langle C_{ijkl}\rangle_R$ is calculated by Eq.(3.13). Since the anisotropic part in $\langle S_{ijkl}\rangle_R$ is sufficiently smaller than the isotropic part, $\langle C_{ijkl}\rangle_R$ is also given by the sum of isotropic and anisotropic parts to the first order approximation. Finally, the macroscopic elastic stiffness for a single-phase polycrystalline cubic metal is represented in the unified expression as:

$$
\langle C_{11}\rangle_i = \lambda_i + 2\mu_i - 2a_i\delta_1,
$$
$$
\langle C_{22}\rangle_i = \lambda_i + 2\mu_i - 2a_i\delta_2,
$$
$$
\langle C_{33}\rangle_i = \lambda_i + 2\mu_i - 2a_i\delta_3,
$$
$$
\langle C_{44}\rangle_i = \mu_i + a_i\delta_4,
$$
$$
\langle C_{55}\rangle_i = \mu_i + a_i\delta_5,
\tag{3.18}
$$
$$
\langle C_{66}\rangle_i = \mu_i + a_i\delta_6,
$$
$$
\langle C_{23}\rangle_i = \lambda_i + a_i\delta_4,
$$
$$
\langle C_{31}\rangle_i = \lambda_i + a_i\delta_5,
$$
$$
\langle C_{12}\rangle_i = \lambda_i + a_i\delta_6,
$$

where the subscript i ($= V, R, H$) refers to the averaging procedure. λ_i and μ_i are the Lamé constants for an isotropic elastic solid and a_i is the anisotropy factor. They are defined by

$$
\lambda_V = C_{11} - 2C_{44} - \frac{4}{5}a_V,
$$

$$
\mu_V = C_{44} + \frac{1}{5}a_V,
$$

$$
a_V = C_{11} - C_{12} - 2C_{44},
$$

$$\lambda_R = -\frac{2\left(S_{12} + S_R/5\right)}{\left(S_{11} + 2S_{12}\right)\left(S_{44} + 4S_R/5\right)},$$

$$\mu_R = \frac{1}{S_{44} + 4S_R/5},$$

$$S_R = S_{11} - S_{12} - \frac{1}{2}S_{44}, \tag{3.19}$$

$$a_R = -4\mu_R^2 S_R,$$

$$\lambda_H = \frac{\lambda_V + \lambda_R}{2},$$

$$\mu_H = \frac{\mu_V + \mu_R}{2},$$

$$a_H = \frac{a_V + a_R}{2}.$$

The δ's in Eq.(3.18) are

$$\delta_1 = -\frac{6\sqrt{2}\pi^2}{35}\left(W_{400}^T - \frac{2\sqrt{10}}{3}W_{420}^T + \frac{\sqrt{70}}{3}W_{440}^T\right),$$

$$\delta_2 = -\frac{6\sqrt{2}\pi^2}{35}\left(W_{400}^T + \frac{2\sqrt{10}}{3}W_{420}^T + \frac{\sqrt{70}}{3}W_{440}^T\right),$$

$$\delta_3 = -\frac{16\sqrt{2}\pi^2}{35}W_{400}^T, \tag{3.20}$$

$$\delta_4 = -\frac{16\sqrt{2}\pi^2}{35}\left(W_{400}^T + \sqrt{\frac{5}{2}}W_{420}^T\right),$$

$$\delta_5 = -\frac{16\sqrt{2}\pi^2}{35}\left(W_{400}^T - \sqrt{\frac{5}{2}}W_{420}^T\right),$$

$$\delta_6 = \frac{4\sqrt{2}\pi^2}{35}\left(W_{400}^T - \sqrt{70}W_{440}^T\right).$$

The δ's, which carry the anisotropy, are dependent on each other, since they are the linear combinations of three independent ODCs:

$$\delta_1 + \delta_2 + \delta_3 = \delta_4 + \delta_5 + \delta_6,$$

$$2\delta_1 = \delta_5 + \delta_6, \tag{3.21}$$

$$2\delta_2 = \delta_4 + \delta_6,$$

$$2\delta_3 = \delta_4 + \delta_5.$$

The values for λ_i, μ_i, and a_i depend on the averaging procedures. But the bulk modulus, which is obtained from Eq.(3.18) taking account of the first expression of Eq.(3.21), is

24

Table 3.1. The elastic constants of a single crystal and polycrystallite in copper [42]. The unit of elastic constants is GPa.

Single crystal				Polycrystallite			
C_{11}	C_{12}	C_{44}		$\lambda_i + 2\mu_i$	μ_i	a_i	a_i/μ_i
			Voigt	209.9	54.64	−103.8	−1.900
168.4	121.4	75.4	Reuss	190.4	40.03	−93.9	−2.345
			Hill	200.2	47.34	−98.8	−2.088

independent of them. It means that both suppositions of the Voigt and Reuss averages are satisfied under the static hydraulic pressure. The value is common to three averages, that is $K = \lambda + 2\mu/3$.

The macroscopic elastic constants of a textured polycrystalline aggregate are given by the sum of the isotropic and the anisotropic parts. Furthermore, the latter one is the product of the anisotropy factor a_i and the ODCs W_{4m0}^T ($m = 0, 2, 4$). If the single crystal has no elastic anisotropy, $a_i = 0$. If the orientation distribution is perfectly random, $W_{4m0}^T = 0$. In these cases, the aggregate is macroscopically isotropic. The elastic constants of a single crystal and $\lambda_i + 2\mu_i$, μ_i, a_i of a polycrystallite are shown in Table 3.1 for copper [42]. The value of a_i/μ_i in the Hill average for copper is lager than the other cubic metals; for example, iron has −1.668, aluminum has −0.405, and tungsten has −0.0026. Therefore, even a weak texture may possibly cause a strong elastic anisotropy in copper polycrystallite. In a crystal with a large value of a_i/μ_i, furthermore, the values of $\lambda_i + 2\mu_i$, μ_i, and a_i differ each other depending on the averaging procedure.

3.3 Elastic stiffnesses of reference samples

We adopt the Hill average for the macroscopic elastic stiffness in reference (uncrept) sample. The explicit form of $C_{ijkl}^R = C_{ijkl}^M + \Delta C_{ijkl}^T$ is written as

$$C_{11}^R = \lambda_M + 2\mu_M + \frac{12\sqrt{2}}{35}\pi^2 a \left(W_{400}^T - \frac{2\sqrt{10}}{3}W_{420}^T + \frac{\sqrt{70}}{3}W_{440}^T \right),$$

$$C_{22}^R = \lambda_M + 2\mu_M + \frac{12\sqrt{2}}{35}\pi^2 a \left(W_{400}^T + \frac{2\sqrt{10}}{3}W_{420}^T + \frac{\sqrt{70}}{3}W_{440}^T \right),$$

$$C_{33}^R = \lambda_M + 2\mu_M + \frac{32\sqrt{2}}{35}\pi^2 a W_{400}^T,$$

$$C_{44}^R = \mu_M - \frac{16\sqrt{2}}{35}\pi^2 a \left(W_{400}^T + \sqrt{\frac{5}{2}}W_{420}^T \right),$$

$$C_{55}^R = \mu_M - \frac{16\sqrt{2}}{35}\pi^2 a \left(W_{400}^T - \sqrt{\frac{5}{2}} W_{420}^T \right), \tag{3.22}$$

$$C_{66}^R = \mu_M + \frac{4\sqrt{2}}{35}\pi^2 a \left(W_{400}^T - \sqrt{70} W_{440}^T \right),$$

$$C_{23}^R = \lambda_M - \frac{16\sqrt{2}}{35}\pi^2 a \left(W_{400}^T + \sqrt{\frac{5}{2}} W_{420}^T \right),$$

$$C_{31}^R = \lambda_M - \frac{16\sqrt{2}}{35}\pi^2 a \left(W_{400}^T - \sqrt{\frac{5}{2}} W_{420}^T \right),$$

$$C_{12}^R = \lambda_M + \frac{4\sqrt{2}}{35}\pi^2 a \left(W_{400}^T - \sqrt{70} W_{440}^T \right),$$

where the notations are recast as

$$C_{ijkl}^R = \langle C_{ijkl} \rangle_H, \qquad \lambda_M = \lambda_H, \qquad \mu_M = \mu_H, \qquad a = a_H. \tag{3.23}$$

The numerical calculation requires the elastic stiffnesses of reference samples. We attempt to obtain them from the measured velocities. The velocities are related to C_{ijkl}^R through

$$\rho_R(V_{11}^R)^2 = C_{11}^R, \qquad \rho_R(V_{22}^R)^2 = C_{22}^R, \qquad \rho_R(V_{33}^R)^2 = C_{33}^R,$$
$$\rho_R(V_{23}^R)^2 = C_{44}^R, \qquad \rho_R(V_{31}^R)^2 = C_{55}^R, \qquad \rho_R(V_{12}^R)^2 = C_{66}^R, \tag{3.24}$$

where V_{23}^R, V_{31}^R, and V_{12}^R are the averages of measured velocities: $(V_{23}^R + V_{32}^R)/2$, $(V_{31}^R + V_{13}^R)/2$, and $(V_{12}^R + V_{21}^R)/2$.

The density was obtained as $\rho_R = 8.89 \times 10^3$ kg/m^3 from mass and volume measurements. We adopted the bulk modulus $K_M = 137$ GPa from Table 3.1, which is independent of the averaging procedures. These values gave the shear modulus as $\mu_M = 46.5$ GPa through an equation

$$\rho_R\{(V_{11}^R)^2 + (V_{22}^R)^2 + (V_{33}^R)^2 + 2(V_{23}^R)^2 + 2(V_{31}^R)^2 + 2(V_{12}^R)^2\} = 3K_M + 10\mu_M. \tag{3.25}$$

The equation is independent of the ODCs, and is based on the fact that $\rho_R\{(V_{11}^R)^2 + (V_{12}^R)^2 + (V_{31}^R)^2\}$, $\rho_R\{(V_{12}^R)^2 + (V_{22}^R)^2 + (V_{23}^R)^2\}$, and $\rho_R\{(V_{31}^R)^2 + (V_{23}^R)^2 + (V_{33}^R)^2\}$ are all equal to $K_M + 10\mu_M/3$. We adopted the above equation to minimize the measuring errors in the velocities. We obtained $\lambda_M = 106$ GPa from $\lambda_M = K_M - 2\mu_M/3$.

We have six velocities for three unknown ODCs. We define an error function as

$$E = \sum_{i=1}^{6} \left\{ \rho_R \left(V_i^R \right)^2 - C_i^R \right\}^2, \tag{3.26}$$

26

where V_i^R denotes the measured velocities in the reference samples, having six independent values, and C_i^R is the calculated stiffness corresponding to the velocity. Although the ODCs W_{4m0}^T cannot be determined, the products of the anisotropy factor and the ODCs (aW_{4m0}^T) can be determined so as to minimize E. Because C_i^R is given by the linear combination of the three unknowns aW_{4m0}^T, the function E is a quadratic surface in a four-dimensional space, and has only one minimum. The minimum is found by the simultaneous equations of partial derivatives $\partial E / \partial (aW_{4m0}^T) = 0$. Calculated results were

$$aW_{400}^T = 1.40 \times 10^{-2} \text{ GPa},$$

$$aW_{420}^T = -6.96 \times 10^{-3} \text{ GPa}, \tag{3.27}$$

$$aW_{440}^T = -5.53 \times 10^{-2} \text{ GPa}.$$

These values gave the velocities as listed in Table 3.2, for which $E_{\min} = 1.47 \times 10^{-2} \text{ (GPa)}^2$.

The macroscopic stiffness C_{ijkl}^R is written in a simple form as $C_{ijkl}^R = C_{ijkl}^M + \Delta C_{ijkl}^T$. According to the calculation, they take the values of

$$C_{11}^M = C_{22}^M = C_{33}^M = 199 \text{ GPa},$$

$$C_{44}^M = C_{55}^M = C_{66}^M = 46.5 \text{ GPa}, \tag{3.28}$$

$$C_{23}^M = C_{31}^M = C_{12}^M = 106 \text{ GPa},$$

and

$$\Delta C_{11}^T = -0.60 \text{ GPa},$$

$$\Delta C_{22}^T = -0.74 \text{ GPa},$$

$$\Delta C_{33}^T = 0.18 \text{ GPa},$$

$$\Delta C_{44}^T = \Delta C_{23}^T = -0.02 \text{ GPa}, \tag{3.29}$$

$$\Delta C_{55}^T = \Delta C_{31}^T = -0.16 \text{ GPa},$$

$$\Delta C_{66}^T = \Delta C_{12}^T = 0.76 \text{ GPa}.$$

The maximum ratio is $\Delta C_{66}^T / C_{66}^M = 0.016$. The deviation stiffness ΔC_{ijkl}^T is much smaller than the isotropic stiffness C_{ijkl}^M. It supports the theoretical assumption (4), and allows us

Table 3.2. Agreement between measured and calculated velocities in reference samples. (unit:m/s)

	V_{11}^R	V_{22}^R	V_{33}^R	V_{23}^R	V_{31}^R	V_{12}^R
Measured	4725.6	4722.5	4734.0	2284.7	2284.2	2305.5
Calculated	4724.8	4723.1	4734.1	2286.1	2282.7	2305.2

to express the macroscopic stiffness in damaged sample as $C^*_{ijkl} = C^M_{ijkl} + \Delta C^T_{ijkl} + \Delta C^V_{ijkl}$. The isotropic matrix is supposable in the calculation of the effective stiffness for the damaged samples.

3.4 Effect of texture on normalized velocities

We now discuss the effect of texture on normalized velocities. The six independent velocities are given by

$$V_i^R = \sqrt{\frac{C_i^R}{\rho_R}} = \sqrt{\frac{C_i^M + \Delta C_i^T}{\rho_R}}, \tag{3.30}$$

$$V_i^* = \sqrt{\frac{C_i^*}{\rho_*}} = \sqrt{\frac{C_i^M + \Delta C_i^T + \Delta C_i^V}{\rho_*}}, \tag{3.31}$$

where $i = 1, 2, \ldots 6$, and C_i^M, ΔC_i^T, and ΔC_i^V are the stiffnesses corresponding to the velocities. Considering that the magnitudes of two deviation stiffnesses are sufficiently small compared with C_{ijkl}^M, the normalized velocities reduce to

$$\frac{V_i^*}{V_i^R} = \sqrt{\frac{1}{1-c}\frac{C_i^C}{C_i^M}}, \tag{3.32}$$

within the first order approximation, where $C_{ijkl}^C = C_{ijkl}^M + \Delta C_{ijkl}^V$. This implies that the texture effect ΔC_{ijkl}^T has been excluded in the normalized velocities.

Numerical examples are presented below. The normalized velocity V_{12}^*/V_{12}^R at $c = 0.02$ is calculated as 0.9803 using the fitting curve in Fig. 2.7. The void effect ΔC_{66}^V is estimated to be -2.75 GPa from Eqs.(3.28)-(3.31). Substituting the value into Eq.(3.32), we obtain $V_{12}^*/V_{12}^R = 0.9798$. The difference of 0.0005 falls into the measuring errors. The difference for V_{33}^*/V_{33}^R at $c = 0.015$ is found to be 0.0002.

3.5 Summary

For the simple procedure to deal with the anisotropic matrix of damaged composite, we used the theory of polycrystalline aggregate. We gave the expression of the macroscopic elastic stiffness in reference sample used in the experiment in chapter 2 as the Hill average for the single-phase polycrystallite cubic metal having statistically the orthorhombic symmetry (rolling texture). The expression was used for the numerical calculation to determine C_{ijkl}^M

and ΔC_{ijkl}^T. The theoretical assumption (4) was supported by $|\Delta C_{ijkl}^T/C_{ijkl}^M| \ll 1$, indicating that the expression of $C_{ijkl}^* = C_{ijkl}^M + \Delta C_{ijkl}^T + \Delta C_{ijkl}^V$ is acceptable for the approximated effective stiffness in damaged samples. We also conclude that the texture effect is absent in the normalized velocities. We will consider only the effective stiffness $C_{ijkl}^C = C_{ijkl}^M + \Delta C_{ijkl}^V$ for the isotropic copper-matrix/voids composite in the modeling studies. The concept of orientation distribution function, ODF, will be adopted to express the inclusion orientation distribution in section 4.5.

The theory of quantitative texture analysis is summarized as follows. A probability density of the crystallographic orientation is represented by the crystallite-ODF. The ODF is expanded by the generalization of associated Legendre functions Z_{lmn}. The coefficients of the expansion, W_{lmn}^T, are called crystallite orientation distribution coefficients, crystallite-ODCs. We use three simple averaging procedures, Voigt, Reuss, and Hill, to obtain the macroscopic elastic moduli. The Voigt and Reuss averages provide the upper and lower bounds, respectively, for the true values. The Hill average is given as the average of them. The macroscopic elastic constants of a textured polycrystalline aggregate are given by the sum of the isotropic and anisotropic parts. Furthermore, the latter is the product of the anisotropy factor, caused by the anisotropy of single crystal, and the ODCs. Three independent ODCs, W_{400}^T, W_{420}^T, and W_{440}^T play an important role in the macroscopic elastic moduli of polycrystallite cubic metals with the rolling texture. Even a weak texture may possibly cause a strong elastic anisotropy in copper polycrystallite. The values of $\lambda_i + 2\mu_i$, μ_i, and a_i differ each other greatly depending on the averaging procedure.

Chapter 4

THEORETICAL CASE STUDIES ON VOID EFFECT

4.1 Introduction

Theoretical case studies on the void effect are described in this chapter. Following the simplification and the conclusion in chapter 3, the isotropic matrix is supposed. The effective stiffness of the composite $C_{ijkl}^C = C_{ijkl}^M + \Delta C_{ijkl}^V$ will be obtained for three cases. They will be applied to the creep damage modeling studies in next chapter.

The present treatment draws much on the previous work, especially of Tandon and Weng [18]. They derived the effective elastic moduli for a composite with unidirectionally aligned spheroidal inclusions. The derivation was carried out by the combination of Eshelby's equivalent inclusion [7] and Mori-Tanaka's average stress [16]. The result is appropriate for the full range, from the dilute to the dense concentration.

We begin with the basic theory for the effective moduli. The effect of the inclusion shape (aspect ratio) is represented by the Eshelby's transformation tensor. Substituting the explicit form of the tensor, the spherical inclusions (case A), and the oblate or prolate inclusions with unidirectional alignment (case B) are considered. Partial orientation is considered in case C as a modified version of the case B by using the orientation distribution function (ODF).

4.2 Basic theory

A composite model is shown in Fig. 4.1(a), where the spheroidal inclusions are embedded in the infinite elastic matrix. We adopt the coordinate systems analogous to the previous chapter. The composite-sample fixed axes are taken to be $O - x_1 x_2 x_3$, and the inclusion fixed axes $O - X_1 X_2 X_3$. The domain of an ellipsoidal inclusion is bounded by

$$\frac{X_1^2}{a_1^2} + \frac{X_2^2}{a_2^2} + \frac{X_3^2}{a_3^2} = 1, \tag{4.1}$$
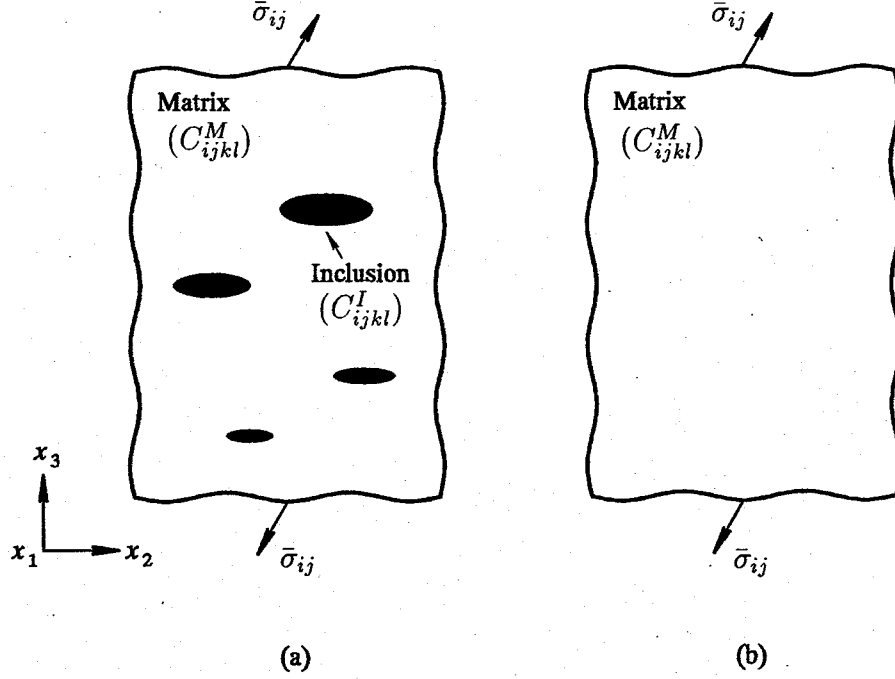
Fig. 4.1. A composite model and a comparison material.

where a_1, a_2, and a_3 are the principal radii of the ellipsoid along the X_1, X_2, and X_3 axes, respectively. The inclusions are spheroid, that is $a_1 = a_2$. We first consider the case that the principal axis of inclusions a_3 is unidirectionally aligned along the x_3 direction and the two coordinate systems coincide each other.

It is assumed that the matrix and the inclusion materials are both linearly elastic, isotropic, and homogeneous. We further assume that the inclusions are randomly positioned in the matrix. Thus the composite is regarded to be macroscopically homogeneous. The elastic stiffness tensor of the matrix is denoted by C_{ijkl}^M, and that of inclusions is given by C_{ijkl}^I. We now prescribe a surface traction on the boundary of the composite to give a uniform stress $\bar{\sigma}_{ij}$. We introduce an identically shaped matrix, as shown in Fig. 4.1(b), as a comparison material, being subjected to the same boundary stress. If we denote the still unknown effective stiffness tensor of the composite by C_{ijkl}^C, the strain of the composite $\bar{\varepsilon}_{ij}$ and of the comparison material ε_{ij}^M will be related to the applied stress $\bar{\sigma}_{ij}$ by

$$\bar{\sigma}_{ij} = C_{ijkl}^C \bar{\varepsilon}_{kl}, \tag{4.2}$$

$$\bar{\sigma}_{ij} = C_{ijkl}^M \varepsilon_{kl}^M, \tag{4.3}$$

where the summation convention for a repeated index from 1 to 3 is implied.

In general, the strain in the matrix is not equal to ε_{kl}^M, and it is a function of the position.

A certain perturbed strain $\tilde{\varepsilon}_{kl}$ from ε_{kl}^M averaged over the matrix is introduced due to the presence of inclusions. Note that $\bar{\varepsilon}_{kl} \neq \varepsilon_{kl}^M + \tilde{\varepsilon}_{kl}$, $\bar{\varepsilon}_{kl}$ is the strain averaged over the composite, and $\varepsilon_{kl}^M + \tilde{\varepsilon}_{kl}$ is the strain averaged over the matrix. This perturbed strain corresponds to an average perturbed stress, denoted by $\tilde{\sigma}_{ij}$, in the matrix; through the elastic moduli C_{ijkl}^M,

$$\tilde{\sigma}_{ij} = C_{ijkl}^M \tilde{\varepsilon}_{kl}. \tag{4.4}$$

Thus, under a given $\bar{\sigma}_{ij}$, the average stress in the matrix is now given by $\bar{\sigma}_{ij} + \tilde{\sigma}_{ij}$ and its average strain is $\varepsilon_{ij}^M + \tilde{\varepsilon}_{ij}$. These quantities are related to each other by

$$\bar{\sigma}_{ij} + \tilde{\sigma}_{ij} = C_{ijkl}^M \left(\varepsilon_{kl}^M + \tilde{\varepsilon}_{kl} \right). \tag{4.5}$$

This concept was originally introduced by Mori and Tanaka [16].

We denote by σ_{ij}^{pt} the average perturbed stress component in the inclusions from the average stress $\bar{\sigma}_{ij} + \tilde{\sigma}_{ij}$ in the matrix, and the corresponding perturbed strain by ε_{ij}^{pt}. Thus the average perturbed stress $\tilde{\sigma}_{ij}$ has a common value in the matrix and the inclusions. The stress-strain relation in the inclusions is then

$$\bar{\sigma}_{ij} + \tilde{\sigma}_{ij} + \sigma_{ij}^{pt} = C_{ijkl}^I \left(\varepsilon_{kl}^M + \tilde{\varepsilon}_{kl} + \varepsilon_{kl}^{pt} \right). \tag{4.6}$$

According to Eshelby [7] this relation is rewritten using the elastic stiffness in the matrix and "equivalent transformation strain" ε_{ij}^* as

$$\bar{\sigma}_{ij} + \tilde{\sigma}_{ij} + \sigma_{ij}^{pt} = C_{ijkl}^M \left(\varepsilon_{kl}^M + \tilde{\varepsilon}_{kl} + \varepsilon_{kl}^{pt} - \varepsilon_{kl}^* \right), \tag{4.7}$$

with the transformation of

$$\varepsilon_{kl}^{pt} = S_{klmn} \varepsilon_{mn}^*, \tag{4.8}$$

where S_{ijkl} is Eshelby's transformation tensor; its components depend on the aspect ratio of the inclusions and the elastic moduli of the matrix. The tensor S_{ijkl} satisfies the symmetry relations of

$$S_{ijkl} = S_{jikl} = S_{ijlk}.$$

The explicit forms of S_{ijkl} will be given later. From Eqs.(4.5) and (4.7),

$$\sigma_{ij}^{pt} = C_{ijkl}^M \left(\varepsilon_{kl}^{pt} - \varepsilon_{kl}^* \right) \tag{4.9}$$

is obtained.

The volume of the matrix is denoted by v_M, and that of the inclusions is denoted by v_I; then that of the composite is given by $v = v_M + v_I$. Since the average of stresses over the composite should be $\bar{\sigma}_{ij}$, one has

$$\bar{\sigma}_{ij} = \frac{1}{v} \left\{ \int_{v_M} (\bar{\sigma}_{ij} + \tilde{\sigma}_{ij})\, dv + \int_{v_I} \left(\bar{\sigma}_{ij} + \tilde{\sigma}_{ij} + \sigma_{ij}^{pt} \right) dv \right\}.$$

Note that $\tilde{\sigma}_{ij}$ and σ_{ij}^{pt} are the average values over the composite and inclusions, respectively. They are independent of the position. The equation, therefore, reduces to

$$\tilde{\sigma}_{ij} + c\sigma_{ij}^{pt} = 0, \tag{4.10}$$

where $c = v_I/v$ is the volume fraction of the inclusions. Substituting Eqs.(4.4) and (4.9) into Eq.(4.10), we obtain the average perturbed strain in the matrix

$$\tilde{\varepsilon}_{kl} = -c \left(\varepsilon_{kl}^{pt} - \varepsilon_{kl}^* \right), \tag{4.11}$$

for arbitrary C_{ijkl}^M. On the other hand, the strain of the composite $\bar{\varepsilon}_{ij}$ in Eq.(4.2) is given by the volume average of strains over its matrix and inclusions:

$$\bar{\varepsilon}_{kl} = \varepsilon_{kl}^M + \tilde{\varepsilon}_{kl} + c\varepsilon_{kl}^{pt}. \tag{4.12}$$

Substituting Eq.(4.11) into the above equation, it simply reduces to

$$\bar{\varepsilon}_{kl} = \varepsilon_{kl}^M + c\varepsilon_{kl}^*. \tag{4.13}$$

From Eqs.(4.6), (4.7), (4.8), and (4.11), we obtain

$$\left(C_{ijkl}^I - C_{ijkl}^M \right) \left\{ \varepsilon_{kl}^M + (1-c)S_{klmn}\varepsilon_{mn}^* + c\varepsilon_{kl}^* \right\} + C_{ijkl}^M \varepsilon_{kl}^* = 0, \tag{4.14}$$

to calculate the equivalent transformation strain ε_{kl}^* in terms of ε_{kl}^M.

Conclusively, the effective elastic moduli of the composite C_{ijkl}^C is calculated from Eqs. (4.2), (4.3), (4.13), and (4.14).

4.3   Case A −Spherical inclusions−

When the inclusions are spherical ($a_1 = a_2 = a_3$), the effective elastic moduli of the composite are also isotropic, thus the moduli have two independent components. Eshelby's

tensor S_{ijkl} is written as follows;

$$S_{1111} = S_{2222} = S_{3333} = \frac{7 - 5\nu_M}{15(1 - \nu_M)},$$

$$S_{1122} = S_{2233} = S_{3311} = S_{1133} = S_{2211} = S_{3322} = \frac{5\nu_M - 1}{15(1 - \nu_M)}, \quad (4.15)$$

$$S_{1212} = S_{2323} = S_{3131} = \frac{4 - 5\nu_M}{15(1 - \nu_M)},$$

where ν_M is Poisson's ratio of matrix.

The elastic stiffness of the matrix and inclusions can be written as

$$C_{ijkl}^M = K_M \delta_{ij}\delta_{kl} + \mu_M \left(\delta_{ik}\delta_{jl} + \delta_{il}\delta_{jk} - \frac{2}{3}\delta_{ij}\delta_{kl} \right), \quad (4.16)$$

$$C_{ijkl}^I = K_I \delta_{ij}\delta_{kl} + \mu_I \left(\delta_{ik}\delta_{jl} + \delta_{il}\delta_{jk} - \frac{2}{3}\delta_{ij}\delta_{kl} \right), \quad (4.17)$$

where K_M and μ_M, K_I and μ_I are the bulk modulus and shear modulus of the matrix and inclusions, respectively, and δ_{ij} is the Kronecker delta, having the property $\delta_{ij} = 1$ when $i = j$ and $\delta_{ij} = 0$ when $i \neq j$. Taking account of the symmetry property of Eshelby's transformation tensor Eq.(4.15), Eq.(4.14) is simply reduced to

$$\varepsilon_{kk}^* = -\frac{\varepsilon_{kk}^M}{\dfrac{K_M}{K_I - K_M} + c + (1 - c)\left(S_{1111} + 2S_{1122} \right)}, \quad (4.18)$$

$$\varepsilon_{12}^* = -\frac{\varepsilon_{12}^M}{\dfrac{\mu_M}{\mu_I - \mu_M} + c + 2(1 - c)S_{1212}}. \quad (4.19)$$

4.3.1 Bulk modulus

We consider the state of static hydraulic pressure

$$\bar{\sigma}_{11} = \bar{\sigma}_{22} = \bar{\sigma}_{33} = \bar{\sigma}.$$

The strain components of the comparison material in Eq.(4.3) are

$$\varepsilon_{11}^M = \varepsilon_{22}^M = \varepsilon_{33}^M = \varepsilon^M.$$

Then, the stress-strain relations of Eqs.(4.2) and (4.3) are written as

$$\bar{\sigma} = 3K_C\bar{\varepsilon} = K_C\bar{\varepsilon}_{kk},$$

$$\bar{\sigma} = 3K_M\varepsilon^M = K_M\varepsilon_{kk}^M,$$

where K_C is the effective bulk modulus of the composite. They can be combined as

$$\frac{K_C}{K_M} = \frac{\varepsilon_{kk}^M}{\bar{\varepsilon}_{kk}}.$$

Substituting Eq.(4.18) into Eq.(4.13), $\bar{\varepsilon}_{kk}$ is represented in terms of ε_{kk}^M:

$$\bar{\varepsilon}_{kk} = \frac{\dfrac{K_M}{K_I - K_M} + (1 - c)(S_{1111} + 2S_{1122})}{\dfrac{K_M}{K_I - K_M} + c + (1 - c)(S_{1111} + 2S_{1122})} \varepsilon_{kk}^M.$$

Using $S_{1111} + 2S_{1122} = 3K_M/(3K_M + 4\mu_M)$, we obtain the effective bulk modulus K_C as

$$\frac{K_C}{K_M} = 1 + \frac{c}{\dfrac{K_M}{K_I - K_M} + (1 - c)\dfrac{3K_M}{3K_M + 4\mu_M}}. \tag{4.20}$$

In the case of dilute suspension $c \ll 1$, it reduces to

$$\frac{K_C}{K_M} = 1 + \frac{c}{\dfrac{K_M}{K_I - K_M} + \dfrac{3K_M}{3K_M + 4\mu_M}}. \tag{4.21}$$

Equation (4.21) coincides with Dewey's result [6] derived by a classical theory of elasticity. It represents the proportional change in the effective bulk modulus K_C with the inclusion volume fraction c.

4.3.2 Shear modulus

We apply a pure shear stress

$$\bar{\sigma}_{12} = \bar{\sigma}_{21} \neq 0, \qquad \bar{\sigma}_{31} = \bar{\sigma}_{13} = \bar{\sigma}_{23} = \bar{\sigma}_{32} = 0.$$

The strain components of the comparison material in Eq.(4.3) are

$$\varepsilon_{12}^M = \varepsilon_{21}^M \neq 0, \qquad \varepsilon_{31}^M = \varepsilon_{13}^M = \varepsilon_{23}^M = \varepsilon_{32}^M = 0.$$

Equations (4.2) and (4.3) are combined as

$$\frac{\mu_C}{\mu_M} = \frac{\varepsilon_{12}^M}{\bar{\varepsilon}_{12}},$$

where μ_C is the effective shear modulus of the composite. Substituting Eq.(4.19) into Eq.(4.13), $\bar{\varepsilon}_{12}$ is represented in terms of ε_{12}^M:

$$\bar{\varepsilon}_{12} = \frac{\dfrac{\mu_M}{\mu_I - \mu_M} + 2(1 - c)S_{1212}}{\dfrac{\mu_M}{\mu_I - \mu_M} + c + 2(1 - c)S_{1212}} \varepsilon_{12}^M.$$

Using Eq.(4.15)$_3$, we obtain the effective shear modulus μ_C as

$$\frac{\mu_C}{\mu_M} = 1 + \frac{15(1 - \nu_M)(\mu_I - \mu_M)c}{15\mu_M(1 - \nu_M) + 2(4 - 5\nu_M)(\mu_I - \mu_M)(1 - c)}. \tag{4.22}$$

In the case of dilute suspension $c \ll 1$, it reduces to

$$\frac{\mu_C}{\mu_M} = 1 - \frac{15(1 - \nu_M)\left(1 - \dfrac{\mu_I}{\mu_M}\right)c}{7 - 5\nu_M + 2(4 - 5\nu_M)\dfrac{\mu_I}{\mu_M}}. \tag{4.23}$$

Equation (4.23) coincides again with Dewey's result [6].

4.3.3 Numerical results and discussions

A numerical calculation for the effective bulk and shear modulus for spherical-void/copper composite is shown in Fig. 4.2, where six models are compared with each other. The calculation
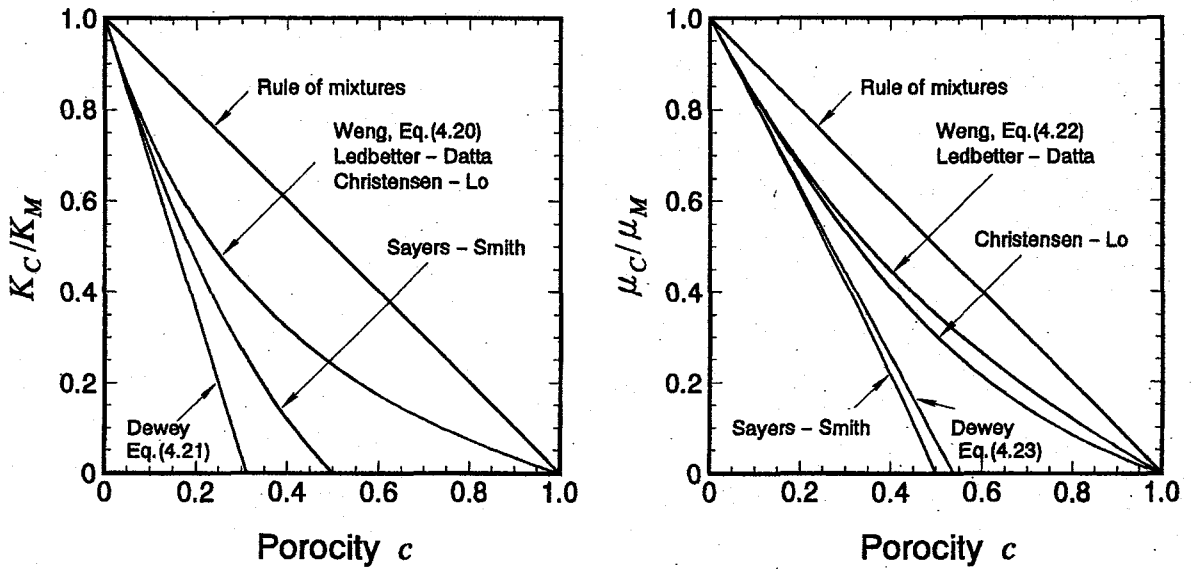
Fig. 4.2. Effective moduli of spherical-void/copper composite.

supposes $K_M = 137$ GPa and $\mu_M = 46.5$ GPa, which are the values in the reference samples calculated in section 3.3. The elastic constants of voids are, of course, $K_I = \mu_I = 0$. The horizontal axis porosity c is the void volume fraction. The rule of mixtures is the arithmetic average of elastic constants of its constituents weighting by the volume fraction. Weng's results [17] are given by Eqs.(4.20) and (4.22). Dewey's results [6] are from Eqs.(4.21) and (4.23) for a dilute suspension. The results of Christensen-Lo [11] are obtained by the three phase model as an approximation for a non-dilute suspension. The results of Sayers-Smith [43] and Ledbetter-Datta [44] are both obtained by the scattering theory of elastic waves. The limitation of the models by Dewey and Sayers-Smith is $c \ll 1$. The model by Christensen-Lo has a less strict limitation. The models by Weng and Ledbtter-Datta cover the whole range of $0 \le c \le 1$, but there remains the discussion for $c \approx 1$ because of the contact or coalescence of the inclusions.

As shown in the figure, the rule of mixtures is far away from the others. The models by Weng and Ledbetter-Datta coincide numerically with each other over whole range. The other models, due to Dewey, Sayers-Smith, and Christensen-Lo are asymptotical to Weng and Ledbetter-Datta as c decreases. Moreover, the effective bulk modulus by Christensen-Lo coincides with Weng and Ledbetter-Datta over the whole range. It can be estimated from this calculation that the use of Dewey and Sayers-Smith is limited to $c < 0.05$ and that of Christensen-Lo to $c < 0.15$.

4.4 Case B −Unidirectionally aligned spheroidal inclusions−

When the inclusions are spheroid, Eshelby's tensor S_{ijkl} is written as follows;

$$S_{1111} = S_{2222} = -\frac{3}{8(1-\nu_M)}\frac{\alpha^2}{1-\alpha^2} + \frac{1}{4(1-\nu_M)}\left\{1 - 2\nu_M + \frac{9}{4(1-\alpha^2)}\right\}g,$$

$$S_{3333} = \frac{1}{2(1-\nu_M)}\left(4 - 2\nu_M - \frac{2}{1-\alpha^2}\right) + \frac{1}{2(1-\nu_M)}\left(-4 + 2\nu_M + \frac{3}{1-\alpha^2}\right)g,$$

$$S_{1122} = S_{2211} = \frac{1}{8(1-\nu_M)}\left(1 - \frac{1}{1-\alpha^2}\right) + \frac{1}{16(1-\nu_M)}\left\{-4(1-2\nu_M) + \frac{3}{1-\alpha^2}\right\}g,$$

$$S_{1133} = S_{2233} = \frac{1}{2(1-\nu_M)}\frac{\alpha^2}{1-\alpha^2} - \frac{1}{4(1-\nu_M)}\left(1 - 2\nu_M + \frac{3\alpha^2}{1-\alpha^2}\right)g, \qquad (4.24)$$

$$S_{3311} = S_{3322} = \frac{1}{2(1-\nu_M)}\left\{-(1-2\nu_M) + \frac{1}{1-\alpha^2}\right\} + \frac{1}{4(1-\nu_M)}\left\{2(1-2\nu_M) - \frac{3}{1-\alpha^2}\right\}g,$$

$$S_{1212} = -\frac{1}{8(1-\nu_M)}\frac{\alpha^2}{1-\alpha^2} + \frac{1}{16(1-\nu_M)}\left\{4(1-2\nu_M) + \frac{3}{1-\alpha^2}\right\}g,$$

$$S_{1313} = S_{2323} = \frac{1}{4(1-\nu_M)}\left(1 - 2\nu_M + \frac{1+\alpha^2}{1-\alpha^2}\right) - \frac{1}{8(1-\nu_M)}\left\{1 - 2\nu_M + 3\left(\frac{1+\alpha^2}{1-\alpha^2}\right)\right\}g,$$

where α is the aspect ratio of the spheroid and

$$g = \begin{cases} \alpha\left(\cos^{-1}\alpha - \alpha\sqrt{1-\alpha^2}\right)/\left(1-\alpha^2\right)^{3/2} & \text{Oblate: } \alpha = a_3/a_1 < 1 \\ \alpha\left(\alpha\sqrt{\alpha^2-1} - \cosh^{-1}\alpha\right)/\left(\alpha^2-1\right)^{3/2} & \text{Prolate: } \alpha = a_3/a_1 > 1 \end{cases}$$

The elastic stiffness of the matrix and inclusions are written as

$$C_{ijkl}^M = \lambda_M \delta_{ij}\delta_{kl} + \mu_M \left(\delta_{ik}\delta_{jl} + \delta_{il}\delta_{jk}\right), \tag{4.25}$$

$$C_{ijkl}^I = \lambda_I \delta_{ij}\delta_{kl} + \mu_I \left(\delta_{ik}\delta_{jl} + \delta_{il}\delta_{jk}\right), \tag{4.26}$$

where $\lambda_M = K_M - 2\mu_M/3$ and μ_M, $\lambda_I = K_I - 2\mu_I/3$ and μ_I are the Lamé constants of the matrix and inclusions, respectively. The symmetry axes of spheroids are all aligned along the sample coordinate x_3. The composite is then macroscopically transverse isotropic in the $x_1 x_2$ plane, and the effective moduli have five independent components.

To find the ε_{ij}^* components, we first set $ij = 11$, 22, and 33 in Eq.(4.14). Taking account of the symmetry property of Eshelby's transformation tensor in Eq.(4.24), we have

$$D_1\varepsilon_{11}^M + \varepsilon_{22}^M + \varepsilon_{33}^M + B_1\varepsilon_{11}^* + B_2\varepsilon_{22}^* + B_3\varepsilon_{33}^* = 0, \tag{4.27}$$

$$\varepsilon_{11}^M + D_1\varepsilon_{22}^M + \varepsilon_{33}^M + B_2\varepsilon_{11}^* + B_1\varepsilon_{22}^* + B_3\varepsilon_{33}^* = 0, \tag{4.28}$$

$$\varepsilon_{11}^M + \varepsilon_{22}^M + D_1\varepsilon_{33}^M + B_4\left(\varepsilon_{11}^* + \varepsilon_{22}^*\right) + B_5\varepsilon_{33}^* = 0, \tag{4.29}$$

where

$$\begin{aligned} B_1 &= cD_1 + D_2 + (1-c)\left(D_1 S_{1111} + S_{1122} + S_{3311}\right), \\ B_2 &= c + D_3 + (1-c)\left(S_{1111} + D_1 S_{1122} + S_{3311}\right), \\ B_3 &= c + D_3 + (1-c)\left\{(1+D_1)S_{1133} + S_{3333}\right\}, \\ B_4 &= c + D_3 + (1-c)\left(S_{1111} + S_{1122} + D_1 S_{3311}\right), \\ B_5 &= cD_1 + D_2 + (1-c)\left(2S_{1133} + D_1 S_{3333}\right), \end{aligned} \tag{4.30}$$

and

$$D_1 = 1 + 2\frac{\mu_I - \mu_M}{\lambda_I - \lambda_M},$$

$$D_2 = \frac{\lambda_M + 2\mu_M}{\lambda_I - \lambda_M}, \tag{4.31}$$

$$D_3 = \frac{\lambda_M}{\lambda_I - \lambda_M}.$$

Solving Eqs.(4.27)-(4.29) simultaneously, we obtain

$$\varepsilon_{11}^* = \frac{1}{2A_1}\left\{(A_2 - A_3A_1)\varepsilon_{11}^M + (A_2 + A_3A_1)\varepsilon_{22}^M + 2A_4\varepsilon_{33}^M\right\},\qquad(4.32)$$

$$\varepsilon_{22}^* = \frac{1}{2A_1}\left\{(A_2 + A_3A_1)\varepsilon_{11}^M + (A_2 - A_3A_1)\varepsilon_{22}^M + 2A_4\varepsilon_{33}^M\right\},\qquad(4.33)$$

$$\varepsilon_{33}^* = \frac{1}{A_1}\left\{A_5\left(\varepsilon_{11}^M + \varepsilon_{22}^M\right) + A_6\varepsilon_{33}^M\right\},\qquad(4.34)$$

where

$$
\begin{aligned}
A_1 &= 2B_3B_4 - B_5(B_1 + B_2),\\[4pt]
A_2 &= (1 + D_1)B_5 - 2B_3,\\[4pt]
A_3 &= \frac{1 - D_1}{B_2 - B_1},\\[4pt]
A_4 &= B_5 - D_1B_3,\\[4pt]
A_5 &= B_1 + B_2 - (1 + D_1)B_4,\\[4pt]
A_6 &= D_1(B_1 + B_2) - 2B_4.
\end{aligned}
\qquad(4.35)
$$

Similarly, setting $ij = 23$, 31, and 12 in Eq.(4.14), one finds

$$\varepsilon_{23}^* = -\frac{\varepsilon_{23}^M}{\dfrac{\mu_M}{\mu_I - \mu_M} + c + 2(1 - c)S_{2323}},\qquad(4.36)$$

$$\varepsilon_{31}^* = -\frac{\varepsilon_{31}^M}{\dfrac{\mu_M}{\mu_I - \mu_M} + c + 2(1 - c)S_{3131}},\qquad(4.37)$$

$$\varepsilon_{12}^* = -\frac{\varepsilon_{12}^M}{\dfrac{\mu_M}{\mu_I - \mu_M} + c + 2(1 - c)S_{1212}}.\qquad(4.38)$$

Although we will derive eight effective constants, they are connected with each other and only five effective constants are independent.

4.4.1 Young's moduli

Apply the unidirectional stress in the x_3 direction,

$$\bar{\sigma}_{33} \neq 0, \qquad \bar{\sigma}_{11} = \bar{\sigma}_{22} = 0.$$

40

The strain components in the comparison material, from Eq.(4.3), are

$$\varepsilon_{33}^M = \bar{\sigma}_{33}/E_M, \qquad \varepsilon_{11}^M = \varepsilon_{22}^M = -\nu_M \varepsilon_{33}^M, \tag{4.39}$$

where E_M and ν_M are Young's modulus and Poisson's ratio of matrix, respectively. Then, Eqs.(4.2) and (4.3) are written as

$$\bar{\sigma}_{33} = E_{33}^C \bar{\varepsilon}_{33}, \qquad \bar{\sigma}_{33} = E_M \varepsilon_{33}^M,$$

where E_{33}^C is effective Young's modulus along the x_3 direction. They are combined as

$$\frac{E_{33}^C}{E_M} = \frac{\varepsilon_{33}^M}{\bar{\varepsilon}_{33}}. \tag{4.40}$$

Substituting Eq.(4.39)$_2$ into Eq.(4.34), we obtain

$$\varepsilon_{33}^* = \frac{1}{A_1}\left(-2\nu_M A_5 + A_6\right)\varepsilon_{33}^M. \tag{4.41}$$

Substituting this equation into Eq.(4.13), one finds

$$\bar{\varepsilon}_{33} = \left\{1 + c\left(-2\nu_M A_5 + A_6\right)/A_1\right\}\varepsilon_{33}^M. \tag{4.42}$$

Finally, from Eqs.(4.40) and (4.42), we obtain

$$\frac{E_{33}^C}{E_M} = \frac{1}{1 + c\left(-2\nu_M A_5 + A_6\right)/A_1}. \tag{4.43}$$

By the similar procedure, we obtain effective Young's modulus E_{11}^C along the x_1 direction, which is exactly the same as E_{22}^C, as

$$\frac{E_{11}^C}{E_M} = \frac{1}{1 + c\left\{(1 - \nu_M)A_2 - (1 + \nu_M)A_3 A_1 - 2\nu_M A_4\right\}/2A_1}. \tag{4.44}$$

4.4.2 Shear moduli

We apply the pure shear stress

$$\bar{\sigma}_{23} = \bar{\sigma}_{32} \neq 0, \qquad \bar{\sigma}_{31} = \bar{\sigma}_{13} = \bar{\sigma}_{12} = \bar{\sigma}_{21} = 0.$$

Then, Eqs.(4.2) and (4.3) are written as

$$\bar{\sigma}_{23} = 2\mu_{23}^C \bar{\varepsilon}_{23}, \qquad \bar{\sigma}_{23} = 2\mu_M \varepsilon_{23}^M,$$

41

where μ_{23}^C is the effective shear modulus in the x_2x_3 plane with $\mu_{23}^C = \mu_{31}^C$. Using Eqs.(4.36) and (4.13), we obtain

$$\frac{\mu_{23}^C}{\mu_M} = 1 + \frac{c}{\dfrac{\mu_M}{\mu_I - \mu_M} + 2(1 - c)S_{2323}}. \qquad (4.45)$$

By the similar procedure, we obtain the effective shear modulus μ_{12}^C as

$$\frac{\mu_{12}^C}{\mu_M} = 1 + \frac{c}{\dfrac{\mu_M}{\mu_I - \mu_M} + 2(1 - c)S_{1212}}. \qquad (4.46)$$

4.4.3 Poisson's ratios

Effective Poisson's ratio ν_{31}^C is defined by

$$\nu_{31}^C = -\frac{\bar{\varepsilon}_{11}}{\bar{\varepsilon}_{33}},$$

where the first index refers to the coordinate of imposed stress or strain and the second index refers to the response direction. We apply the unidirectional stress along the x_3 axis and then the strain components in the comparison material are

$$\varepsilon_{11}^M = \varepsilon_{22}^M = -\nu_M \varepsilon_{33}^M.$$

Equations (4.32) and (4.34) reduce, respectively, to

$$\varepsilon_{11}^* = \frac{1}{A_1} \left(-\nu_M A_2 + A_4\right) \varepsilon_{33}^M,$$

$$\varepsilon_{33}^* = \frac{1}{A_1} \left(-2\nu_M A_5 + A_6\right) \varepsilon_{33}^M.$$

Using Eq.(4.13), we fined

$$\nu_{31}^C = \nu_M - c\frac{\nu_M \left(-2\nu_M A_5 + A_6\right) + \left(-\nu_M A_2 + A_4\right)}{A_1 + c\left(-2\nu_M A_5 + A_6\right)}. \qquad (4.47)$$

Similarly, applying the unidirectional stress along the x_1 direction, we obtain Poisson's ratios as

$$\nu_{12}^C = \nu_M - c\frac{\left(1 - \nu_M^2\right)\left(A_2 + A_3 A_1\right) - 2\nu_M(1 + \nu_M)A_4}{2A_1 + c\left\{\left(A_2 - A_3 A_1\right) - \nu_M \left(A_2 + A_3 A_1 + 2A_4\right)\right\}}, \qquad (4.48)$$

$$\nu_{13}^C = \nu_M - c\frac{2A_5 + \nu_M \left\{\left(A_2 - A_3 A_1 - 2A_5 - 2A_6\right) - \nu_M \left(A_2 + A_3 A_1 + 2A_4\right)\right\}}{2A_1 + c\left\{\left(A_2 - A_3 A_1\right) - \nu_M \left(A_2 + A_3 A_1 + 2A_4\right)\right\}}. \qquad (4.49)$$

4.4.4 Plane-strain bulk modulus

We consider the plane strain state in the x_1x_2 plane for the composite as

$$\bar{\varepsilon}_{11} = \bar{\varepsilon}_{22} = \bar{\varepsilon}, \qquad \bar{\sigma}_{11} = \bar{\sigma}_{22} = \bar{\sigma}.$$

Then, Eqs.(4.2) and (4.3) reduce, respectively, to

$$\bar{\sigma} = 2K_{12}^C \bar{\varepsilon}, \qquad \bar{\sigma} = 2\bar{K}_M \varepsilon_{11}^M + \lambda_M \varepsilon_{33}^M,$$

where K_{12}^C is the effective plane-strain bulk modulus in the x_1x_2 plane and $\bar{K}_M = \lambda_M + \mu_M$ is the plane strain bulk modulus of the matrix. Since $\bar{\varepsilon}_{33} = (-2\nu_{31}^C \bar{\sigma} + \bar{\sigma}_{33})/E_{33}^C = 0$, we find

$$\bar{\sigma}_{33} = 2\nu_{31}^C \bar{\sigma}.$$

Using this equation, the strain components of the comparison material are

$$\varepsilon_{11}^M = \varepsilon_{22}^M = \frac{1}{E_M}\left\{1 - \nu_M\left(1 + 2\nu_{31}^C\right)\right\}\bar{\sigma},$$

$$\varepsilon_{33}^M = \frac{2}{E_M}\left(\nu_{31}^C - \nu_M\right)\bar{\sigma}.$$

From Eqs.(4.32) and (4.13), we obtain

$$\frac{K_{12}^C}{\bar{K}_M} = \frac{(1 + \nu_M)(1 - 2\nu_M)}{1 - \nu_M(1 + 2\nu_{31}^C) + c\left[\{1 - \nu_M(1 + 2\nu_{31}^C)\} A_2 + 2(\nu_{31}^C - \nu_M)A_4\right]/A_1}. \tag{4.50}$$

Finally, substituting Eq.(4.47) into Eq.(4.50), the explicit form of K_{12}^C is obtained.

4.4.5 Numerical results and discussions

Figure 4.3 shows a comparison of two models for the effective moduli of a spheroidal-void/copper composite as a function of porosity c. A constant aspect ratio $\alpha = 0.5$ is supposed. The material properties used in the computation are the same as Fig. 4.2: $K_M = 137$ GPa, $\mu_M = 46.5$ GPa, $K_I = \mu_I = 0$. The results by Tandon-Weng [18] are based on Eqs.(4.43)-(4.46) and Eq.(4.50). The curves by Russel-Acrivos [8] are calculated based on their solutions assuming a dilute suspension. Tandon-Weng's curves pass through 1 at $c = 0$ and 0 at $c = 1$, while Russel-Acrivos's curves give linear dependence on c. They become closer to each other for a dilute suspension.

Figure 4.4 shows the variation of the effective moduli as a function of aspect ratio α. The material properties used in the computation are the same as Fig. 4.3. E_{33}^C is most sensitive to
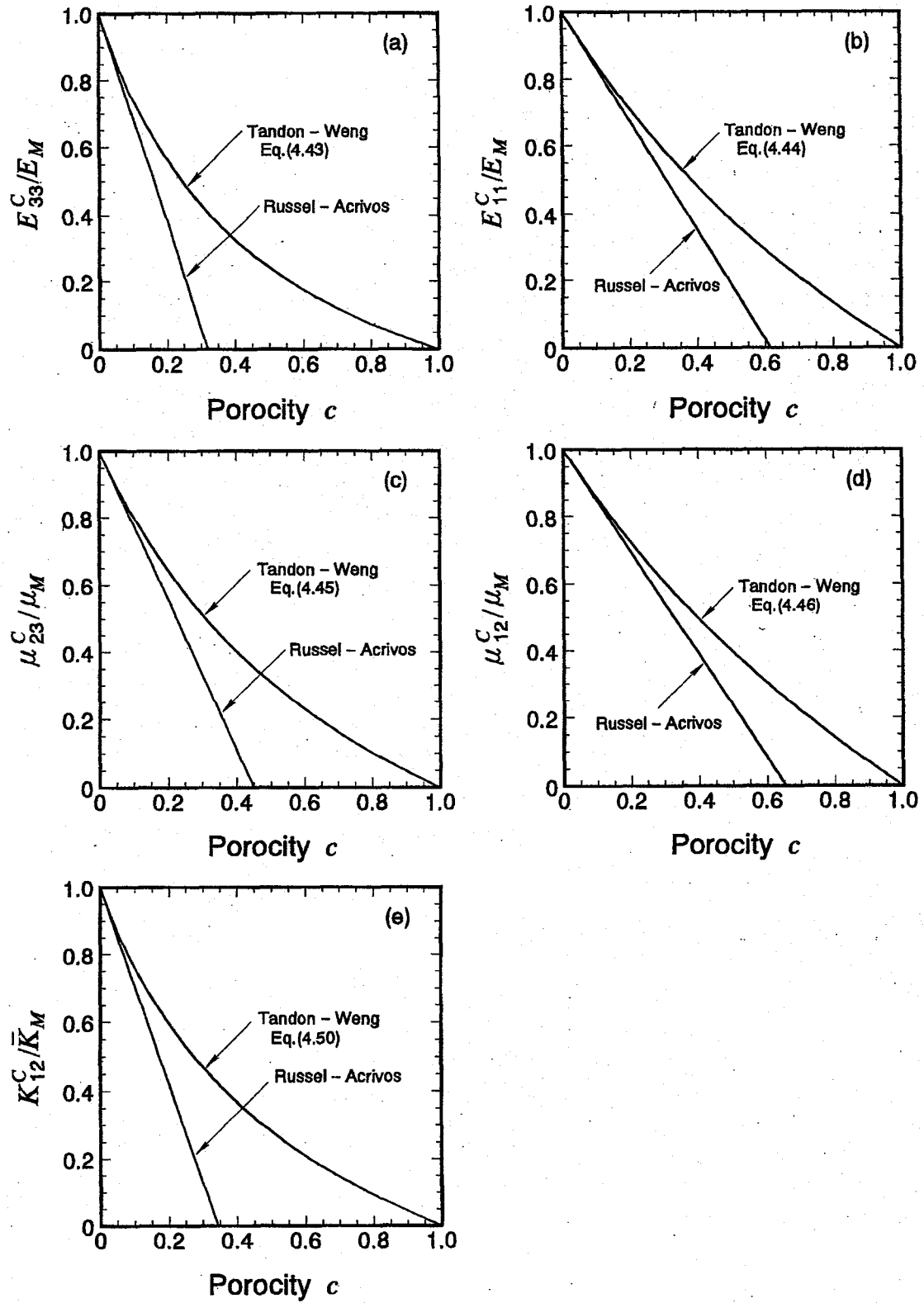
Fig. 4.3. Comparison of effective moduli for a spheroidal-void/copper composite by Tandon-Wng [18] and Russel-Acrivos [8]. Aspect ratio is $\alpha = 0.5$. The composite is transversely isotropic in the $x_1 x_2$ plane.
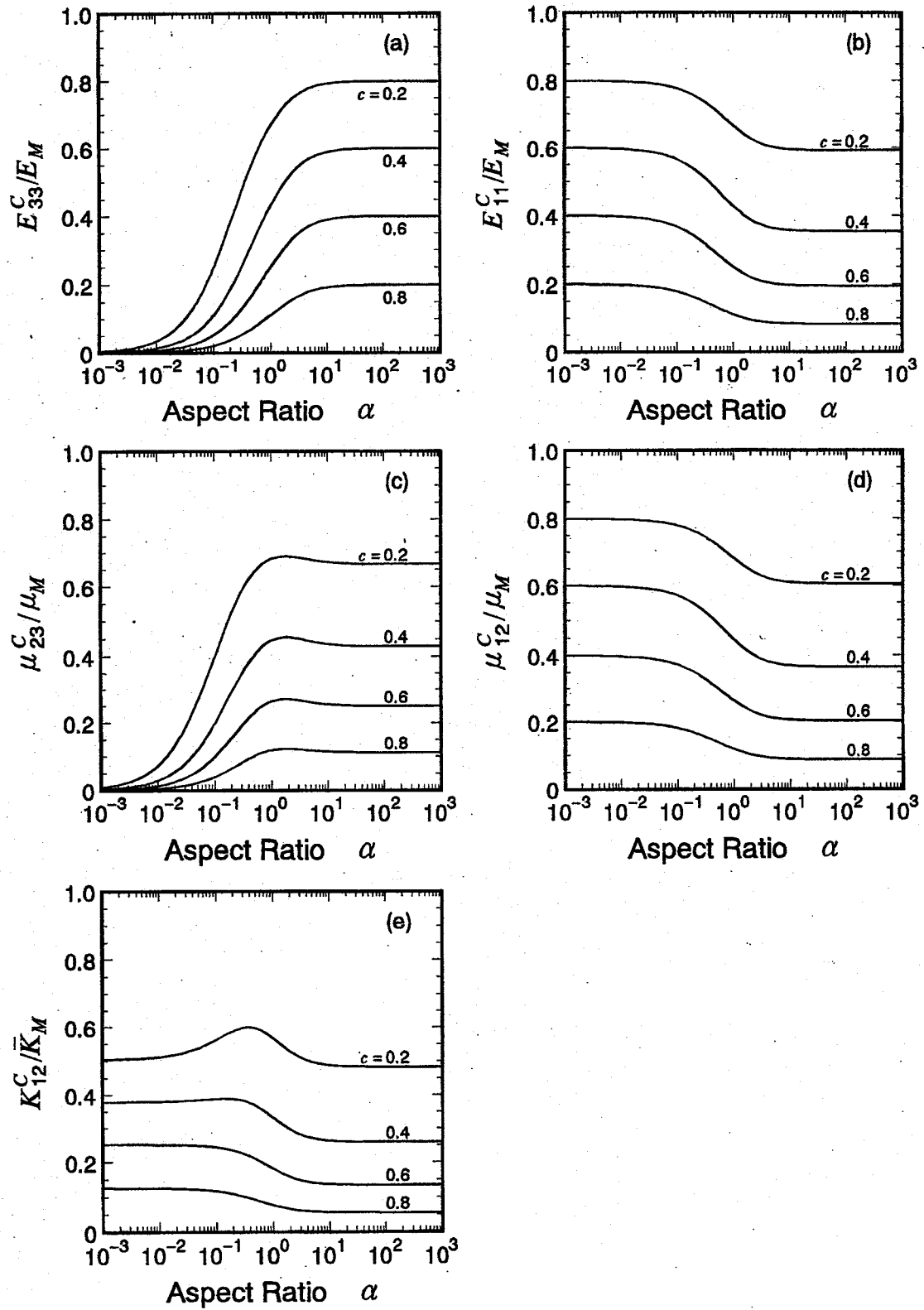
Fig. 4.4. Dependence of aspect ratio on effective moduli of spheroidal-void/copper composite. The composite is transversely isotropic in the $x_1 x_2$ plane.

the variation of α. E_{33}^C increases with increasing aspect ratio, while E_{11}^C and μ_{12}^C decrease with it. μ_{23}^C has a maximum value around $\alpha = 2$. K_{12}^C has also a maximum value for smaller c, but it shows a monotonous decrease for lager c. These five effective moduli reach the convergence at $\alpha = 100$ with increasing α. On the other hand, E_{11}^C, μ_{12}^C, and K_{12}^C reach the convergence at $\alpha = 0.01$ with decreasing α. E_{33}^C and μ_{23}^C converge to zero with decreasing α.

4.4.6 Relation between stiffness and engineering constants

In the end of this section, the engineering constants of a transverse isotropic composite described above are related to the effective elastic stiffness. The relations will be useful for a partially oriented composite in the next section and for creep damage modeling in the next chapter.

Stress-strain relation in a transverse isotropic composite is written as

$$
\begin{pmatrix} \sigma_{11} \\ \sigma_{22} \\ \sigma_{33} \\ \tau_{23} \\ \tau_{31} \\ \tau_{12} \end{pmatrix} = \begin{pmatrix} C_{11}^C & C_{12}^C & C_{13}^C & 0 & 0 & 0 \\ & C_{11}^C & C_{13}^C & 0 & 0 & 0 \\ & & C_{33}^C & 0 & 0 & 0 \\ & & & C_{44}^C & 0 & 0 \\ & sym. & & & C_{44}^C & 0 \\ & & & & & \frac{1}{2}\left(C_{11}^C - C_{12}^C\right) \end{pmatrix} \begin{pmatrix} \varepsilon_{11} \\ \varepsilon_{22} \\ \varepsilon_{33} \\ \gamma_{23} \\ \gamma_{31} \\ \gamma_{12} \end{pmatrix}. \tag{4.51}
$$

Consider a unidirectional stress state in the x_3 direction. From Eq.(4.51), E_{33}^C and ν_{31}^C are obtained as

$$
E_{33}^C = C_{33}^C - \frac{2(C_{13}^C)^2}{C_{11}^C + C_{12}^C}, \tag{4.52}
$$

$$
\nu_{31}^C = \nu_{32}^C = \frac{C_{13}^C}{C_{11}^C + C_{12}^C}. \tag{4.53}
$$

Next, we consider a plane strain state in the $x_1 x_2$ plane. From Eq.(4.51), we obtain

$$
K_{12}^C = \frac{1}{2}\left(C_{11}^C + C_{12}^C\right). \tag{4.54}
$$

From Eq.(4.51), shearing moduli are apparently

$$
\mu_{23}^C = \mu_{31}^C = C_{44}^C, \tag{4.55}
$$

$$
\mu_{12}^C = \frac{1}{2}\left(C_{11}^C - C_{12}^C\right). \tag{4.56}
$$

46

The inverse relations of Eqs.(4.52)-(4.56) are as follows;

$$C_{11}^C = K_{12}^C + \mu_{12}^C,$$

$$C_{12}^C = K_{12}^C - \mu_{12}^C,$$

$$C_{13}^C = 2K_{12}^C \nu_{31}^C, \tag{4.57}$$

$$C_{33}^C = E_{33}^C + 4K_{12}^C (\nu_{31}^C)^2,$$

$$C_{44}^C = \mu_{31}^C.$$

The transverse isotropic materials have five independent engineering elastic constants. The other engineering constants are related to them. Considering a unidirectional stress state in the x_1 direction, E_{11}^C, ν_{12}^C, and ν_{13}^C are obtained as

$$E_{11}^C = C_{11}^C + \frac{C_{12}^C \left\{ (C_{13}^C)^2 - C_{12}^C C_{33}^C \right\} + (C_{13}^C)^2 \left(C_{12}^C - C_{11}^C \right)}{C_{11}^C C_{33}^C - (C_{13}^C)^2}, \tag{4.58}$$

$$\nu_{12}^C = \frac{C_{12}^C C_{33}^C - (C_{13}^C)^2}{C_{11}^C C_{33}^C - (C_{13}^C)^2}, \tag{4.59}$$

$$\nu_{13}^C = \frac{C_{13}^C \left(C_{11}^C - C_{12}^C \right)}{C_{11}^C C_{33}^C - (C_{13}^C)^2}. \tag{4.60}$$

From the symmetry property, they are evidently,

$$\nu_{12}^C = \nu_{21}^C, \qquad \nu_{13}^C = \nu_{23}^C. \tag{4.61}$$

ν_{13}^C is not equal to ν_{31}^C, and the relation

$$\frac{\nu_{13}^C}{E_{11}^C} = \frac{\nu_{31}^C}{E_{33}^C} \tag{4.62}$$

holds. Substituting Eq.(4.57) into Eqs.(4.58) - (4.60), we obtain

$$E_{11}^C = \frac{4K_{12}^C \mu_{12}^C}{K_{12}^C + \mu_{12}^C + 4K_{12}^C \mu_{12}^C (\nu_{31}^C)^2 / E_{33}^C}, \tag{4.63}$$

$$\nu_{12}^C = \frac{K_{12}^C - \mu_{12}^C - 4K_{12}^C \mu_{12}^C (\nu_{31}^C)^2 / E_{33}^C}{K_{12}^C + \mu_{12}^C + 4K_{12}^C \mu_{12}^C (\nu_{31}^C)^2 / E_{33}^C}, \tag{4.64}$$

$$\nu_{13}^C = \frac{4K_{12}^C \mu_{12}^C \nu_{31}^C}{E_{33}^C \left(K_{12}^C + \mu_{12}^C \right) + 4K_{12}^C \mu_{12}^C (\nu_{31}^C)^2}. \tag{4.65}$$

4.5 Case C —Partially oriented spheroidal inclusions—

We consider a particle dispersed composite that has partially oriented spheroidal inclusions. The probability density for the orientation of spheroid is given by the orientation distribution function, ODF, described in chapter 3. Originally, the ODF was used to study the textured polycrystalline aggregate. It was also found useful to study the composites, such as rocks containing microcracks [45] and short-fiber composite [46, 47]. Their successes encourage us to apply the ODF to creep void modeling. The Voigt average was used in these previous studies, but we will adopt the Hill average to calculate the effective moduli for better result.

We suppose that the orientation distribution of spheroid is statistically of the orthorhombic symmetry. The coordinate system $O - X_1 X_2 X_3$ shown in Fig.3.1 represents the inclusion-fixed axes in this case, where the X_3 axis is taken along the symmetry axis of a spheroidal inclusion. We denote the inclusion-ODCs of the inclusion-ODF by W_{lmn}^I. Since the shape of inclusions is axial symmetric around the X_3 axis, the ODF $w(\xi, \psi, \phi)$ must be independent of ϕ. Therefore we take $n = 0$ in Eq.(3.4). Considering the symmetry properties of the inclusions and that of the sample with the orthorhombic symmetry, the ODCs W_{lm0}^I have the following characteristics:

(a) W_{lm0}^I are real values,

(b) W_{lm0}^I are zero unless l and m are even,

(c) $W_{lm0}^I = W_{l\bar{m}0}^I$.

Therefore, the ODF contains five independent ODCs, W_{200}^I, W_{220}^I, W_{400}^I, W_{420}^I, and W_{440}^I up to $l = 4$. It is written explicitly as

$$w(\xi, \psi, \phi) = \frac{1}{8\pi^2} + \frac{\sqrt{5}}{2\sqrt{2}} W_{200}^I \left(3\xi^2 - 1\right) + \frac{\sqrt{15}}{2} W_{220}^I \left(-\xi^2 + 1\right) \cos 2\psi$$

$$+ \frac{3}{8\sqrt{2}} W_{400}^I \left(35\xi^4 - 30\xi^2 + 3\right) \tag{4.66}$$

$$+ \frac{15}{4\sqrt{5}} W_{420}^I \left(-7\xi^4 + 8\xi^2 - 1\right) \cos 2\psi$$

$$+ \frac{3\sqrt{35}}{8} W_{440}^I \left(\xi^4 - 2\xi^2 + 1\right) \cos 4\psi,$$

where $\xi = \cos\theta$. The ODCs W_{2m0}^I $(m = 0, 2)$ determine the two-fold distribution intensity characterized by the second order functions of ξ. W_{4m0}^I $(m = 0, 2, 4)$ correspond to the four-fold distribution characterized by the fourth order functions of ξ. The truncated higher order ODCs, corresponding to the higher order functions of ξ, have no effect on the effective moduli.

We recast the effective elastic stiffness tensor for perfectly aligned spheroidal inclusions

48

obtained in previous section as C^A_{ijkl}. The stiffness tensor C^A_{ijkl} has five independent components. They are $C^A_{11} = C^A_{22}$, C^A_{33}, $C^A_{12} = C^A_{21}$, $C^A_{23} = C^A_{32} = C^A_{31} = C^A_{13}$, $C^A_{44} = C^A_{55}$, and $C^A_{66} = \left(C^A_{11} - C^A_{12}\right)/2$ in the Voigt (two-index) notation; all others are zero. They are given as functions of c, α, and the elastic constants of the matrix and the inclusions. We further denote the corresponding effective compliance tensor by S^A_{ijkl}. It has the same symmetry property with C^A_{ijkl}, except for $S^A_{66} = 2\left(S^A_{11} - S^A_{12}\right)$. Similar to Eqs.(3.15) and (3.16), the effective elastic moduli of the composite having the partially oriented spheroidal inclusions are obtained by

$$\langle C^C_{ijkl}\rangle_V = \int_0^{2\pi}\int_0^{2\pi}\int_{-1}^1 \beta_{mi}\beta_{nj}\beta_{pk}\beta_{ql}C^A_{mnpq}w(\xi,\psi,\phi)d\xi d\psi d\phi, \qquad (4.67)$$

$$\langle S^C_{ijkl}\rangle_R = \int_0^{2\pi}\int_0^{2\pi}\int_{-1}^1 \beta_{mi}\beta_{nj}\beta_{pk}\beta_{ql}S^A_{mnpq}w(\xi,\psi,\phi)d\xi d\psi d\phi. \qquad (4.68)$$

Substituting Eq.(4.66) into Eq.(4.67), the effective elastic stiffness in the Voigt average $\langle C^C_{ijkl}\rangle_V$ is obtained. Similarly, from Eq.(4.68), the effective elastic compliance in the Reuss average $\langle S^C_{ijkl}\rangle_R$ is obtained. Both of them again reduce to the sum of the isotropic and anisotropic parts. The effective elastic stiffness in the Reuss average $\langle C^C_{ijkl}\rangle_R$ is calculated by Eq.(3.13). Since the anisotropic part in $\langle S^C_{ijkl}\rangle_R$ is much smaller relative to the isotropic part, $\langle C^C_{ijkl}\rangle_R$ is also written as the sum of isotropic and anisotropic parts. Finally, we adopt the Hill average. The effective elastic stiffness for a particle dispersed composite with partial orientation distribution is represented as follows:

$$C^C_{11} = \lambda_C + 2\mu_C + \frac{8\sqrt{10}}{105}\pi^2 a_3\left(W^I_{200} - \sqrt{6}W^I_{220}\right)$$
$$+ \frac{4\sqrt{2}}{35}\pi^2 a_1\left(W^I_{400} - \frac{2\sqrt{10}}{3}W^I_{420} + \frac{\sqrt{70}}{3}W^I_{440}\right),$$

$$C^C_{22} = \lambda_C + 2\mu_C + \frac{8\sqrt{10}}{105}\pi^2 a_3\left(W^I_{200} + \sqrt{6}W^I_{220}\right)$$
$$+ \frac{4\sqrt{2}}{35}\pi^2 a_1\left(W^I_{400} + \frac{2\sqrt{10}}{3}W^I_{420} + \frac{\sqrt{70}}{3}W^I_{440}\right),$$

$$C^C_{33} = \lambda_C + 2\mu_C - \frac{16\sqrt{10}}{105}\pi^2 a_3 W^I_{200} + \frac{32\sqrt{2}}{105}\pi^2 a_1 W^I_{400},$$

$$C^C_{44} = \mu_C - \frac{2\sqrt{10}}{315}\pi^2\left(7a_2 + 2a_3\right)\left(W^I_{200} - \sqrt{6}W^I_{220}\right)$$

$$-\frac{16\sqrt{2}}{105}\pi^2 a_1 \left(W_{400}^I + \sqrt{\frac{5}{2}}W_{420}^I\right),$$

$$C_{55}^C = \mu_C - \frac{2\sqrt{10}}{315}\pi^2 (7a_2 + 2a_3)\left(W_{200}^I + \sqrt{6}W_{220}^I\right)$$

$$-\frac{16\sqrt{2}}{105}\pi^2 a_1 \left(W_{400}^I - \sqrt{\frac{5}{2}}W_{420}^I\right), \qquad (4.69)$$

$$C_{66}^C = \mu_C + \frac{4\sqrt{10}}{315}\pi^2 (7a_2 + 2a_3) W_{200}^I + \frac{4\sqrt{2}}{105}\pi^2 a_1 \left(W_{400}^I - \sqrt{70}W_{440}^I\right),$$

$$C_{23}^C = \lambda_C + \frac{4\sqrt{10}}{315}\pi^2 (7a_2 - a_3)\left(W_{200}^I - \sqrt{6}W_{220}^I\right)$$

$$-\frac{16\sqrt{2}}{105}\pi^2 a_1 \left(W_{400}^I + \sqrt{\frac{5}{2}}W_{420}^I\right),$$

$$C_{31}^C = \lambda_C + \frac{4\sqrt{10}}{315}\pi^2 (7a_2 - a_3)\left(W_{200}^I + \sqrt{6}W_{220}^I\right)$$

$$-\frac{16\sqrt{2}}{105}\pi^2 a_1 \left(W_{400}^I - \sqrt{\frac{5}{2}}W_{420}^I\right),$$

$$C_{12}^C = \lambda_C - \frac{8\sqrt{10}}{315}\pi^2 (7a_2 - a_3) W_{200}^I + \frac{4\sqrt{2}}{105}\pi^2 a_1 \left(W_{400}^I - \sqrt{70}W_{440}^I\right),$$

where λ_C and μ_C are the Lamé constants for an isotropic composite and a_j $(j = 1, 2, 3)$ is the anisotropy factor. They are defined by

$$\lambda_C = \lambda_H = \frac{\lambda_V + \lambda_R}{2},$$

$$\mu_C = \mu_H = \frac{\mu_V + \mu_R}{2},$$

$$a_1 = a_{1H} = \frac{a_{1V} + a_{1R}}{2},$$

$$a_2 = a_{2H} = \frac{a_{2V} + a_{2R}}{2},$$

$$a_3 = a_{3H} = \frac{a_{3V} + a_{3R}}{2},$$

$$\lambda_V = \frac{1}{15}\left(C_{11}^A + C_{33}^A + 5C_{12}^A + 8C_{31}^A - 4C_{44}^A\right),$$

$$\mu_V = \frac{1}{30}\left(7C_{11}^A + 2C_{33}^A - 5C_{12}^A - 4C_{31}^A + 12C_{44}^A\right),$$

$$a_{1V} = C_{11}^A + C_{33}^A - 2C_{31}^A - 4C_{44}^A,$$

$$a_{2V} = C_{11}^A - 3C_{12}^A + 2C_{31}^A - 2C_{44}^A,$$

$$a_{3V} = 4C_{11}^A - 3C_{33}^A - C_{31}^A - 2C_{44}^A,$$

$$\lambda_R = -\frac{S_{R2}}{(S_{R1} - S_{R2})(S_{R1} + 2S_{R2})}, \tag{4.70}$$

$$\mu_R = \frac{1}{2(S_{R1} - S_{R2})},$$

$$a_{1R} = -4\mu_R^2 S_{R3},$$

$$a_{2R} = 2\lambda_R\mu_R \left\{ \frac{S_{R1}S_{R4}}{S_{R2}} + \frac{2}{3}(2S_{R4} + S_{R5}) \right\},$$

$$a_{3R} = 2\lambda_R\mu_R \left\{ \frac{S_{R1}S_{R5}}{S_{R2}} + \frac{1}{3}(7S_{R4} - S_{R5}) \right\},$$

$$S_{R1} = \frac{1}{15}(8S_{11}^A + 3S_{33}^A + 4S_{31}^A + 2S_{44}^A),$$

$$S_{R2} = \frac{1}{15}(S_{11}^A + S_{33}^A + 5S_{12}^A + 8S_{31}^A - S_{44}^A),$$

$$S_{R3} = S_{11}^A + S_{33}^A - 2S_{31}^A - S_{44}^A,$$

$$S_{R4} = S_{11}^A - 3S_{12}^A + 2S_{31}^A - \frac{1}{2}S_{44}^A,$$

$$S_{R5} = 4S_{11}^A - 3S_{33}^A - S_{31}^A - \frac{1}{2}S_{44}^A.$$

Note that in the case of an axial symmetric distribution of inclusions along x_3, $W_{220}^I = W_{420}^I = W_{440}^I = 0$ and the effective elastic stiffness are determined by only two expansion coefficients W_{200}^I and W_{400}^I. In this case the composite is transversely isotropic in the x_1x_2 plane. In the case of a random orientation, five ODCs are all zeros, and the composite is isotropic.

A numerical example is given in Fig. 4.5 to compare the averaging procedures with each other. The material properties used in this calculation are the same with Figs. 4.2 - 4.4; a void/copper composite. A constant aspect ratio $\alpha = 0.1$ is supposed. The figure shows the large relative differences depending on the averaging procedures especially in a_{1i} ($i = V, R, H$). But the differences for the dilute suspension are negligible except for a_{1i}. The values of a_{1i} and a_{2i} have one order smaller values than a_{3i}. The degree of the differences in these five parameters depends on the degree of the anisotropy in C_{ijkl}^A. The anisotropy in C_{ijkl}^A was shown implicitly in Figs. 4.3 - 4.4. Despite such a large difference in a_{1i} only the Voigt average had been used to apply the ODF to the partial oriented composites in the existing work [45] - [47].
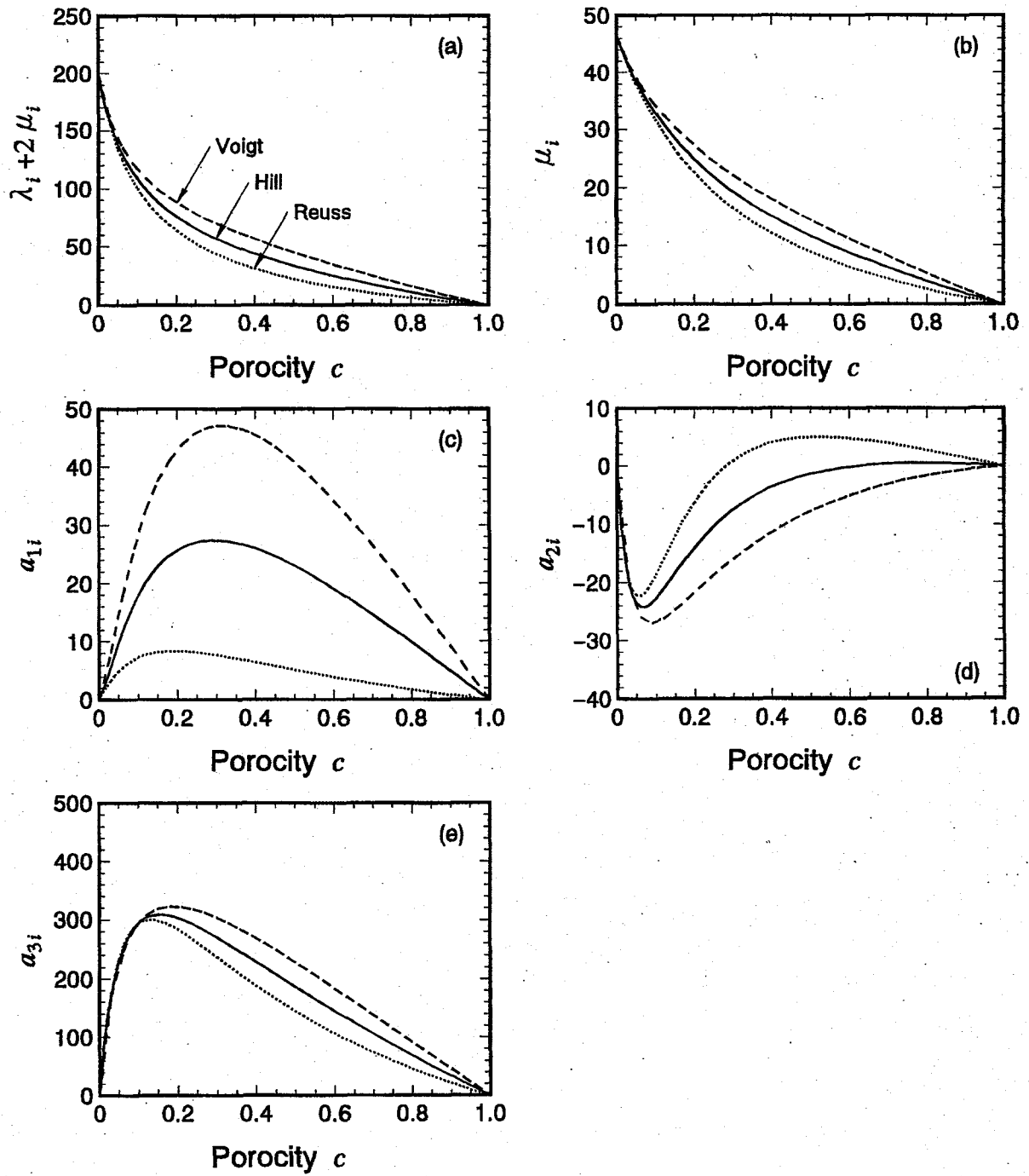
Fig. 4.5. Comparison among averaging procedures. Constant aspect ratio $\alpha = 0.1$ is supposed. Unit in parameters is GPa.

4.6 Summary

The effective elastic moduli of a particle dispersed composite were derived for three cases. They will be applied to establish the creep void modeling in chapter 5. The experimental result of the porosity shows $c \leq 0.02$. It seems that the calculation of effective elastic moduli for a dilute suspension is sufficient for creep void modeling. However, we adopted a full range theory to make a model (model 5) having a positional distribution of voids. In the model, the spherical voids are restricted to within the volume elements dispersed in the matrix. The overall porosity is $c \leq 0.02$, but the void volume fraction in the elements can have a large value.

It is assumed that the matrix and the inclusion materials are both linearly elastic, isotropic, and homogeneous. The inclusions are assumed to be randomly positioned in the matrix. Three cases are summarized as follows:

Case A. The spherical inclusions are assumed. The composite is isotropic. The effective stiffness of the composite C_{ijkl}^{C} depends only on the volume fraction c, provided the elastic constants of the constituents are given.

Case B. The shape of inclusions is assumed to be spheroidal. The symmetry axes are unidirectionally aligned along the x_3 direction. The shape of inclusions is given by the aspect ratio α. The effective stiffness C_{ijkl}^{C} is transversely isotropic in the $x_1 x_2$ plane. It is obtained as functions of c and α.

Case C. We applied the ODF to a composite with partially oriented spheroidal inclusions. The statistical distribution of the orientation is assumed to be orthorhombic. The effective stiffness is modified from that of the case B (recasting as C_{ijkl}^{A}) using the inclusion-ODF as a weighting function. We use the Hill average to obtain the better results. C_{ijkl}^{C} again reduces to the sum of isotropic and anisotropic parts. The isotropic constants λ_C and μ_C, and the anisotropy factors a_j ($j = 1, 2, 3$) depend on c and α. The anisotropic parts are given by the products of a_j and the five independent inclusion-ODCs, W_{200}^{I}, W_{220}^{I}, W_{400}^{I}, W_{420}^{I}, and W_{440}^{I}. For the axis-symmetrical distribution, C_{ijkl}^{C} is obtained by setting $W_{220}^{I} = W_{420}^{I} = W_{440}^{I} = 0$. Substituting zero to the five ODCs, the expression of C_{ijkl}^{C} reduces to that of random orientation.

Chapter 5

CREEP VOIDS MODELING AND NUMERICAL CALCULATIONS

5.1 Introduction

In this chapter, we intend to establish a creep voids model that explains the ultrasonic velocity change described in chapter 2. According to the conclusion in chapter 3, the normalized velocities exclude the texture effect:

$$\frac{V_i^*}{V_i^R} = \sqrt{\frac{1}{1-c}\frac{C_i^C}{C_i^M}}, \tag{5.1}$$

where $C_{ijkl}^C = C_{ijkl}^M + \Delta C_{ijkl}^V$ is the effective stiffness of the composite made up with isotropic copper matrix and voids. The values of the stiffness in the matrix C_{ijkl}^M have already been obtained in Eq.(3.28). The elastic constants of voids are $K_I = \mu_I = 0$. The void effect ΔC_{ijkl}^V depends on the void factors; the volume fraction (the porosity), the shape (the aspect ratio), the positional distribution, and the orientation distribution of non-spherical voids. Porosity is obtained by the measured density, but the remaining three factors have to be determined to establish the models. Five candidate models are considered. Among them, we seek the most acceptable model, which best explains the quantitative relation between the measured velocities and the porosity, and represents well the damaging process.

5.2 Model 1 —Spherical voids model—

Spherical voids randomly positioned in the copper matrix are assumed. The model coincides with case A in the previous chapter. The effective stiffness C_{ijkl}^C is macroscopically isotropic. It is obtained by Eq.(4.20) and Eq.(4.22) as a function of the porosity c. Comparison of the measured normalized velocities with the calculations is shown in Fig. 5.1. The broken lines represent the calculations. When the porosity is sufficiently small, this is a good approximation to the measured velocities, indicating that the spherical voids nucleate at ran-
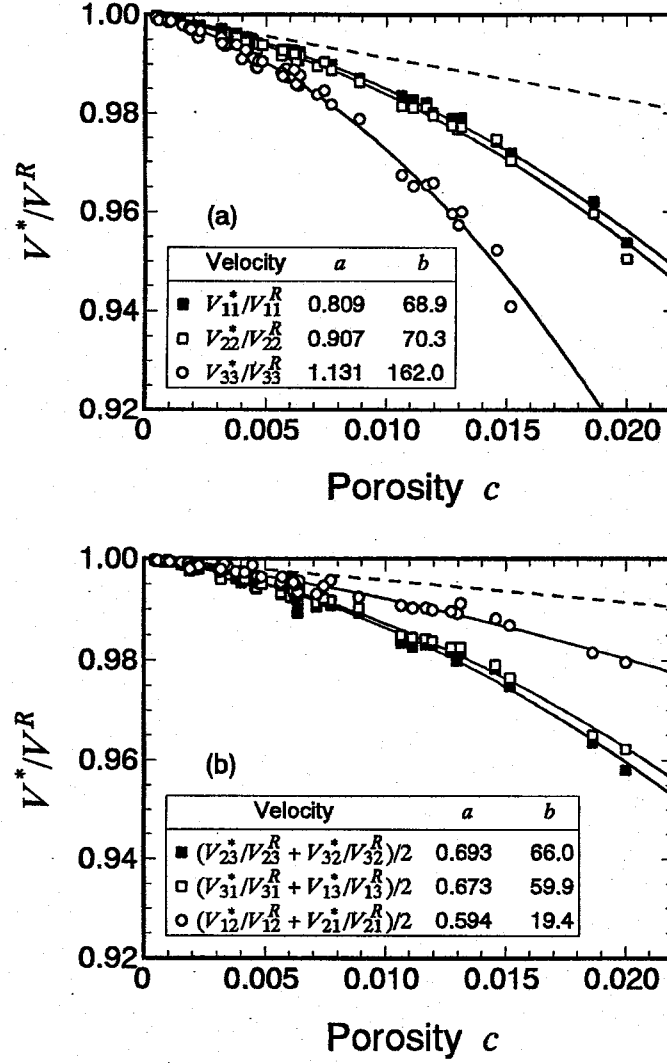
Fig. 5.1. Comparison of the measured normalized velocities with the calculations by the spherical voids model (model 1) for longitudinal waves (a) and shear waves (b).

dom locations. However, the measured velocities decrease more acceleratingly with increasing c than the calculation. Together with the isotropy, this model should be rejected except for $c \approx 0$.

5.3   Model 2 —Unidirectionally aligned oblate voids model—

We consider the unidirectional alignment of minor axis of the oblate voids (aspect ratio $\alpha < 1$) with random positions. In this composite, four independent velocities are $V_{11}^* = V_{22}^*$, V_{33}^*, $V_{23}^* = V_{32}^* = V_{31}^* = V_{13}^*$, and $V_{12}^* = V_{21}^*$. The model can potentially explain the velocity anisotropy. The effective stiffness C_{ijkl}^C is obtained from case B in section 4.4. It has two parameters, c and α.
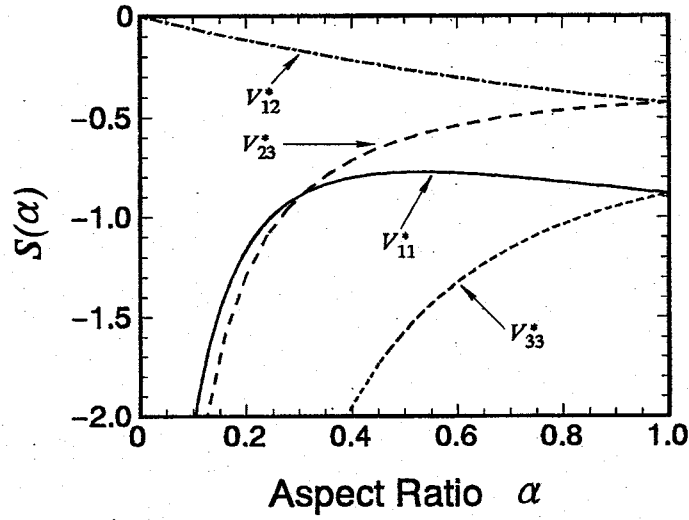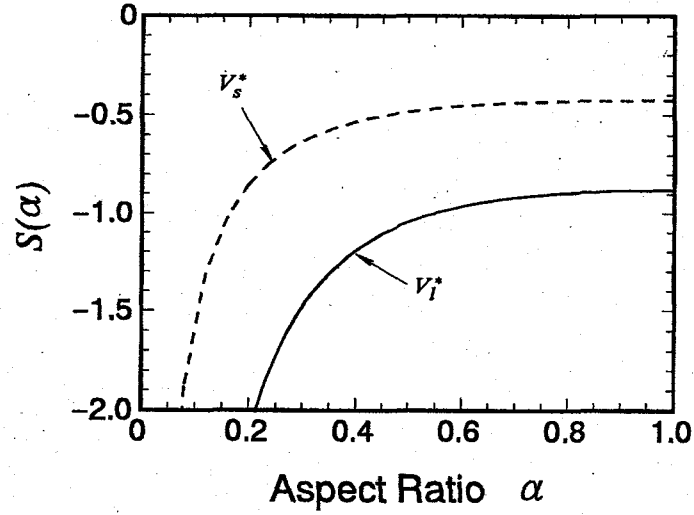
Fig. 5.2. Slope $S(\alpha)$ in normalized velocities as a function of aspect ratio α by the supposition of unidirectionally aligned oblate voids (model 2).

Measured porosity c is smaller than 0.02. For such a dilute suspension, the normalized velocities are approximated to

$$\frac{V^*}{V^R} = 1 + S(\alpha)c, \tag{5.2}$$

where $S(\alpha)$ is the slope of straight line as a function of α. In the case of spherical voids ($\alpha = 1$), the above equation (5.2) coincides with the result from Eq.(4.20) and Eq.(4.22), and is shown in Fig. 5.1. Figure 5.2 shows $S(\alpha)$ based on the present model. The figure shows $V_{33}^* < V_{11}^* < V_{23}^* < V_{12}^*$ for the possible range of α, which is compatible with the measured velocities (see Fig. 5.1). Supposing that the aspect ratio α decreases with increasing porosity c, the accelerated decrease of measured velocities V_{33}^* and V_{23}^* can be understood from the figure. According to the lines for V_{11}^* and V_{12}^*, the slope of the velocities should increase with decreasing α. However, the measured velocities showed the opposite tendency.

The unidirectional alignment explains the experimental features (3), (4) and (5) summarized in chapter 2, which are qualitative features of the velocity anisotropy. However, it explains only partly the feature (2) and is not acceptable.

5.4 Model 3 −Randomly oriented oblate voids model−

We next consider the random orientation of the oblate voids with random positions. The effective stiffness of the composite is then isotropic, and is given by Eq.(4.69), in which the

Fig. 5.3. Slope $S(\alpha)$ in normalized velocities as a function of aspect ratio α by the supposition of randomly oriented oblate voids (model 3).

all ODCs are set to zero. As in the unidirectional alignment, the normalized velocities are approximated to the form of Eq.(5.2) for dilute suspension. Figure 5.3 shows $S(\alpha)$, where V_l^* denotes the longitudinal wave velocity and V_s^* denotes the shear wave velocity. Both $S(\alpha)$ naturally take the average values of longitudinal and shear waves in Fig. 5.2 and decrease with decreasing α. Therefore, the random orientation compensates for the contradiction to the experimental features (2) in the unidirectional alignment, although it gives the macroscopic isotropy.

From the qualitative discussions of models 1 - 3, it is concluded that the orientation distribution should be partial.

5.5 Model 4 —Partially oriented oblate voids model—

We consider model 4 as illustrated in Fig. 5.4 in a two dimensional sketch. The oblate ellipsoidal voids are assumed to be randomly positioned in the matrix. A void is rotated by angle ψ around the x_3 axis and by θ around the X_2 axis. The symmetry axis of spheroidal void X_3 inclines in the direction of the angle ψ (See Fig. 3.1). The inclusion-ODF is given by Eq.(4.66). This model coincides with case C. The effective stiffness $C_{ijkl}^C = C_{ijkl}^M + \Delta C_{ijkl}^V$ is given by Eq.(4.69). The modeling parameters are the porosity c, the aspect ratio of voids α, and five ODCs.

It is natural to suppose that the orientation distribution is statistically axial symmetric around the x_3 axis. If the supposition is acceptable, the ODF is independent of ψ and
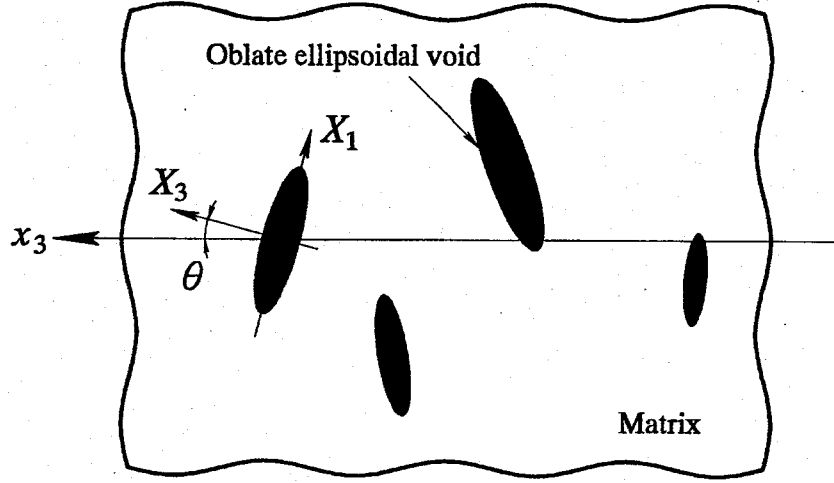
Fig. 5.4. Partially oriented oblate modeling (model 4).

$W_{220}^I = W_{420}^I = W_{440}^I = 0$. In the velocity measurements shown in Fig. 2.7, we observed $V_{11}^*/V_{11}^R \approx V_{22}^*/V_{22}^R$ and $V_{23}^*/V_{23}^R \approx V_{31}^*/V_{31}^R$. The equalities indicate only $W_{220}^I \approx 0$ and $W_{420}^I \approx 0$. It is unclear from the measurement whether W_{440}^I varnishes or not. We thus suppose the statistically orthorhombic symmetry with five unknown ODCs. The calculation results will show $W_{220}^I \approx 0$ and $W_{420}^I \approx 0$. If $W_{440}^I \approx 0$ is also achieved, the distribution will be concluded to be axial symmetric.

The porosity c has been obtained by the measurements. We need to determine the remaining parameters from the measured velocities; the aspect ratio α and five ODCs. We use an error function as

$$E = \sum_{i=1}^{6} (u_i^m - u_i^p)^2 , \qquad (5.3)$$

where $u_i^m = (V_i^*/V_i^R)^2$ are the measured values and $u_i^p = C_i^C / \left\{ (1-c)C_i^M \right\}$ are the predicted values from the given parameters. Finding the parameters to make E minimum is equivalent to solve the simultaneous equation, $\partial E/\partial \alpha = 0$ and $\partial E/\partial W_{lm0}^I = 0$. Because we have six parameters to six measured velocities, the perfect agreement between the measured and the calculated velocities, or $E = 0$, could be achieved. Unfortunately, the calculation for derivative $\partial E/\partial \alpha$ is very laborious in this case. We attempt to determine the parameters by a numerical iteration procedure without using $\partial E/\partial \alpha = 0$. The partial derivatives with respect to five ODCs $\partial E/\partial W_{lm0}^I$ are easily obtainable, because E is a quadratic function of the linear combination of W_{lm0}^I. Under a given α_k for the kth iteration, the numerical solution of the simultaneous equations for five ODCs are substituted into Eq.(5.3), and then E_k is calculated
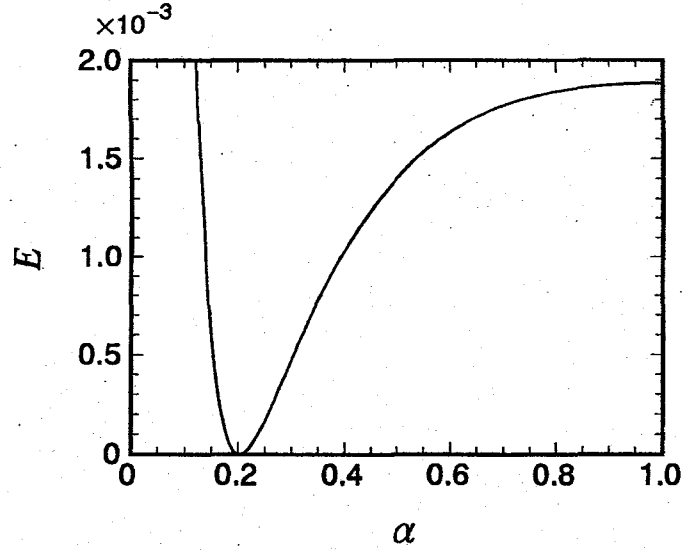
Fig. 5.5. Error function E as a function of aspect ratio α for model 4. Porosity c is assumed to be 0.01.

numerically. Next, E_{k+1} is calculated for $\alpha_{k+1} = \alpha_k + \Delta\alpha_k$. The corrector $\Delta\alpha_k$ is selected to be $E_{k+1} < E_k$ and to arrive at $E_{\min}$ as fast as possible. The iteration is continued until an absolute difference $|\Delta\alpha_k|$ becomes smaller than the sufficiently small value e: $|\Delta\alpha_k| < e$. The predicted α is then obtained as α_k. A typical example of E as a function of α is shown in Fig. 5.5. The porosity c is assumed to be 0.01 in this example. The function E has only a minimum of zero. In other words, $\partial E/\partial \alpha = 0$ has a unique solution. Because of this, we can determine α to give $E_{\min}$ by the iteration procedure with no ambiguity. We adopt the conjugate direction method [48] for the iteration procedure. It is one of the method for finding the most efficient corrector and gives the minimum only after several iterations.

We used $e = 10^{-5}$. The function E reached the minimum in the order of 10^{-12} for all damaged samples. The convergence was achieved by several iterations even in a far different initial value. Because the order of $E_{\min}$ is sufficiently small, we were able to determine the modeling parameters that make perfect agreement between the measured and the calculated normalized velocities. The agreement is shown in Fig. 5.6. It is the natural result because of the six parameters to the six velocities. However, the parameters have to be examined whether they represent the damage process suitably.

Numerical results for the modeling parameters are shown in Fig. 5.7. Solid lines represent the calculated results based on the fitting curves in Fig. 2.7. The fitting curve on V_{33}^* is extrapolated to compensate for the last two unavailable measurements. Aspect ratio α is around 0.5 in the early stage and decreases with increasing porosity c. This indicates the
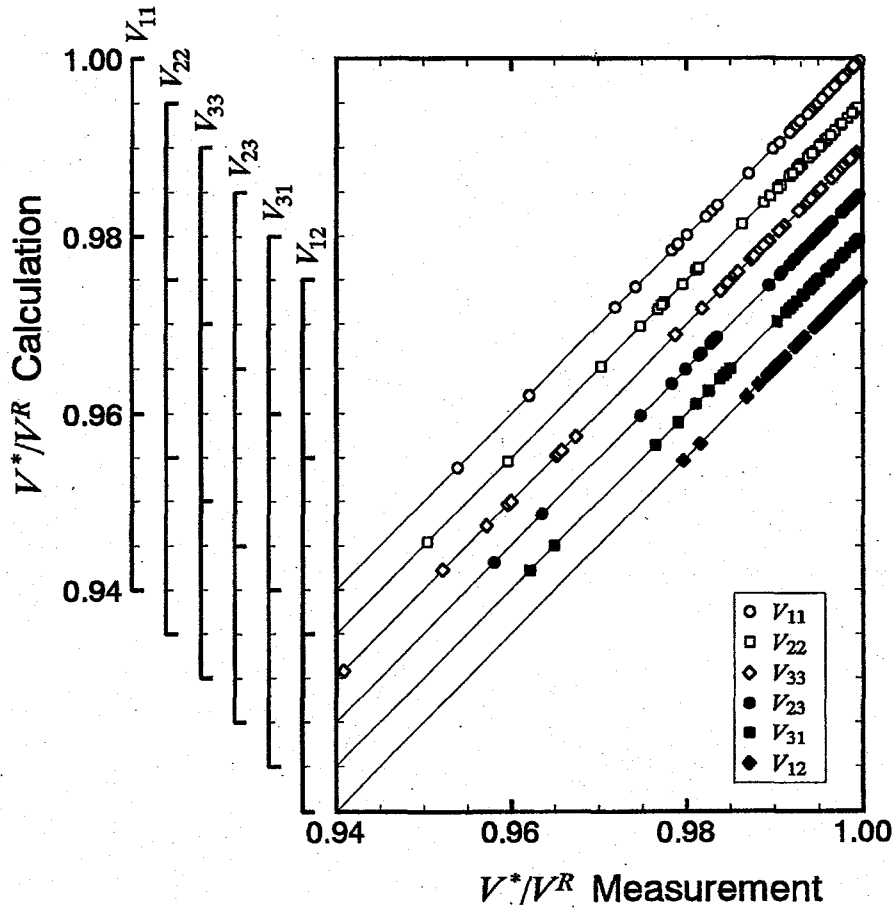
Fig. 5.6. Agreement between the measured and the calculated normalized velocities using model 4.

nucleation of oblate voids and the void growth to microcracks with the damage accumulation.

The ODCs for small c could be erroneous in some degree due to the behavior of the anisotropy factors a_j ($j = 1, 2, 3$). Figure 5.8 shows the anisotropy factors calculated from the measured porosity c and the estimated aspect ratio α. They approach zero when c diminishes. The calculation contains dividing with a_j and their very small values may cause a large scattering in the calculated ODCs.

As shown in Fig. 5.7, the calculated W_{220}^I and W_{420}^I are close to zero as is expected from the measured normalized velocities, $V_{11}^*/V_{11}^R \approx V_{22}^*/V_{22}^R$ and $V_{23}^*/V_{23}^R \approx V_{31}^*/V_{31}^R$. W_{440}^I, which is the remaining ODC to give the distribution on ψ (see Eq.(4.66) and Fig. 3.1), is not equal to zero. We expected $W_{440}^I = 0$ because of the unidirectional stress. The result indicates that the inclusion orientation distribution is not ideally axial symmetric, but it approaches the symmetry with the damage accumulation. The void nucleation doesn't take place axis-symmetrically on the grain boundaries (probably due to the texture-induced anisotropy of
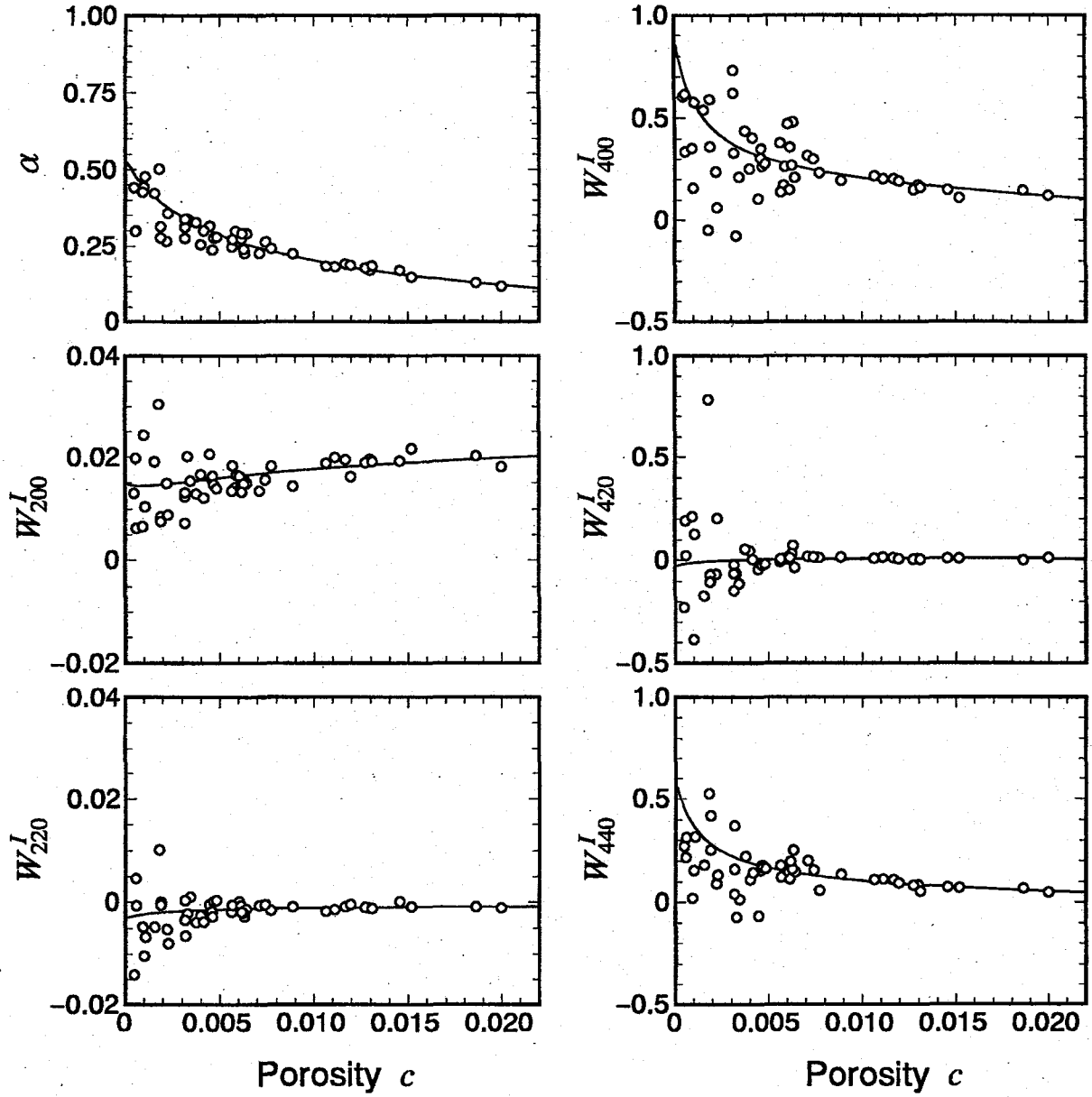
61

Fig. 5.7. Calculation results for model 4.

misorientation distribution). But the growth of voids occurs mainly in the axial symmetric way.

W_{200}^I and W_{400}^I determine the distribution intensity at $\theta = 0$, where θ is the rotation angle of the void symmetry axis X_3 from the stress direction x_3. W_{200}^I increases with the porosity, but W_{400}^I decreases. Because W_{4m0}^I is one order of magnitude larger than W_{2m0}^I, the ODF w is governed by W_{4m0}^I. Therefore, the distribution intensity at $\theta = 0$ decreases with the porosity. The inferred ODF w by Eq.(4.66) at two porosities is shown in Fig. 5.9. The inferred ODCs
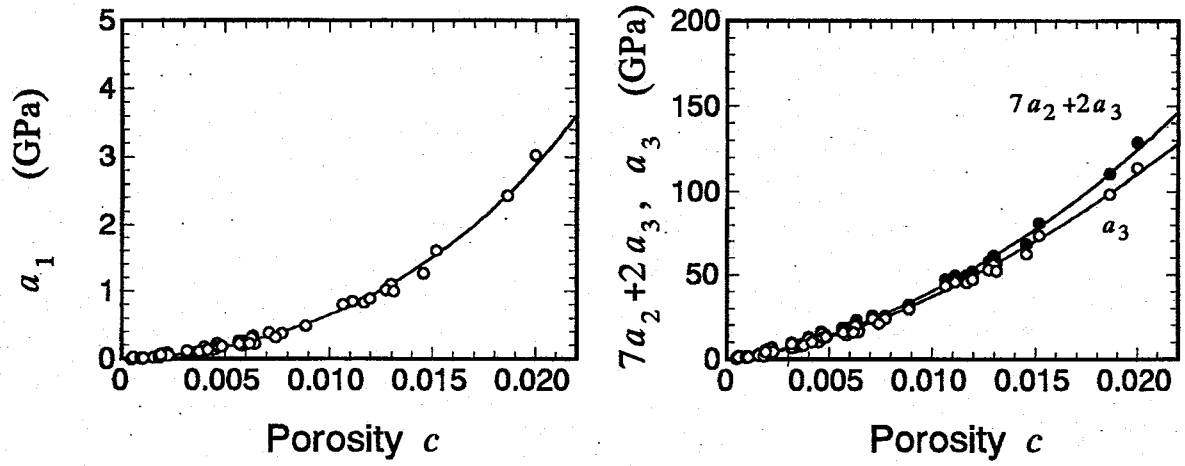
Fig. 5.8. Anisotropy factors for model 4.
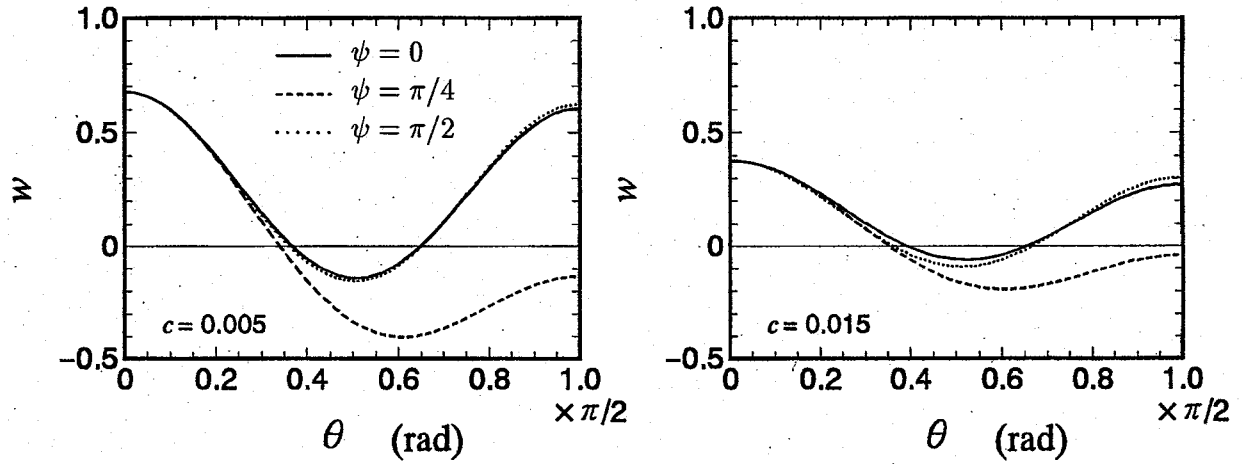
Fig. 5.9. ODF w for model 4 truncated at $l = 4$.

by fitting curves for measured velocities at $c = 0.005$ and $c = 0.015$ were substituted into the equation. Truncation at $l = 4$ has lost fine features of the orientation distribution, and is responsible for yielding unrealistic negative values of w. The figure shows the decreasing intensity at $\theta = 0$ with increasing c.

We summarize the modeling calculation results and point out a irrationality of model 4. We determined the modeling parameters to make the measured velocities coincide with the calculated velocities. The minimum E_{min} was sufficiently small. The model can explain the experimental features from (2) to (5) described in chapter 2. The changes in modeling parameters with increasing porosity c are summarized as follows:

(i) α decreases,   (ii) W_{200}^I increases,   (iii) W_{440}^I decreases,   (iv) W_{400}^I decreases.

The changes (i), (ii), and (iii) are acceptable for the damage accumulation model. However, the change (iv) is improper. We require the increasing W_{400}^I because of the damaging process, that is, the growth of voids within the grain boundaries perpendicular to the stress axis x_3. According to the observation of voids by photomicrograph (Fig.2.3), the voids are not randomly positioned. They tend to gather preferentially on the grain boundaries perpendicular to the x_3 direction. The irrationality would be caused by the simplification for void state.

5.6   Model 5 —Double composite model—

The damage morphology motivates us to consider a composite modeling relying on the non-random positions of spherical voids. The basic concept is illustrated in Fig.5.10 in a two dimensional sketch. The creep voids are assumed to be dispersed uniformly in oblate ellipsoidal volume elements. The volume elements are randomly positioned in the matrix, and their principal axes X_i are statistically tilted in an orthorhombic symmetric way. A volume element is rotated by angle ψ around the x_3 axis and by θ around the X_2 axis. By the ellipsoidal volume elements, we simulate the grain boundaries containing creep voids. The composite model having such a hierarchical structure has been used for studying the effective stiffness of SiC/Al-alloy composite by Ledbetter et al. [49].

The calculation procedure with this *double composite model* consists of three steps [50]. For the first step, the spherical voids are assumed to be distributed uniformly in the copper matrix. We calculate the effective stiffness of this composite C_{ijkl}^C using Eqs.(4.20) and (4.22).
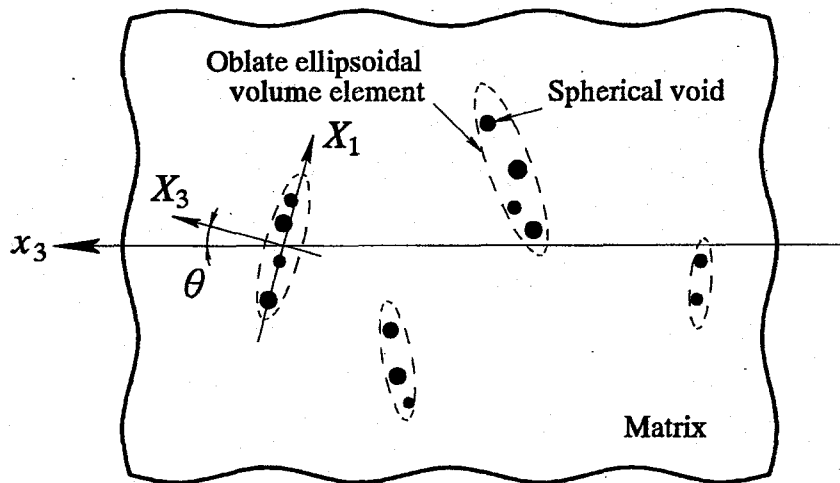

Fig. 5.10. Double composite modeling (model 5).

The density of this composite, ρ_1, is given by

$$\rho_1 = (1 - c_1)\rho_R, \tag{5.4}$$

where c_1 is the volume fraction of spherical voids and ρ_R is the density of the matrix, that is the reference sample.

In the second step, the volume elements including voids are regarded as the oblate ellipsoidal inclusions. They are distributed randomly in the copper matrix with the minor axes parallel to the stress direction x_3. The shape of the oblate ellipsoids is represented by an aspect ratio α (< 1). We obtain the anisotropic stiffness tensor for perfect alignment, C^A_{ijkl}, by the equations described in section 4.4. In this calculation, the stiffness C^C_{ijkl} obtained by the previous step is used as the stiffness of ellipsoidal inclusions C^I_{ijkl}. The volume fraction of the oblate ellipsoids is denoted by c_2. The density of the composite with the perfect alignment, ρ_2, is

$$\rho_2 = (1 - c_2)\rho_R + c_2\rho_1 = (1 - c_1 c_2)\rho_R, \tag{5.5}$$

where the density of ellipsoidal inclusion ρ_1 in Eq.(5.4) was used.

Finally, the oblate ellipsoids are inclined by angles θ and ψ and then C^A_{ijkl} is averaged with ODF w as a weighting function. The ODF w is given in Eq.(4.66). We obtain the effective stiffness of the double composite model as Eq.(4.69). The density of the composite ρ_* is equivalent to ρ_2 in the second step, Thus the density of the composite is given by

$$\rho_* = (1 - c_1 c_2)\rho_R. \tag{5.6}$$

The porosity c is determined by $c_1 c_2$.

The final effective stiffness C^C_{ijkl} is governed by eight modeling parameters, c_1, c_2, α, and five ODCs W^I_{lm0}. The anisotropy factors a_j ($j = 1, 2, 3$) and ODCs contribute to the stiffness anisotropy. The a_j reflect the anisotropy strength introduced by the arranged formation of spherical voids on the grain boundaries. The five ODCs W^I_{lm0} reflect the orientation distribution of the oblate ellipsoids containing the voids inside. When the ellipsoids are randomly oriented, W^I_{lm0} vanish and the stiffness is isotropic. The isotropic constants λ_C and μ_C are the functions of c_1, c_2, and α. They decrease with the void formation.

Equation (5.3) is considered again. Since the porosity c has been measured, we give the volume fraction of the oblate ellipsoids as $c_2 = c/c_1$. We have seven parameters, c_1, α, and five ODCs, against the six velocities. It is impossible to determine them from only the velocities. $W^I_{220} = W^I_{420} = 0$ could be assumed. However, it indicates $V^*_{11}/V^R_{11} = V^*_{22}/V^R_{22}$ and
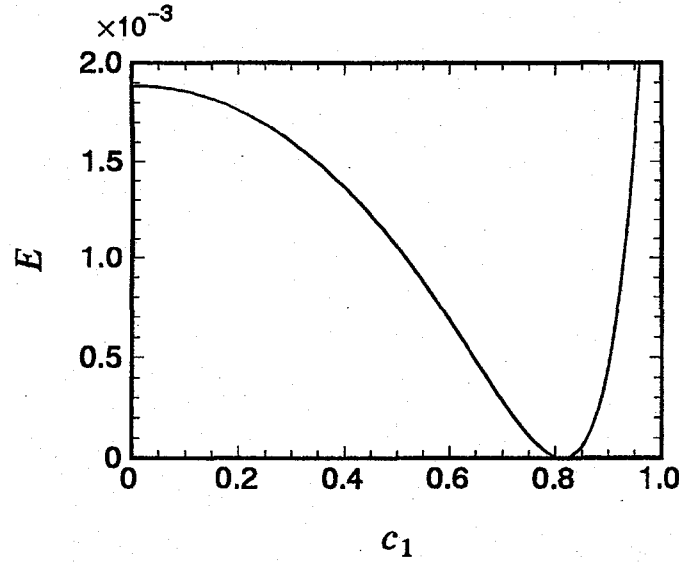
Fig. 5.11. Error function E as a function of c_1 for model 5. Porosity c and aspect ratio α are assumed as 0.01 and 0.1 respectively.

$V_{23}^*/V_{23}^R = V_{31}^*/V_{31}^R$. Therefore, this assumption is meaningless. For the sake of supplement, we impose a constant aspect ratio $\alpha = 0.1$. This is suggested by the average void diameter of 10 μm and the average grain size of 0.1 mm. The error function E can be calculated as a function of only c_1, by putting the solutions for the simultaneous equation $\partial E/\partial W_{lm0}^I = 0$ and the constant aspect ratio $\alpha = 0.1$. A typical example of E as a function of c_1 is shown in Fig. 5.11. The porosity c is assumed to be 0.01 in this example. The function E has only a minimum of zero. In other words, $\partial E/\partial c_1 = 0$ has a unique solution. Because of this, we can determine c_1 to give E_{min} by a numerical iteration procedure with no ambiguity. We used again the conjugate direction method.

The convergence for the iteration procedure was found in the order of 10^{-12} for E_{min} using $e = 10^{-5}$. We were able to determine the modeling parameters to agree perfectly the measured and the calculated normalized velocities. Because the order of E_{min} was equivalent to the previous model 4, the graphical expression for the agreement between them is equivalent to Fig. 5.6. Next, we discuss the change in parameters with the damage accumulation.

The inferred parameters are shown in Fig. 5.12. The oblate-ellipsoid volume fraction c_2 is also plotted, which is calculated from inferred c_1 with the measured porosity c. As the creep progresses, the two volume fractions increase. The ellipsoidal elements are sparsely scattered in the matrix, but they continue to grow in volume, containing more and more voids in them. High volume fraction c_1 shows that the voids of various sizes are closely packed in the ellipsoids. The effective moduli for the first step, which are derived by Weng [17], are
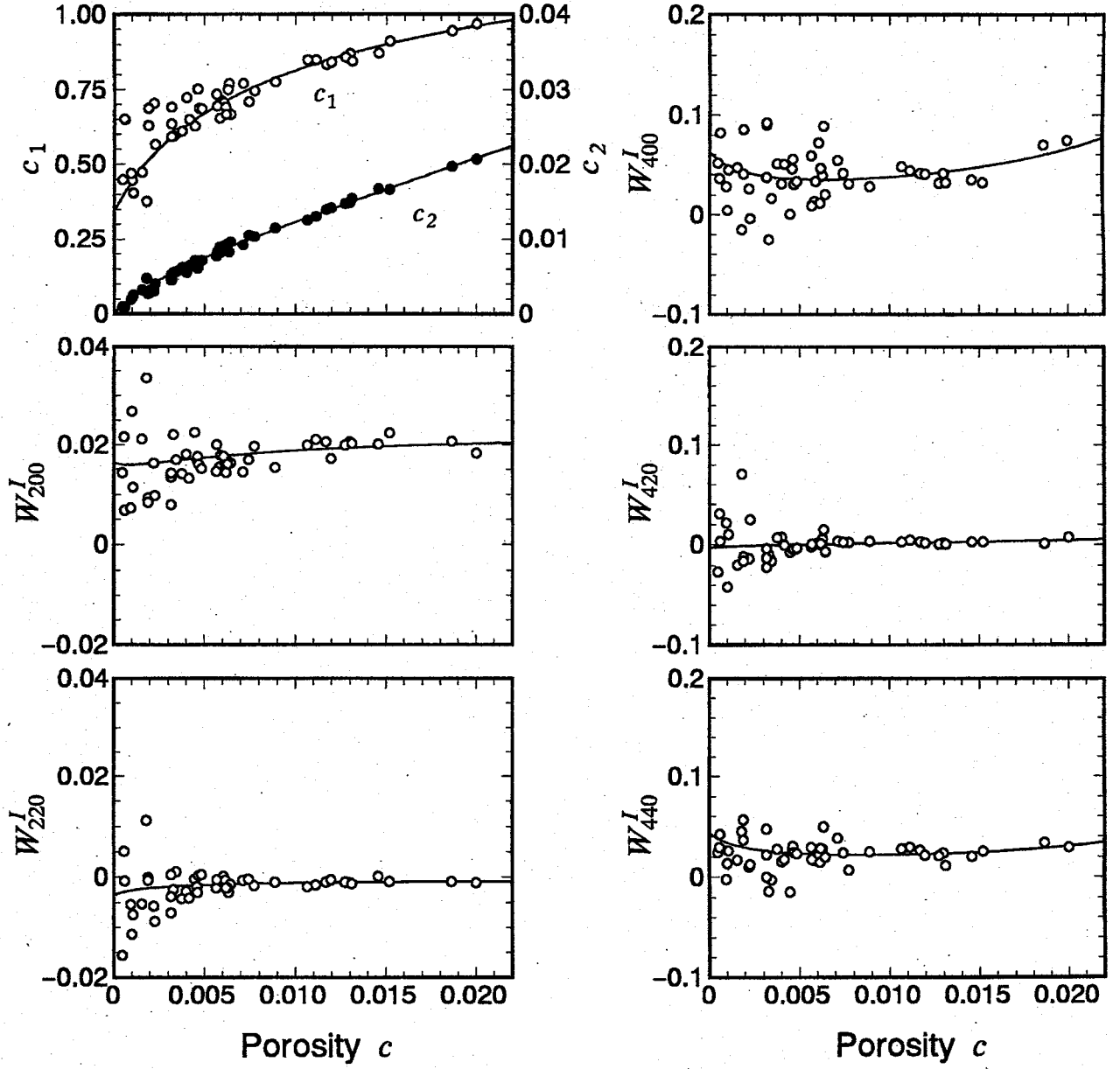
Fig. 5.12. Calculation results for model 5.

applicable to a dense concentration. Ledbetter and Datta [44] gave an alternative expression using a scattered-plane wave ensemble average model. These two approaches give the same values of effective moduli for random distribution of voids up to extremely high concentration (See Fig. 4.2).

The ODCs W_{2m0}^I are almost equivalent with those of partially oriented oblate voids model (model 4). W_{420}^I is nearly zero as in the previous model, but W_{400}^I and W_{440}^I apparently show a different tendency. In the double composite model, W_{400}^I increases as a whole with increasing c,
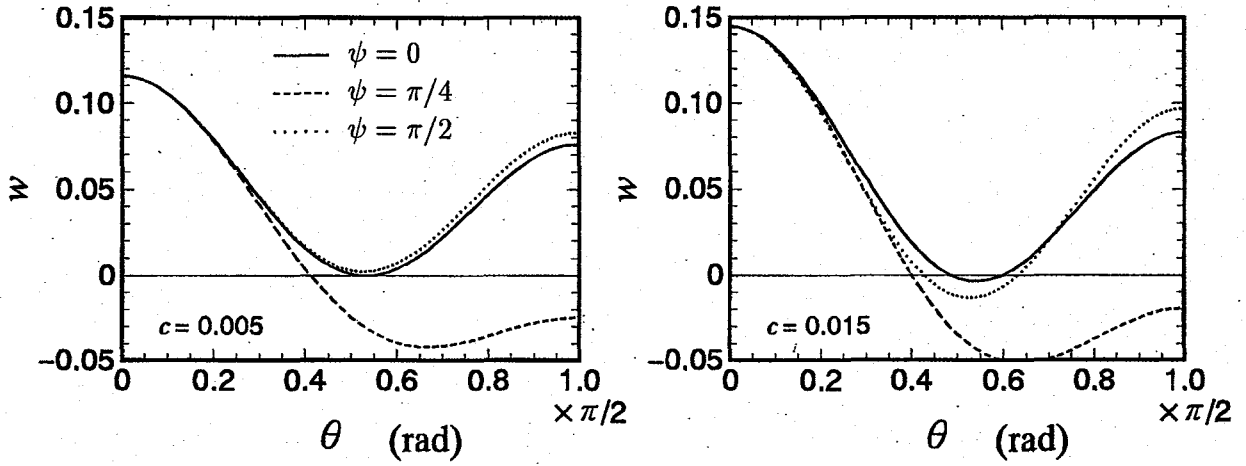
67
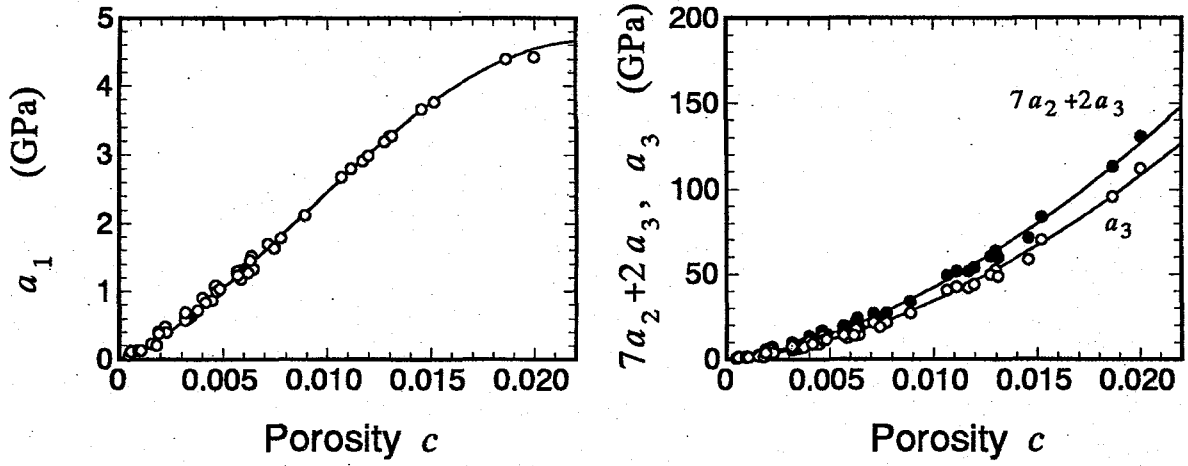
Fig. 5.13. Anisotropy factors for model 5.

Fig. 5.14. ODF w for model 5 truncated at $l = 4$.

and W_{440}^I is almost unchanged. The anisotropy factors are shown in Fig. 5.13. The anisotropy factors $7a_2 + 2a_3$ and a_3 are almost equivalent to those of the previous model, which affect the ODCs W_{2m0}^I. However, the anisotropy factor a_1 has a different tendency. The difference of W_{4m0}^I is caused by the difference on a_1.

The irrationality on W_{400}^I observed in the previous model was removed. The evolution of W_{200}^I and W_{400}^I indicates the anisotropy growth due to the preferential void formation within the grain boundaries perpendicular to the stress axis x_3. The unchanged W_{440}^I is also acceptable. The inferred ODF w by Eq.(4.66) at two porosities is shown in Fig. 5.14. The

ODF w demonstrates the progressive concentration around $\theta = 0$ as creep advances.

The changes of the parameters appear to be suitable as the creep damage model. The double composite model best explains the observations among the five models studied.

An alternative numerical procedure was attempted to determine the parameters. From Eq.(4.69), we obtain

$$\rho_*\{(V_{11}^*)^2 + (V_{22}^*)^2 + (V_{33}^*)^2 + 2(V_{23}^*)^2 + 2(V_{31}^*)^2 + 2(V_{12}^*)^2\} = 3\lambda_C + 12\mu_C. \qquad (5.7)$$

The equation is independent of the inclusion-ODCs and the crystallite-ODCs. We determined c_1 numerically to satisfy the equation, under a given porosity c with $\alpha = 0.1$ and $c_2 = c/c_1$. The inclusion-ODCs were determined by the simultaneous equation $\partial E/\partial W_{lm0}^I = 0$. The numerical results coincided with Fig. 5.12.

If we used cylindrical specimens, the inclusion orientation distribution could be assumed to be axis-symmetric. The independent ODCs are then W_{200}^I and W_{400}^I. We have four parameters, c_1, α, and the two ODCs, to the four independent velocities. In this case, all four parameters can be determined from the measured velocities. However, the prediction would be impossible. The supposition on the constant α is indispensable. Equation (5.7) holds for the case with $V_{11}^* = V_{22}^*$ and $V_{23}^* = V_{31}^*$. We have only one equation independent of ODCs. Therefore, only one void parameter is determined being independent of the number of the ODCs.

5.7 Summary

We explained the ultrasonic velocity change by creep voids modeling studies. The studies were based on the conclusion in chapter 3 that the normalized velocities excluded the texture effect. We characterized the three factors; the aspect ratio, the positional distribution, and the orientation distribution of non-spherical inclusions. The effective stiffness C_{ijkl}^C was obtained as functions of the modeling parameters. Five models were considered. The void factors are summarized in Table 5.1. From the qualitative discussions of models 1 - 3, it was concluded that the orientation distribution should be included.

In models 4 and 5, we supposed the statistically orthorhombic symmetry for the orientation distribution of oblate ellipsoids. Five independent ODCs were W_{2m0}^I ($m = 0, 2$) and W_{4m0}^I ($m = 0, 2, 4$). The void modeling parameters were the porosity c and the aspect ratio of oblate voids α in model 4 (partially oriented oblate voids model). In model 5 (double composite model), they were the void volume fraction in oblate volume element c_1, the volume fraction of oblate ellipsoids c_2, and the aspect ratio of them α. Measured porosity was used for the calculation. Only six parameters can be predicted because of the six velocities. A constant aspect ratio 0.1 was assumed in model 5 for the sake of supplement. The modeling parameters

Table 5.1. Comparison of void factors among models.

	shape of voids	positional distribution	orientational distribution
model 1	sphere	random	–
model 2	oblate ellipsoid	random	unidirectional
model 3	oblate ellipsoid	random	random
model 4	oblate ellipsoid	random	partially oriented
model 5	sphere	restricted to oblate areas	areas partially oriented

were predicted by the conjugate direction method so as to minimize the error function E for α in model 4 and for c_1 in model 5 with the simultaneous equations $\partial E/\partial W^I_{lm0} = 0$. The minimum of the function E_{min} was sufficiently small in the order of 10^{-12} for both models. We were able to determine the modeling parameters to yield the calculated velocities coincident with the measured velocities as a natural result. The modeling parameters have to represent the damage accumulation. On this view point, the last two models were investigated.

The result for aspect ratio in model 4 indicates the nucleation of oblate voids and the void growth to microcracks with the damage accumulation. The increase of two volume fractions in model 5 shows that the ellipsoidal elements are sparsely scattered in the matrix, but they continue to grow in volume, containing more and more voids in them. The void modeling parameters for both models represent suitably the generation and growth of voids.

Two ODCs W^I_{220} and W^I_{420} are approximated to be zero for both models as expected by the measured normalized velocities, $V^*_{11}/V^R_{11} \approx V^*_{22}/V^R_{22}$ and $V^*_{23}/V^R_{23} \approx V^*_{31}/V^R_{31}$. The estimated evolution of the remaining ODCs are summarized as Table 5.2. W^I_{200} were equivalent for both models, because of the equivalences of the anisotropy factors $7a_2 + 2a_3$ and a_3. The different tendencies for W^I_{400} and W^I_{440} were caused by a_1. The coefficient of W^I_{2m0} is a_3 for the longitudinal waves and $7a_2 + 2a_3$ for the shear waves, and that of W^I_{4m0} is a_1. Both W^I_{400} and W^I_{440} decrease in model 4. On the other hand, W^I_{400} increases and W^I_{440} is unchanged in model 5. Decreasing W^I_{400} in model 4 was not acceptable. Because W^I_{4m0} were remarkably larger than W^I_{2m0}, the ODF w is governed by W^I_{4m0}. Therefore, the distribution intensity at $\theta = 0$ decreased with the porosity. On the other hand, all ODCs for model 5 were acceptable. The ODF w demonstrated the enhanced concentration around $\theta = 0$ as creep advances. It was concluded from the change in ODCs that model 5 was better than model 4.

It is natural to suppose that the orientation distribution of oblate ellipsoids is statistically axial symmetric around the x_3 axis because of the unidirectional stress. In this case, $W^I_{220} = W^I_{420} = W^I_{440} = 0$ should be satisfied. However, the numerical results for models 4 and 5 showed $W^I_{440} \neq 0$, indicating that the inclusion orientation distribution is not ideally axial symmetric.

Table 5.2. Comparison of inferred ODCs.

	W_{200}^I	W_{400}^I	W_{440}^I
model 4	increase	decrease	decrease
model 5	increase	increase	unchanged

We surmised that the orthorhombic distribution of the oblate ellipsoid orientation is caused by that of the grain boundary misorientation, on which the nucleation and the growth of voids on the grain boundaries would depend.

Chapter 6

CONCLUSIONS

6.1 Summary

The effective stiffness of the particle reinforced composite has been studied. The theories are applicable to porous materials, and we applied them to the creep damaged material. An interpretation of the ultrasonic velocity change due to creep voids is presented through the void modeling and the calculation of the effective stiffness. For the simplicity, we adopted four assumptions to give the theoretical discussions:

(1) No precipitation of the second phase particles,

(2) No texture modification,

(3) No dislocation restructuring,

(4) No interaction between the effects of voids and texture.

The first three assumptions are introduced to ignore the metallurgical attributes, which are obstructive in the concept of voids/matrix composite. The last is introduced to give an simple procedure in calculating the approximated effective stiffness supposing the isotropic matrix composite.

The work is summarized as following. The experiment was described in chapter 2, where we made the best possible procedures to carry out a simple experiment for bing compatible with the theoretical analysis. To avoid the precipitation, pure copper was used. To suppress the texture modification by the recrystallization, a stabilization annealing was provided prior to the creep tests. The test conditions were chosen for the brittle failure to occur. The porosity and the ultrasonic velocities were measured for coupon samples at various times to rupture. Ultrasonic velocities showed an orthorhombic anisotropy even in the initial state. They decreased and the anisotropy developed with increasing porosity due to creep voids.

In chapter 3, the anisotropic deviation stiffness due to texture is separated. We gave the macroscopic elastic stiffness in reference (uncrept) sample as $C^R_{ijkl} = C^M_{ijkl} + \Delta C^T_{ijkl}$ using

the ODF to represent the crystallite orientation distribution in polycrystallite metals. The expression was used in the numerical calculation to determine C_{ijkl}^M and ΔC_{ijkl}^T. The theoretical assumption (4) was supported by $|\Delta C_{ijkl}^T / C_{ijkl}^M| \ll 1$. It allowed the supposition of the isotropic matrix in the calculation of the effective stiffness in damaged samples, so the expression of $C_{ijkl}^* = C_{ijkl}^M + \Delta C_{ijkl}^T + \Delta C_{ijkl}^V$ was acceptable. It was concluded that the normalized velocities don't contain the texture effect.

The effective stiffness $C_{ijkl}^C = C_{ijkl}^M + \Delta C_{ijkl}^V$ of a composite comprising the isotropic copper matrix and the inclusions was obtained for three cases in chapter 4. We have four aspects of the inclusions; the volume fraction, the shape, the positional distribution, and the orientation distribution of non-spherical inclusion. Theoretical case studies in this chapter assumed the random distribution of the position.

Five models for creep damage were investigated in chapter 5. From the qualitative discussions on the first three trial models, it was concluded that the inclusion orientation distribution should be taken into account. In model 4 (partially oriented oblate voids model), the oblate voids were randomly positioned in the matrix. In model 5 (double composite model), the oblate volume elements containing the spherical voids were randomly positioned in the matrix. Non-random positional distribution of voids was given by the hierarchical structure. The modeling parameters were determined so as to give a coincidence between the calculated and measured velocities. The coincidence is a natural result because of the six parameters to the six velocities. However, the parameters have to represent the damage process suitably. The changes in void parameters appear to be suitable for both models. The features of the ODF leaded to the conclusion that model 5 was superior in explaining the evolution of creep damage. In this model, the ellipsoidal elements are sparsely scattered in the matrix, but they continue to grow in volume, containing more and more voids in them. The elastic anisotropy develops with the preferential void formation within the grain boundaries perpendicular to the stress axis.

6.2 Discussions

The five models are relatively simple compared with the real situations. To express the void state more appropriately, a more involved model is required. We consider, for example, the partially oriented oblate spheroidal elements including oblate spheroidal voids. In the second step to obtain the effective stiffness, the composite consists of the isotropic matrix and anisotropic inclusions. The problem would be difficult. We assumed the same shape for all voids or inclusions in the matrix in this study. It would be also complicated to introduce the distribution of the aspect ratio. Anyway, it would be impossible to determine the void

parameters, because we can determine only one using the isotropic function unconnected with the ODCs.

The concept of this work, the effective stiffness of the creep damaged material, is applicable to the heat resistant materials involving metallurgical complexity. Micromechanics of dislocations and inclusions in anisotropic matrix is highly complicated, but the problems is treated in the book of Mura [2]. We now discuss the remaining two assumptions used in this work for the simplicity.

In the heat resistant alloys, the precipitation of the second phase particles such as carbide and intermetallic compounds occurs during creep. The effect on the effective stiffness will be investigated by a three-phase composite modeling consists of matrix, voids, and precipitated inclusions. The effective stiffness of a two-phase composite consists of matrix and inclusions can be calculated if the inclusion material is identified. It is recast as the stiffness of matrix for the next step, where the additional effect of voids is involved. The inclusion volume fraction would be approximated by the ultrasonic velocity measurements for the sample with the same thermal history and no stress.

If the texture modification occurs during creep, the stiffnesses in reference sample and in damaged sample are written as

$$C_{ijkl}^R = C_{ijkl}^M + \Delta C_{ijkl}^{TR},$$
$$C_{ijkl}^* = C_{ijkl}^M + \Delta C_{ijkl}^{TD} + \Delta C_{ijkl}^V. \tag{6.1}$$

The texture effect, ΔC_{ijkl}^{TR}, in reference samples is modified to ΔC_{ijkl}^{TD} due to the texture change during the creep. From these equations, the normalized velocity reduces to

$$\frac{V_i^*}{V_i^R} = \sqrt{\frac{1}{1-c}\frac{1}{C_i^M}(C_i^C + \Delta C_i^{TD} - \Delta C_i^{TR})}, \tag{6.2}$$

within the first order approximation. The texture modification gives rise to $\Delta C_{ijkl}^{TD} - \Delta C_{ijkl}^{TR}$, which affects the normalized velocities. The explicit form of C_{ijkl}^* is given as

$$C_{11}^* = \lambda_C + 2\mu_C + \frac{8\sqrt{10}}{105}\pi^2 a_3 \left(W_{200}^I - \sqrt{6}W_{220}^I\right)$$

$$+ \frac{12\sqrt{2}}{35}\pi^2 a \left(\bar{W}_{400} - \frac{2\sqrt{10}}{3}\bar{W}_{420} + \frac{\sqrt{70}}{3}\bar{W}_{440}\right),$$

$$C_{22}^* = \lambda_C + 2\mu_C + \frac{8\sqrt{10}}{105}\pi^2 a_3 \left(W_{200}^I + \sqrt{6}W_{220}^I\right)$$

$$+ \frac{12\sqrt{2}}{35}\pi^2 a \left(\bar{W}_{400} + \frac{2\sqrt{10}}{3}\bar{W}_{420} + \frac{\sqrt{70}}{3}\bar{W}_{440}\right),$$

$$C_{33}^* = \lambda_C + 2\mu_C - \frac{16\sqrt{10}}{105}\pi^2 a_3 W_{200}^I + \frac{32\sqrt{2}}{35}\pi^2 a \bar{W}_{400},$$

$$C_{44}^* = \mu_C - \frac{2\sqrt{10}}{315}\pi^2 (7a_2 + 2a_3)\left(W_{200}^I - \sqrt{6}W_{220}^I\right)$$

$$- \frac{16\sqrt{2}}{35}\pi^2 a \left(\bar{W}_{400} + \sqrt{\frac{5}{2}}\bar{W}_{420}\right),$$

$$C_{55}^* = \mu_C - \frac{2\sqrt{10}}{315}\pi^2 (7a_2 + 2a_3)\left(W_{200}^I + \sqrt{6}W_{220}^I\right)$$

$$- \frac{16\sqrt{2}}{35}\pi^2 a \left(\bar{W}_{400} - \sqrt{\frac{5}{2}}\bar{W}_{420}\right), \tag{6.3}$$

$$C_{66}^* = \mu_C + \frac{4\sqrt{10}}{315}\pi^2 (7a_2 + 2a_3) W_{200}^I + \frac{4\sqrt{2}}{35}\pi^2 a \left(\bar{W}_{400} - \sqrt{70}\bar{W}_{440}\right),$$

$$C_{23}^* = \lambda_C + \frac{4\sqrt{10}}{315}\pi^2 (7a_2 - a_3)\left(W_{200}^I - \sqrt{6}W_{220}^I\right)$$

$$- \frac{16\sqrt{2}}{35}\pi^2 a \left(\bar{W}_{400} + \sqrt{\frac{5}{2}}\bar{W}_{420}\right),$$

$$C_{31}^* = \lambda_C + \frac{4\sqrt{10}}{315}\pi^2 (7a_2 - a_3)\left(W_{200}^I + \sqrt{6}W_{220}^I\right)$$

$$- \frac{16\sqrt{2}}{35}\pi^2 a \left(\bar{W}_{400} - \sqrt{\frac{5}{2}}\bar{W}_{420}\right),$$

$$C_{12}^* = \lambda_C - \frac{8\sqrt{10}}{315}\pi^2 (7a_2 - a_3) W_{200}^I + \frac{4\sqrt{2}}{35}\pi^2 a \left(\bar{W}_{400} - \sqrt{70}\bar{W}_{440}\right),$$

where

$$\bar{W}_{4m0} = \frac{a_1}{3a}W_{4m0}^I + W_{4m0}^{TD}, \quad m = 0, 2, 4.$$

The anisotropy factor of single crystal a is a constant. The isotropic elastic constants λ_C and μ_C, and the anisotropy factors a_j ($j = 1, 2, 3$) are given by the void parameters; c and α in model 4, c_1, c_2, and α in model 5. The ODCs W_{4m0}^I and W_{4m0}^{TD} are not independent to each other. It is then impossible to determine each ODC from the velocities. If W_{4m0}^{TD} is obtained by x-ray or neutron diffraction technique, W_{4m0}^I can be predicted by the measured porosity and velocities.

One of the practical applications of the modeling studies would be the estimation of creep life. Some of high temperature components in fossil fuel power plants have been used over the

designed lives, 15 years or 10^5 hours [51]. This is partly because the stationary projects for new plants result from a great fund of construction, the difficulty for procurement of a site, and the severe controls over environment. Moreover, the overage components have been used in more and more severe operating conditions, such as daily starting-stopping with the electric power demand. After the long term operation, the damage has accumulated even in low stress portions and may lead to the eventual failure. Their fracture would give catastrophic hit to the social and economical activities. Evaluation of their damage has been desired for the prevention of hazardous fracture and the extension of life. The evaluation for the ductile failure, the transgranular creep process, is achieved by the measurement of elongation or deformation.

The hardly accessible situation is the brittle fracture, that is, the intergranular creep process. It is revealed that the ultrasonic velocities are sensitive to such damaging process, while the damage state cannot detect from the conventional technique, say, measuring the elongation.

Ultrasonic velocity measurement is one of the nondestructive means proposed for continuously monitoring the damage evolution in high-temperature components. Ultrasonics detects the internal damage state. Other techniques mainly sense the surface and the surface region. Because the creep damage is distributed over the entire body in general, ultrasonics supplements the information from other techniques. Moreover, ultrasonics is easy for the measurements. At the present time, the effect of creep damage on ultrasonic velocities is inconclusive. In some cases, the velocity decreases with the damage accumulation [33] [52] -[55], while in others, this tendency is not observed [56] -[58]. Such confusion results from the diversity of creep damage in the high-temperature steel alloys. A number of metallurgical attributes occurring in creep process may affect the ultrasonic velocities.

The modeling studies provide a basis for understanding complicated and important phenomena of metals creep. The development of ultrasonic methods for the reliable estimation of creep remaining life would be supported by the studies.

Appendix A

ULTRASONIC BACKSCATTERING DUE TO CREEP VOIDS IN COPPER

A.1 Introduction

When the ultrasonic pulse wave passes through a porous material, it is partly scattered by voids. Faint scattered waves from a large number of voids are superimposed, and the backscattering noise is detected by the transducer at incidence surface [57, 59]. Creep voids would be estimated nondestructively by the backscattering noise measurements. This measurement offers an alternative access to the creep voids, although the theoretical background is still under development [60].

A.2 Experiment

Reference (uncrept) and damaged samples described in chapter 2 are used again. Experimental setup is shown in Fig. A.1. An electric pulse generated by a pulser is fed to a transducer through a diplexer. The transducer inputs an ultrasonic pulse to the specimen. When the ultrasonic pulse travels through a creep damaged specimen, it scatters slightly due to voids. The transducer receives the backscattering noise that is a integration of faint scattered waves from a great number of voids. Receiver amplifies the backscattering noise and
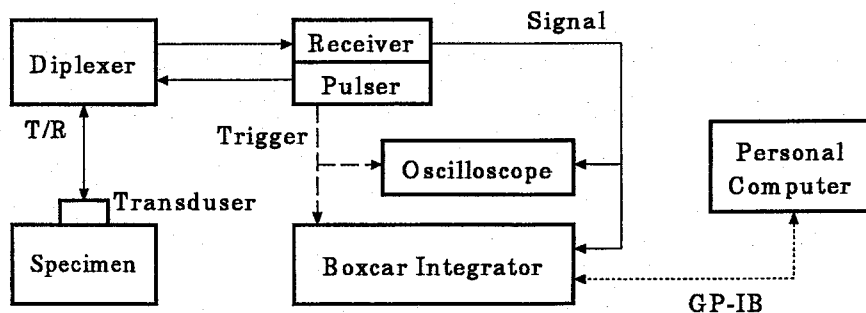

Fig. A.1. Experimental setup.

79

sends it to boxcar integrator (waveform recorder). A personal computer is connected to the boxcar integrator through GP-IB, controls it, and processes the measured data. The receiver has the amplification rate ranging from -12 to 67 dB. The maximum amplitude of input signal to the boxcar integrator is ± 1.0 V. The vertical resolution is 10 bits.

The longitudinal ultrasonic wave was generated by the piezoelectric transducer of 6 mm diameter. The center frequency was 10 MHz. To make full use of the vertical resolution of the boxcar integrator, the received noise was amplified by the receiver. Through the experiment, all the measuring parameters were fixed except for the amplification rate of the receiver. The noise waveform before the first echo arrival was taken as shown in Fig. A.2. Taking sixty-four time average for the waveform in the boxcar integrator, the random noise was eliminated and only the backscattering noise from creep voids survived.

We define the noise intensity I as the rms (root mean square) value:

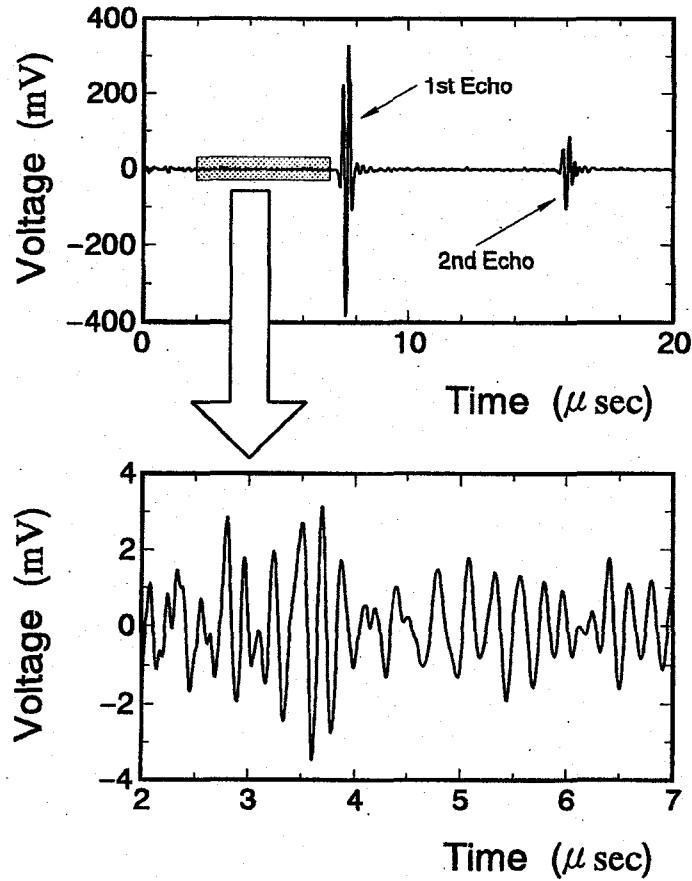$$I = \sqrt{\frac{1}{t_2 - t_1} \int_{t_1}^{t_2} V^2 dt}, \qquad (A.1)$$

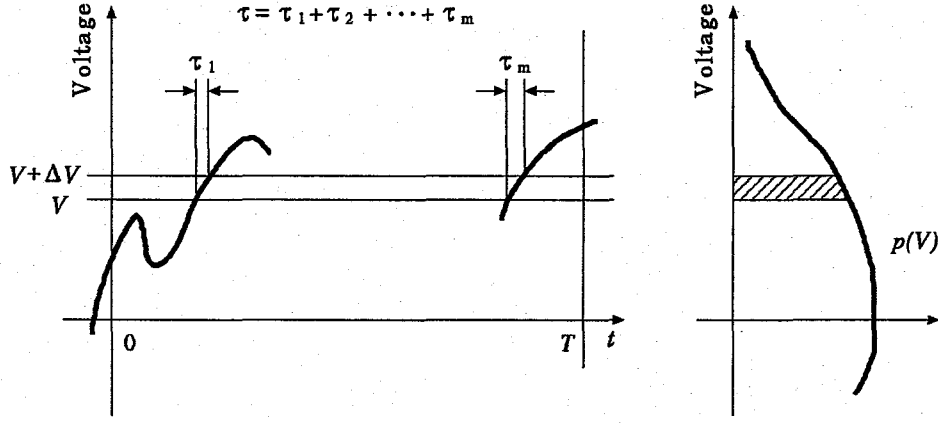Fig. A.2. Ultrasonic backscattering noise.

80

Fig. A.3. Backscattering noise and probability density.

where V is the voltage of backscattering noise and is shifted to zero average in order to eliminate the drift in the circuit. We denote the sum of the time period by τ, when the noise voltage exists in a range from V to $V + \Delta V$. The probability is, as illustrated in Fig. A.3,

$$\int_V^{V+\Delta V} p(V)dV = \lim_{T \to \infty} \frac{\tau}{T},$$

where $p(V)$ is a probability density. The average μ and the variance σ^2 are defined by, respectively,

$$\mu = \int_{-\infty}^{\infty} Vp(V)dV,$$

$$\sigma^2 = \int_{-\infty}^{\infty} V^2p(V)dV - \mu^2.$$

They are rewritten as

$$\mu = \lim_{T \to \infty} \frac{1}{T} \int_0^T Vdt,$$

$$\sigma^2 = \lim_{T \to \infty} \frac{1}{T} \int_0^T V^2dt - \mu^2.$$

In this experiment the average μ is always zero. Therefore the noise intensity I corresponds to the standard deviation σ if the observed time width $t_2 - t_1 = T$ is long enough.

Because V is a time series of discrete data, we calculate the noise intensity by

$$I = \sqrt{\frac{1}{n} \sum_{i=1}^{n} V_i^2}, \qquad (A.2)$$
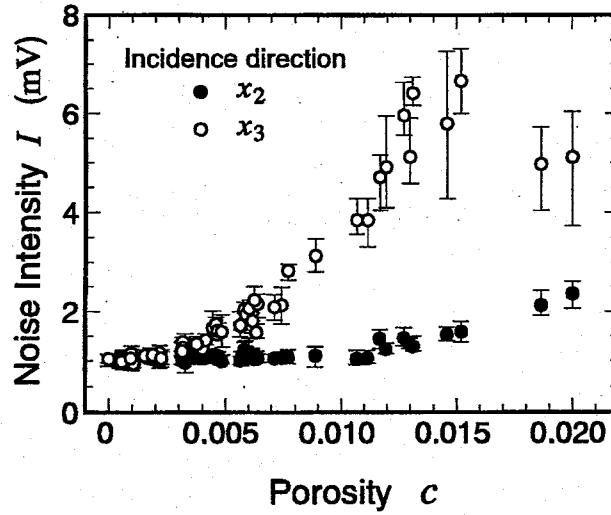
Fig. A.4. Relation between porosity c and noise intensity I.

where n is the number of sampling points. In this experiment we fixed $t_2 - t_1 = 5$ μs and $n = 1024$. We measured the noise intensity I for longitudinal ultrasonic waves propagating in x_i $(i = 1, 2, 3)$ direction (see Fig. 2.1).

The relation between porosity c and noise intensity I is shown in Fig. A.4. Because the result for ultrasonic wave propagating in x_1 direction is almost the same as that in x_2 direction, we omitted the result. The noise intensity I at $c = 0$ corresponds to the backscattering noise from the grain boundaries, and it indicates the equiaxial grain shape and a weak texture at the same time. The ultrasonic velocities in the reference samples showed the anisotropy due to the rolling texture as shown in Table 2.2. Hirao et al. [61] showed the strong anisotropy of I depending on the propagation direction in textured pure titanium. The annealed copper samples in this experiment have a weak texture, but the initial values of I are insensitive to the direction. The change in I for creep damaged samples is caused only by the backscattering from voids because of the assumptions of no texture modification, no precipitation of the second phase, and no dislocation restructuring. The noise intensity I for the x_2 direction remains unchanged in the range of $c < 0.01$, and then it increases slowly with increasing c. On the other hand, the noise intensity I for the x_3 direction, that is the stress direction, is sensitive to c. I increases with c in a parabolic way until it reaches a maximum at approximately $c = 0.014$, saturates, and then it decreases.

A.3 Discussion

The dependence of noise intensities on the propagation direction can be explained by the positional distribution of creep voids. As shown in Fig. 2.3, voids are not randomly positioned. They tend to gather preferentially on the grain boundaries perpendicular to the x_3 direction. If the voids line up in the propagation direction, the number of voids that cause the scattering will be limited. Therefore we conclude that the projective area of voids on the incident surface decides the noise intensity. The equivalence between the noise intensity in the x_1 direction and that in the x_2 direction is similar to the velocity equality of $V_{11}^*/V_{11}^R \approx V_{22}^*/V_{22}^R$.

The multiple scattering or the interference can be considered for the reason of maximum noise intensity in the x_3 direction. Increasing the number of voids, the scattering waves don't arrive at the transducer because of the secondary scattering. Moreover, if too many scattering waves of various phases overlap each other, they cancel out each other and the amplitude becomes smaller through interference. Hirao et al. [61] calculated the backscattering noise intensity from the grain boundaries, and showed that there was a maximum in the relation between the grain size and the noise intensity.

A.4 Summary

The noise intensity I for the perpendicular direction to the stress is unchanged until the beginning of the final stage, and then it increases slowly with increasing c. On the other hand, I for the stress direction increases with c in a parabolic way until it reaches the maximum at approximately $c = 0.014$, and then it decreases. The dependence of I on the propagation direction can be explained by the positional distribution of creep voids. The existence of the maximum intensity in the stress direction may result from the multiple scattering and/or the interference among the scattered signals.

From the practical viewpoint, the high sensitivity of I seems promising, particularly in the x_3 direction, where I increases in a factor of 7 or more. Also, the measurement of I doesn't require the opposite surfaces of the parts. However, we cannot measure I in the stress direction in many cases and the measurement is vulnerable to the surface conditions. After all, it lacks the theoretical background for interpretation.

The use of a transducer with higher frequencies should be attempted. It may give the more sensitive response to the voids. Angle beam method would be useful instead of the normal incidence like the present measurement. Detailed measurements around the maximum intensity would be required.

Appendix B

CREEP LIFE ESTIMATION BASED ON DAMAGE GROWTH EQUATION

B.1 Introduction

The author previously proposed a method for the nondestructive estimation of creep life using ultrasonic velocities. It makes use of the relation between the consuming rate of life and the normalized velocities. We will now discuss another method based on the damage growth equation. The method doesn't need any master curves, but it requires several measurements. It was proposed by Ihara et al. [62]. We will apply this phenomenological method to the measured values in chapter 2; the porosity and the normalized velocities.

B.2 Damage growth equation

The damage growth equation can be written as

$$\frac{dD}{dt} = f(D, \sigma, T) \qquad (B.1)$$

for creep damage growth, where t is the time, σ is the stress, and T is the temperature. Variable D is the monotonically increasing parameter to indicate the present state of damage. It is defined so that it varies from 0 in virgin material to 1 at failure. Several equations have been proposed [63]-[65]. They reduce to

$$\frac{dD}{dt} = \frac{A}{(1 - D)^k}, \qquad (B.2)$$

where A (> 0) and k (≥ 1) are the material constants depending on σ and T. The equation simply shows the finite rate A at $D = 0$ and the infinite rate at $D = 1$. The difference of the proposed equations is the definition of constant A. The damage dependence $1/(1 - D)^k$ is common.
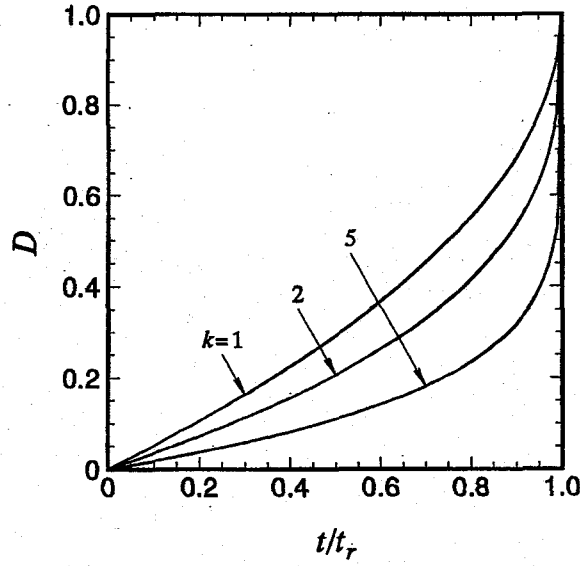
Fig. B.1. Influence of constant k on the damage curve.

Ihara et al [62] rewrote the equation using the rupture time t_r. Taking the integration, the equation can be rewritten as

$$-\frac{1}{k+1}(1-D)^{k+1} = At + C. \tag{B.3}$$

The above equation has to be satisfied $D = 0$ at $t = 0$, we thus obtain $C = -1/(k+1)$. Taking $D = 1$ at $t = t_r$, one has

$$t_r = \frac{1}{(k+1)A}. \tag{B.4}$$

The rupture time t_r is decided by k and A, which is the damage growth rate at $t = 0$. Finally, Eq.(B.3) reduces to

$$D = 1 - \left(1 - \frac{t}{t_r}\right)^{1/(k+1)}. \tag{B.5}$$

This equation indicates that the relation between the damage variable D and the normalized time t/t_r depends only on k. The influence of constant k on the damage curve is illustrated in Fig. B.1.

B.3 Estimation of creep life

Our objective is to estimate t_r based on Eq.(B.5) from the measured data (t_i, D_i). Schematic illustration for this method is shown in Fig. B.2. The damage growth curve can be obtained
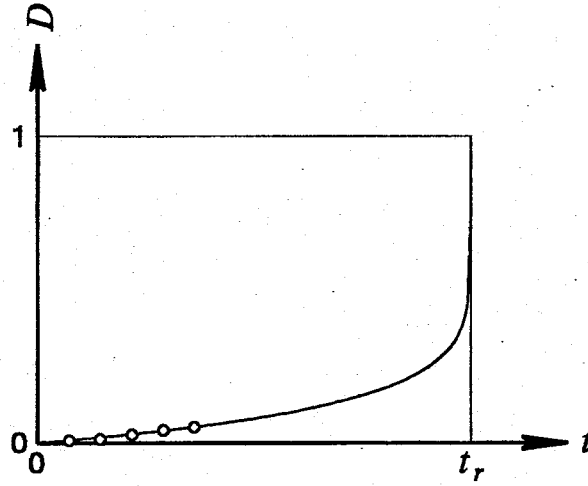
Fig. B.2. Estimation of t_r based on the damage growth equation from the measured data (t_i, D_i).

by fitting to the given sets of data (t_i, D_i) and the values for the parameters, t_r and k, are given.

We define an error function as

$$E = \sum_{i=1}^{n} \left[D_i - \left\{ 1 - \left(1 - \frac{t_i}{t_r} \right)^{1/(k+1)} \right\} \right]^2 , \tag{B.6}$$

where n is the number of data. We determine t_r and k so as to minimize E by the conjugate direction method. We denote the estimated t_r by $\hat{t}_r$ to distinguish from the measured t_r.

We will calculate $\hat{t}_r$ for copper samples used in this thesis. The stress was 6.0 MPa and the temperature was 500 °C and 550 °C. In this study, D is simply defined by the porosity c as $D = c$, or $D = 1 - V^*/V^R$ by the ultrasonic velocity, where V^R and V^* denote the velocities

Table B.1. Estimated $\hat{t}_r$ for copper samples crept at 6.0 MPa, $t_r = 597.8$ hr at 500 °C, $t_r = 270.8$ hr at 550 °C.

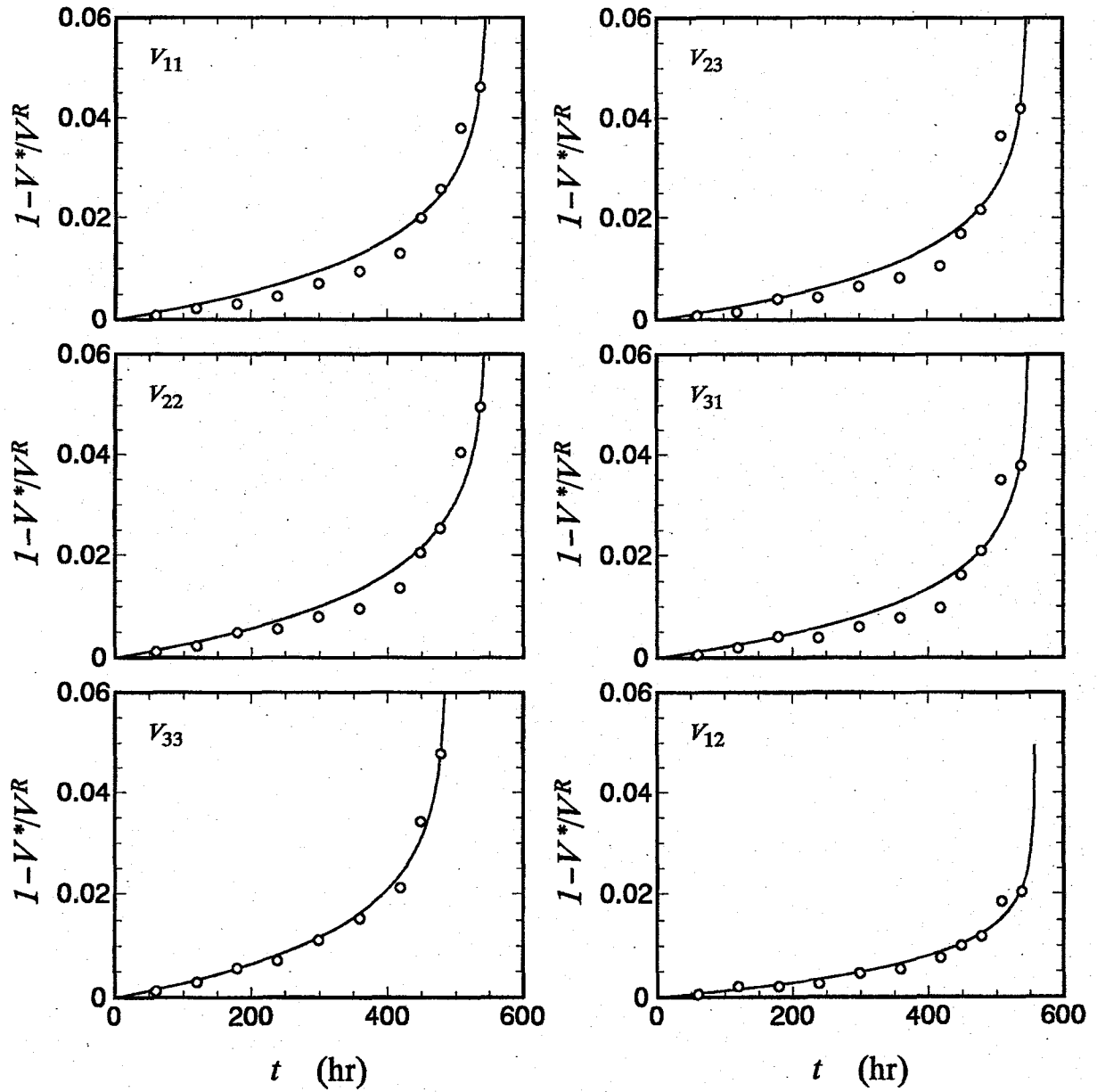|	500 °C		550 °C	
	$\hat{t}_r$ (hr)	k	$\hat{t}_r$ (hr)	k
c	585.0	119.9	324.4	96.93
V_{11}	547.9	81.65	269.9	92.89
V_{22}	546.7	78.65	270.4	85.29
V_{33}	486.8	80.63	261.8	51.34
V_{23}	547.2	91.61	271.1	100.5
V_{31}	549.6	95.13	269.2	110.5
V_{12}	557.2	156.6	290.4	157.0

Fig. B.3. Fitting curves of $D = 1 - V^*/V^R$ for the crept copper samples at 500 °C, $t_r = 597.8$ hr.

in the reference and damaged samples, respectively. The definition $D = 1 - V^*/V^R$ follows Ihara et al. [62]. The measurements in chapter 2 are not the data monitored throughout with a specimen. The data includes a scatter originating from the metallurgical inhomogeneity, which causes a variation in the rupture time or the damage accumulation rate in the individual specimens. Relatively small difference in the rupture time as shown in Table 2.1 encourages us to apply the estimation.

The numerical results are shown in Table B.1. The velocity V^*_{33} at 500 °C was not obtain-
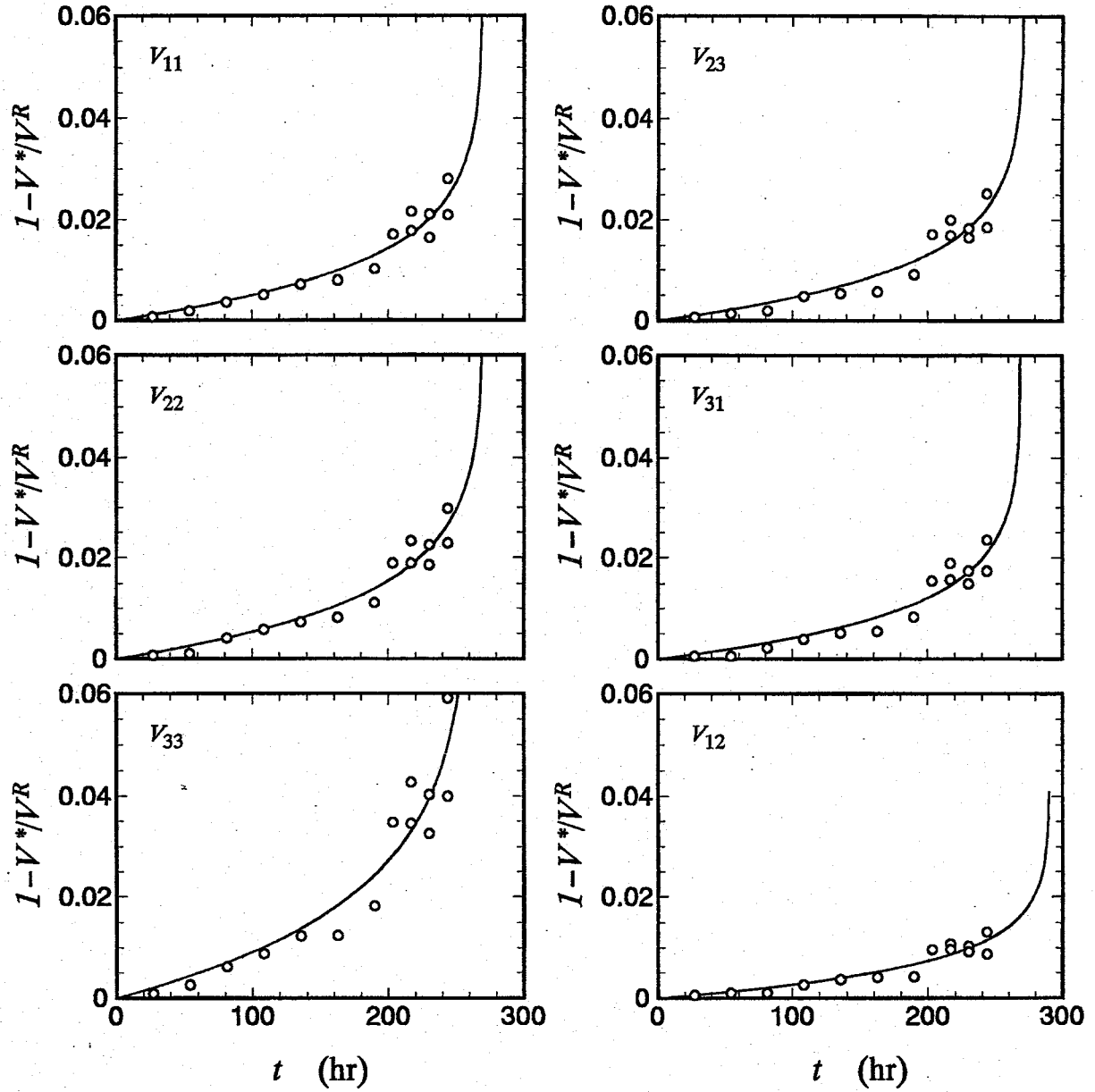
Fig. B.4. Fitting curves of $D = 1 - V^*/V^R$ for the crept copper samples at 550 °C, $t_r = 270.8$ hr.

able for $t/t_r \geq 0.85$. The calculation was made using V_{33}^* up to $t/t_r \leq 0.80$. Good estimations for $\hat{t}_r$ were achieved except for V_{33} at 500 °C. The fitting curves for the porosity have already been presented in Fig. 2.5. Those for the velocities are shown in Fig. B.3 and in Fig. B.4. They represent well the porosity evolution and the velocity change, for which Eq.(B.5) is a good approximation.

Figure B.5 shows $\hat{t}_r/t_r$ depending on t/t_r. The value of $\hat{t}_r$ at $t/t_r = 0.3$ is, for instance, estimated by the data up to $n = 3$. We observe that involving the data at the late stages con-
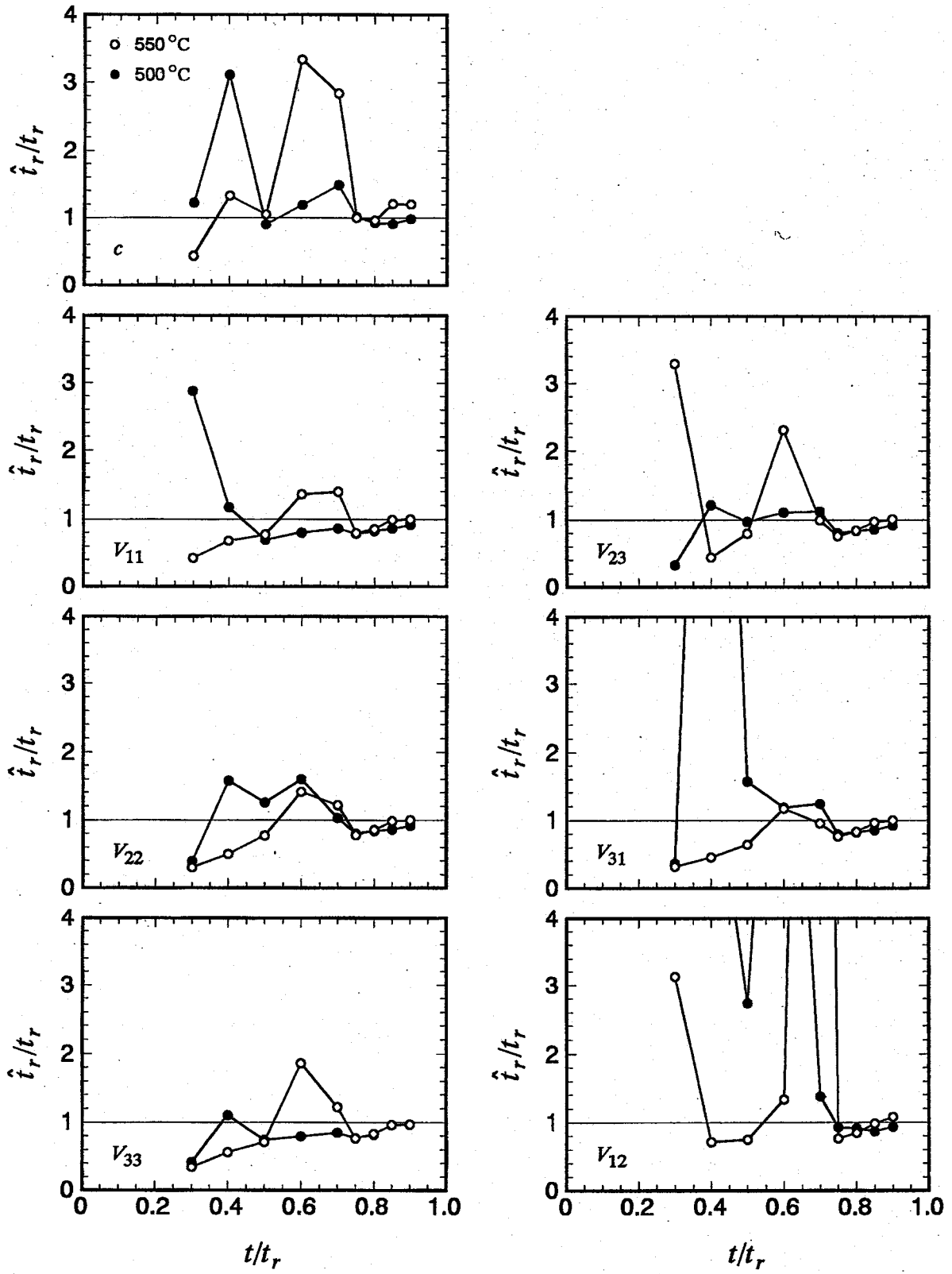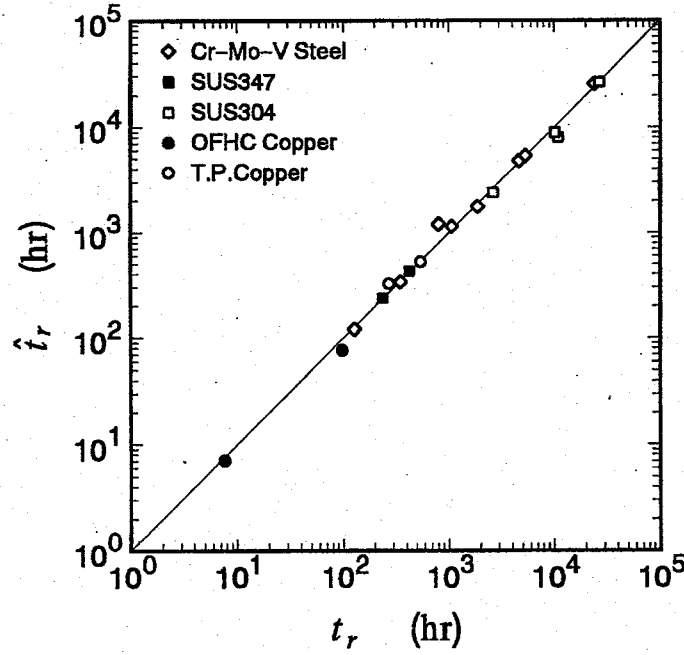
Fig. B.5. Estimated $\hat{t}_r$ depending on t/t_r.

Fig. B.6. Comparison of the estimated $\hat{t}_r$ with the measured t_r.

siderably improves the estimation. The unsatisfactory estimation results from the measuring error or the metallurgical inhomogeneity in the individual specimens, because D and dD/dt are both extremely small in the initial and the middle stages. To obtain a good estimation even in the early stage, the data containing less error and/or a large number of data n are required.

We apply the estimation based on the porosity to other metals. The change in density has been measured for Cr-Mo-V steel [22], OFHC copper [23], SUS347 [31], and SUS304 [32]. In the heat resistant materials, the change in density is caused by the precipitation of the second phase particles in addition to the generation of voids. We adopt the specimen head, having the same thermal history with the gauge position, as the reference sample. The porosity is calculated by Eq.(2.1) in all cases. The number of data is $n = 3 \sim 6$, and the measurements were done from the initial stage to the final stage. The comparison of the estimated $\hat{t}_r$ with the measured t_r is shown in Fig. B.6 including the present measurement on tough pitch copper. The agreement is just excellent despite the large range of t_r.

B.4   Summary

We applied the estimation of the creep life based on the damage growth equation to the crept copper samples used in chapter 2. Two definitions for the damage variable D were

attempted: $D = c$ and $D = 1 - V^*/V^R$. The damage growth equation represents well the porosity evolution and the velocity change. The creep life was estimated successfully. The definition by the porosity with the careful measurements gives a good estimation for other metals.

The porosity is not obtained nondestructively. For the practical use of Eq.(B.5), the nondestructive measurement for the continuous monitoring of the damage is necessary. Ultrasonic velocities can be applied for the purpose. As described in Appendix A, the backscattering noise intensity propagated in the transverse direction to the stress holds the initial value even in the middle stage. The other technique should be attempted.

REFERENCES

[1] R.M.Christensen. *Mechanics of Composite Materials.* John Wiley & Sons, New York, 1979.

[2] T.Mura. *Micromechanics of Defects in Solids.* Kluwer Academic Publishers, Dordrecht, 1987.

[3] M.Taya and R.J.Arsenault. *Metal Matrix Composites, Thermomechanical Behavior.* Pergamon Press, New York, 1989.

[4] J.Aboudi. *Mechanics of Composite Materials, A Unified Micromechanical Approach.* Elsevier Science Publishers, New York, 1991.

[5] K.Z.Markov. *Advances in Mechanical Modeling of Composite Materials.* World Scientific Publishing, Singapore, 1994.

[6] J.M.Dewey. The elastic constants of materials loaded with non-rigid fillers. *J. Appl. Phys.*, 18:578, 1947.

[7] J.D.Eshelby. The determination of the elastic field of an ellipsoidal inclusion, and related problems. *Pro. R. Soc. London*, A241:376, 1957.

[8] W.B.Russel and A.Acrivos. On the effective moduli of composite materials: Slender rigid inclusions at dilute concentrations. *Z. Angw. Math. Phys.*, 23:434, 1972.

[9] E.H.Kerner. The elastic and thermoelastic properties of composite media. *Proc. Phys. Soc.*, 69:808, 1956.

[10] C.van der Pol. On the theology of concentrated dispersions. *Rheol. Acta.*, 1:198, 1958.

[11] R.M.Christensen and K.H.Lo. Solutions for effective shear properties in three phase sphere and cylinder models. *J. Mech. Phys. Solis*, 27:315, 1979.

[12] A.V.Hershey. The elasticity of an isotropic aggregate of anisotropic cubic crystals. *J. Appl. Mech.*, 21:236, 1954.

[13] E.Kröner. Berechnung der elastischen Konstanten des Vielkristalls aus den Konstanten des Einkristalls. *Z. Phys.*, 151:504, 1958.

[14] R.Hill. A self-consistent mechanics of composite materials. *Mech. Phys. Solids*, 13:213, 1965.

[15] B.Budiansky. On the elastic moduli of some heterogeneous materials. *J. Mech. Phys. Solids*, 13:223, 1965.

[16] T.Mori and K.Tanaka. Average stress in matrix and average elastic energy of materials with misfitting inclusions. *Acta Metall.*, 21:571, 1973.

93

[17] G.J.Weng. Some elastic properties of reinforced solids, with special reference to isotropic ones containing spherical inclusions. *Int. J. Engng. Sci.*, 22:845, 1984.

[18] G.P.Tandon and G.J.Weng. The effect of aspect ratio of inclusions on the elastic properties of unidirectionally aligned composites. *Polymer Composites*, 5:327, 1984.

[19] G.P.Tandon and G.J.Weng. Average stress in matrix and effective moduli of randomly oriented composites. *Composite Sci. Tech.*, 27:111, 1986.

[20] Y.H.Zhao, G.P.Tandon, and G.J.Weng. Elastic moduli for a class of porous materials. *Acta Mechanica*, 76:105, 1989.

[21] A.Bhattacharyya and G.J.Weng. Theoretical calculation of the stress-strain behavior of dual-phase metals with randomly oriented spheroidal inclusions. *Metallurgical and Materials Trans.*, 27A:2359, 1996.

[22] N.Shinya, J.Kyono, and S.Yokoi. An assessment of creep damage by density change measurements for Cr-Mo-V steel. *ISIJ*, 70:573, 1984.

[23] R.C.Boettner and W.D.Robertson. A study of the growth of voids in copper during the creep process by measurement of the accompanying change in density. *Trans. Metall. Soc. AIME*, 221:613, 1961.

[24] A.Gitting. The mechanism of cavitation in copper during creep. *Metal Sci.J.*, 1:214, 1967.

[25] R.-J.Roe. Description of crystallite orientation in polycrystalline materials. III: General solution to pole figure inversion. *J. Appl. Phys.*, 36:2024, 1965.

[26] R.-J.Roe. Inversion of pole figures for materials having cubic crystal symmetry. *J. Appl. Phys.*, 37:2069, 1966.

[27] N.G.Needham and G.W.Greenwood. The creep of copper under superimposed hydrostatic pressure. *Metal Science*, 9:258, 1975.

[28] N.G.Needham, J.E.Wheatley, and G.W.Greenwood. The creep fracture of copper and magnesium. *Acta Metall.*, 23:23, 1975.

[29] M.F.Ashby, C.Gandhi, and D.M.R.Taplin. Overview no.3: Fracture-mechanism maps and their construction for f.c.c. metals and alloys. *Acta Metall.*, 27:699, 1979.

[30] R.T.Ratclife. The measurement of small density changes in solids. *Brit. J. Appl. Phys.*, 16:1193, 1965.

[31] J.Wadsworth, S.R.Keown, and J.H.Woodhead. The effect of niobium carbide precipitation on the density changes and creep properties of type 347 austenitic stainless steels. *Metal Sci.*, 10:105, 1976.

[32] H.Tanaka, M.Murata, M.Kaise, and N.Shinya. Creep-induced grain boundary damage and creep properties of SUS304. *ISIJ*, 74:2009, 1988.

[33] H.M.Ledbetter, R.J.Fields, and S.K.Datta. Creep cavities in copper: an ultrasonic velocity and composite-modeling study. *Acta Metall.*, 35:2393, 1987.

[34] C.S.Barrett. *Structure of Metals*. McGraw-Hill, New York, 2nd edition, 1952.

[35] H.-J.Bunge. *Texture Analysis in Materials Science*. Butterworks, London, 1982.

[36] C.M.Sayers. Ultrasonic velocities in anisotropic polycrystalline aggregates. *J. Phys. D*, 15:2157, 1982.

[37] A.J.Allen, M.T.Hutchings, C.M.Sayers, D.R.Allen, and R.L.Smith. Use of neutron diffraction texture measurements to establish a model for calculation of ultrasonic velocities in highly oriented austenitic weld metal. *J. Appl. Phys.*, 54:555, 1983.

[38] M.Hirao, K.Aoki, and H.Fukuoka. Texture of polycrystalline metals characterized by ultrasonic velocity measurements. *J. Acoust. Soc. Am.*, 81:1434, 1987.

[39] A.V.Clark,Jr., R.C.Reno, R.B.Thompson, J.F.Smith, G.V.Blessing, R.J.Fields, P.P.Delsanto, and R.B.Mignogna. Texture monitoring in aluminum alloys: A comparison of ultrasonic and neutron diffraction measurement. *Ultrasonics*, 26:189, 1988.

[40] A.V.Clark,Jr., R.B.Thompson, Y.Li.R.C.Reno, G.V.Blessing, D.V.Mitrakovic, R.E.Schramm, and D.Matlock. Ultrasonic measurement of sheet steel texture and formability: Comparison with neutron diffraction and mechanical measurements. *Res. Nondestr. Eval.*, 2:239, 1990.

[41] R.Hill. The elastic behavior of a crystalline aggregate. *Proc. R. Soc. London*, A65:349, 1952.

[42] R.F.S.Hearmon. *Landolt-Börnstein, Numerical Data and Functional Relationships in Science and Technology, Group III.* (eds K.-H.Hellwege and A.M.Hellwege), Springer, Berlin, 1966.

[43] C.M.Sayers and R.L.Smith. The propagation of ultrasound in porous media. *Ultrasonics*, 20:201, 1982.

[44] H.M.Ledbetter and S.K.Datta. Effective wave speeds in an SiC-particle-reinforced Al composite. *J. Acoust. Soc. Am.*, 79:239, 1986.

[45] C.M.Sayers. Inversion of ultrasonic wave velocity measurements to obtain the microcrack orientation distribution function in rocks. *Engng. Frac. Mech.*, 35:743, 1990.

[46] C.M.Sayers. Elastic anisotropy of short-fibre reinforced composites. *Int. J. Solids Structures*, 29:2933, 1992.

[47] M.L.Dunn and H.M.Ledbetter. Estimation of the orientation distribution of short-fiber composites using ultrasonic velocities. *J. Acoust. Soc. Am.*, 99:283, 1996.

[48] M.J.D.Powell. An efficient method for finding the minimum of a function of several variables without calculating derivatives. *Computer Journal*, 7:155, 1964.

[49] H.M.Ledbetter, S.K.Datta, and R.D.Kriz. Elastic constants of an anisotropic, nonhomogeneous particle-reinforced composite. *Acta Metall.*, 32:2225, 1984.

[50] T.Morishita and M.Hirao. Creep damage modeling based on ultrasonic velocities in copper. *Int. J. Solids Structures*, 34:1169, 1997.

[51] M.Ohnami, T.Endo, K.Yoshikawa, M.Kitagawa, and A.Nitta. Remaining life assessment of fossil fuel power plants: Current situation and activities. *J.JSME*, 90:556, 1987.

[52] H.Willems, W.Bendick, and H.Weber. Nondestructive evaluation of creep damage in service exposed 14 MoV 63 steel. In J.F.Bussière, J.-P.Monchalin, C.O.Ruud, and R.E.Green,Jr., editors, *Nondestructive Characterization of Materials II*, pages 451–459. Plenum Press, New York, 1987.

[53] A.S.Birring, D.G.Alcazer, J.J.Hanley, and S.Gehl. Detection of creep damage by ultrasonics. In D.O.Thompson and D.E.Chimenti, editors, *Review of Progress in Quantitative Nondestructive Evaluation, 8B*, pages 1833–1840. Plenum Press, New York, 1989.

[54] S.Kishimoto, N.Shinya, S.Matsumoto, and H.Fukuhara. Evaluation of creep cavity by measurement of ultrasonic velocity. *J. Soc. Materials Science Jpn.*, 39:1043, 1990.

[55] M.Hirao, T.Morishita, and H.Fukuoka. Ultrasonic velocity change with creep damage in copper. *Metall. Trans.*, 21A:1725, 1990.

[56] H.Willems. Investigation on creep damage in alloy 800H using ultrasonic velocity measurements. In J.F.Bussière, J.-P.Monchalin, C.O.Ruud, and R.E.Green,Jr., editors, *Nondestructive Characterization of Materials II*, pages 471–479. Plenum Press, New York, 1987.

[57] M.Nakashiro, H.Yoneyama, S.Shibata, and A.Ohtomo. Assessment for creep damage of boiler tube by newly researched ultrasonic technique. In *Proc. Int. Conf. on Advances in Material Technology for Fossil Power Plants*, page 351, 1987.

[58] M.Matsubara, A.Nitta, S.Sakai, and N.Fujinawa. A theoretical study on creep damage detection by ultrasonic wave measurement. *J. Soc. Materials Science Jpn.*, 39:1049, 1990.

[59] M.Matsubara and A.Nitta. Creep damage detection for a steam turbine rotor material after long-term service using ultrasonic technique. *Trans.JSME*, A59:2061, 1993.

[60] F.J.Margetan, R.B.Thompson, and I.Yalda-Mooshabad. Backscattered microstructural noise in ultrasonic toneburst measurements. *J. Nondestr. Eval.*, 13:111, 1994.

[61] M.Hirao, H.Fukuoka, and H.Koga. Ultrasonic backscattering noise and texture in pure titanium. In *Rev. Prog. in Quant. NDE*, pages 1699–1704. Plenum Press, New York, 1994.

[62] C.Ihara, T.Yanagi, and T.Tanaka. Estimation of creep life for metals based on damage mechanics. *Engng. Frac. Mech.*, 39:887, 1991.

[63] L.M.Kachanov. Time of the rupture process under creep conditions. *Izv. Akad. Nauk, SSR, Otd Tekh. Naul*, 8:26, 1958.

[64] Y.N.Rabotnov. *Creep Problems in Structural Members*. North-Holland, Amsterdam, 1969.

[65] D.R.Hayhurst, P.R.Brown, and C.J.Morrison. The role of continuum damage in creep crack growth. *Phil. Trans. R. Soc. Lond.*, A311:131, 1984.